MICROMACHINED BROADBAND ACOUSTIC TRANSDUCERS WITH INTEGRATED OPTICAL DISPLACEMENT DETECTION

A Dissertation Presented to

The Academic Faculty

By

Neal A. Hall

In Partial Fulfillment of the Requirements for the Degree Doctor of Philosophy in

Mechanical Engineering

Georgia Institute of Technology

October 20, 2004

MICROMACHINED BROADBAND ACOUSTIC TRANSDUCERS WITH INTEGRATED OPTICAL DISPLACEMENT DETECTION

Approved by:

Dr. F. Levent Degertekin, Chair

Dr. Yves Berthelot

Dr. Peter Rogers

Dr. Ken Cunefare

Dr. Zhiping Zhou

Dr. Mark Allen

October 20, 2004

ACKNOWLEDGEMENTS

This thesis is dedicated to all who made it possible. I would first like to thank the PhD reading committee - Professors Cunefare, Berthelot, Rogers, Allen, and Zhou for serving on my thesis and for their constructive feedback. I owe special thanks to my thesis advisor - Professor Degertekin – for being a good friend in addition to an excellent mentor. I can say the same thing he said regarding his former advisor: I have always felt privileged to be one of his students.

I would also like to thank all the members of the MiST Laboratory for their help and support. I owe special thanks to Guclu Onaran for helping out with theoretical issues, Wook Lee for serving as my teacher in the laboratory on many occasions, and Jeff McLean for his craftsmanship in constantly improving the conditions of the lab. I have equally enjoyed working closely with Kamran Jeelani and Baris Bicen over the past year, during which time a large portion of this work came together. I would also like to thank the students in Professor Cunefare's lab for generously donating their time while acquainting me with the first rate acoustic testing facilities at Georiga Tech.

Also, special thanks to Professor Zhou, Gary Spinner, and the entire MiRC cleanroom staff for helping out with many fabrication issues related to this work and for continuously improving the conditions in the cleanroom. I am fortunate to have been a part of their cleanroom during my time here. Thanks are also owed to the Defense Advanced Research Projects Agency (DARPA) and the National Institute of Health (NIH) for their financial support of this research.

Last and most importantly, I would like to thank my wife Lennie, my mother and father, and my two sisters for their tremendous support in all aspects of life.

TABLE OF CONTENTS

LIST OF TABLES

LIST OF FIGURES

SUMMARY

This thesis presents micromachined microphones with diffraction-based optical displacement detection. A compliant membrane is made part of a phase sensitive diffraction grating, and the deflection resulting from external acoustic pressure alters the intensities of the diffracted orders which are monitored with photodiodes. A 1-D analysis based on scalar diffraction theory is presented which provides expressions for the intensity of the diffracted orders. The analysis shows that the method provides the displacement sensitivity of a Michelson type interferometer and allows optoelectronic integration in a $1mm^3$ volume without beam splitters or critical alignment problems.

The method is implemented and characterized using microphone membranes with integrated diffraction grating back electrodes fabricated on silicon using Sandia National Laboratories' dedicated SwIFT-lite processing platform. These devices were fabricated with an isolated electrostatic actuation port which provides displacement sensitivity tuning and dynamic characterization capabilities. Detailed response characterization in both air and vacuum environments is performed to extract the diaphragm properties and high frequency cutoff frequencies of the microphone. Finite element models used to study the vibration modes of the diaphragm and the electrostatic actuation behavior are in good agreement with the measured data.

Internal noise measurements of the microphones are performed in the anechoic testing facility at Georgia Tech. A displacement resolution of 6×10^{-4}Å/√Hz is measured at 1kHz which is limited by thermal acoustic noise caused by the microphone's back-plate flow resistance. The back-plate resistance causes an upper cut-off frequency of 2kHz which adversely affects the performance of the device in the audio range and

results in a total noise level of 39.9dBA. The dominant noise sources across the entire frequency range are characterized and recommendations are made for future designs which can lead to microphones with noise levels below 20dBA.

The detection method is also applied to capacitive micromachined ultrasonic transducers (cMUTs) fabricated with diffraction grating bottom electrodes on quartz substrates. The large displacement sensitivity obtained from each individual 160μm element of the cMUT has enabled the demonstration of a phased imaging array in air only 4mm×4mm in size.

CHAPTER 1

BACKGROUND AND INTRODUCTION

Micromachined acoustic transducers are one of many MEMS technologies to have already demonstrated commercial and market relevance. Micromachined capacitive microphones, or "silicon microphones," made their debut in cellular phones this year, and hearing aid applications are close on the horizon [1]. In addition, capacitive micromachined ultrasonic transducers (cMUTs) have been shown to be a viable alternative to piezoelectric devices for non-destructive testing and medical ultrasound imaging applications [2-4]. Since their fabrication is based on integrated circuit manufacturing technology, cMUTs are especially suited for small scale transducer arrays and applications where electronics integration is advantageous [5, 6]. The physical structure and sound detection principle for both silicon microphones and cMUTs are similar. An electrically conductive and mechanically compliant top electrode is suspended over a rigid back electrode to form a capacitor. Incoming sound vibrates the top electrode and the resulting change in capacitance is detected, either under constant charge or constant voltage conditions. As discussed in the following sections, capacitive detection has fundamental limitations that bound the performance and, in turn, the range of applications for both of these micromachined acoustic sensors.

Silicon Microphones

Figure 1 shows a simple schematic of a silicon microphone. In order to detect frequencies in the audio range, these capacitive microphones must operate under a

constant charge condition. In this case, the membrane displacement results in a corresponding change in electric potential across the electrodes. The electrical sensitivity of the device, S_e, is defined as the change in voltage output per change in membrane displacement. In a similar fashion, the mechanical sensitivity, S_m, is defined as the change in membrane displacement per change in applied pressure (i.e. S_m is simply the compliance or softness of the membrane). The total sensitivity of the device to sound pressure can then be expressed as S_e X S_m, with units of V/Pa. For high S_e, a large DC bias voltage should be applied and the gap height between the electrodes should be made as small as possible, typically on the order of 2μm. In fact, these two requirements are in conflict, as the maximum DC bias that can be used is limited by the electrostatic collapse voltage, which decreases with shrinking gap height [7]. The electrical sensitivity is a maximum when the device is biased near this electrostatic collapse voltage. Unfortunately, the detection scheme becomes nonlinear under this same condition. In addition to this drawback, implementation of the constant charge condition requires the use of high impedance amplifiers, which often come with high electronic noise [6, 8].

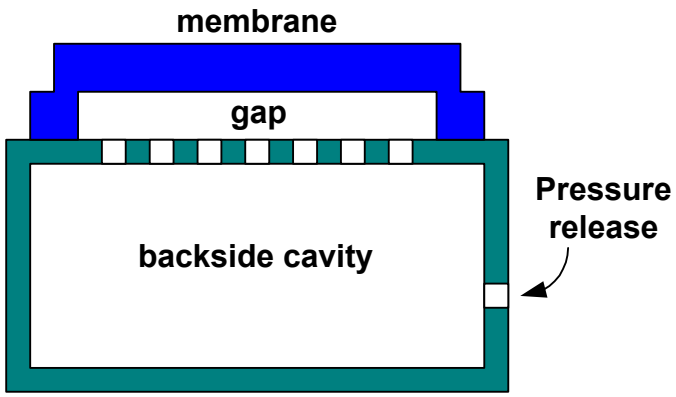

Figure 1 Schematic of a silicon microphone

To compensate for poor S_e, micromachined capacitive microphones must use large, soft membranes on the order of 1-5 mm to enhance mechanical sensitivity and, in turn, the overall device performance. Even this approach is limited, however, by membrane stresses that result during fabrication. These stresses bound the mechanical sensitivity that can be achieved and make the fabrication of uniform membranes with high yield difficult [1, 8]. In addition to using a soft membrane, the back electrode must be perforated and open to a large back-side cavity as shown in Figure 1 to prevent additional stiffening which would otherwise occur from compression of the air in the thin gap. The perforation reduces the active capacitance and adversely affects S_e, leading to yet another design conflict [7].

Capacitive Micromachined Ultrasonic Transducers

cMUTs operate in a manner different from silicon microphones, and capacitive detection presents some additional limitations. As shown in Figure 2, cMUTs use a movable membrane with a conductive film that is set into motion using electrostatic forces in the transmit mode. In this case, the membrane is much smaller and stiffer than a microphone membrane, and the gap between the membrane and the electrode can be either sealed under vacuum during fabrication, or left open to atmosphere to provide additional stiffness. A single cMUT employs hundreds of such membranes, each on the order of 50μm in diameter, to form an array on the order of $1cm^2$ that can effectively radiate and receive ultrasound.

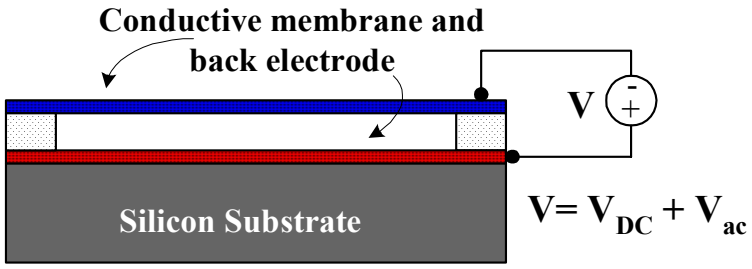

Figure 2 Schematic of a membrane element in a cMUT

In the receive mode, the most common approach is to measure the current caused by capacitance change under a constant DC bias voltage. The output current, i, of the cMUT in response to a membrane displacement, Δx, is given by the relation

$$i = \omega_a V_{bias} C \frac{\Delta x}{d_0} \tag{1}$$

where ω_a is the angular frequency of the acoustic wave, V_{bias} is the DC bias voltage, C is the cMUT capacitance and d_0 is the membrane-substrate gap. As seen in this equation, the output current is proportional to the frequency of the acoustic signal, resulting in poor sensitivity at low frequencies. This is essentially a result of measuring membrane velocity rather than displacement. The sensitivity can be improved by larger device capacitance, smaller gap and larger DC bias. As in the case of silicon microphones, the last two factors listed are in conflict. In addition, decreasing d_0 reduces the allowable membrane displacement in the transmit mode since this displacement can only be 1/3 of d_0 to prevent electrostatic collapse. This limits the maximum power of transmitted signals, especially for low frequency applications in air. To increase its active capacitance, the cMUT must receive sound as a whole with all of the individual membrane elements connected in parallel. This limits the phased array imaging capability of cMUTs, which demands high detection sensitivity from each individual

element. In addition to these drawbacks, the integration of complex low noise receive electronics with signal transmit circuitry is a difficult challenge and can be a limiting factor in some applications.

Alternative Detection Techniques

To improve the receive sensitivity of the cMUT at low frequencies, a method based on the interference of electromagnetic waves in artificial transmission line structures in the radio frequency (RF) range has been used to detect membrane displacement [9, 10]. As described in more detail in [9], the output current of a cMUT using this method can be expressed as

$$i = \omega_{RF} \frac{V_{RF}}{4} C \frac{\Delta x}{d_0} \tag{2}$$

where ω_{RF} is the angular frequency of the RF signal and V_{RF} is the RF signal amplitude. Since the RF signal frequency can be in the GHz range, this method effectively replaces the large DC bias with a large RF frequency bias. This method can provide high detection sensitivity in the audio range and has been implemented as a broadband microphone, as well. However, the method still requires a large capacitance and a small membrane-substrate gap. Furthermore, the electronics integration issue is still a problem. For microphone applications, the high RF power consumption can prevent remote applications where battery operation would be required, as in the case of portable communication devices and hearing aids.

It is clear that capacitive detection imposes profound limitations on the performance of micromachined acoustic transducers. Alternatively, in recognition of

this, more sensitive techniques to detect membrane displacement have been investigated. Optical interferometry has long been used to detect displacements with remarkable sensitivity in large scale apparatus and is a particularly attractive option to consider. These large scale systems have widely been used to characterize conventional piezoelectric and micromachined ultrasonic transducers [11, 12]. Unfortunately, most microscale implementations have not been successful due to integration difficulties [13, 14]. The optical schemes that have proven feasible to integrate use intensity modulation rather than phase modulation, and hence do not come close to achieving true interferometric sensitivity [13, 15]. An exception is a structure which utilizes interdigital phase-sensitive diffraction gratings. With this structure, interferometric displacement detection in atomic force microscopy and sensitive accelerometers have been made possible [16-19]. One important issue that has not been addressed in these implementations is the active optimization of detection sensitivity: Interferometric sensitivity is obtained only when the vertical distance between the reference and moving grating fingers is an odd multiple of $\lambda/8$, where λ is the optical wavelength in air.

In this thesis, an optical interferometric detection method for capacitive micromachined acoustic transducers is presented. The method uses a phase-sensitive diffraction grating embedded in a micromachined capacitive transducer, where the bottom electrode forms the reference fingers and the membrane serves as the moving reflector. It is shown that this scheme detects the displacement of the transducer membrane with interferometric sensitivity and can be easily integrated into a robust, microscale package. The electrostatic actuation port is still retained in this structure and provides several important functions: 1) it is used to actively control the detection

sensitivity by electrostatically biasing the membrane-grating gap, d, to the optimum value, 2) it enables transmission of acoustic waves by adding an AC signal to the DC bias for transmit-receive operation as in the case of cMUTs, but with the small gap constraint removed, and 3) it can also be used for self-calibration purposes in the case of microphone applications. For the case of cMUTs, transmit and receive electronics are isolated so no integration or switching electronics are required. For microphone applications, the enhancement in displacement sensitivity allows the requirement on S_m to be relaxed, so that smaller, stiffer membranes can be used to construct microphones with enhanced bandwidth, robustness, and fabrication yield. The scheme is also well suited to form miniature microphone arrays with high detection quality.

CHAPTER 2

DIFFRACTION BASED OPTICAL MICROPHONES

The fundamental operating principles of the method being introduced in this thesis are described in this chapter. An optical analysis using scalar diffraction theory provides analytical expressions that describe the diffracted field. The simple analysis provides expressions for the displacement detection sensitivity and for the position and size of the diffracted orders. These results confirm the suitability of the method for microscale integration. Consideration of the internal noise sources of the scheme lead to theoretical limits on the minimum detectable displacement. Finally, three enabling features of the method are discussed; 1) sensitivity-tuning, 2) self-calibration, and 3) differential order detection.

Phase Sensitive Diffraction Gratings

A simple schematic of the diffraction based optical displacement detection scheme under consideration is illustrated in Figure 3 to introduce the fundamental components and operating principles. This structure consists of a transparent substrate with an optically reflective diffraction grating fixed onto the surface. The grating of spatial period, d_g, consists of alternating regions of reflective fingers. An optical reflector, whose position is to be monitored, is placed behind the substrate. The overall system forms what is known as a phase sensitive diffraction grating [20, 21]. When illuminated through the substrate from the back-side with a coherent light source as

represented by the incoming plane wave fronts in Figure 3, light returns as a zero order specular reflected beam and as higher order diffracted beams.

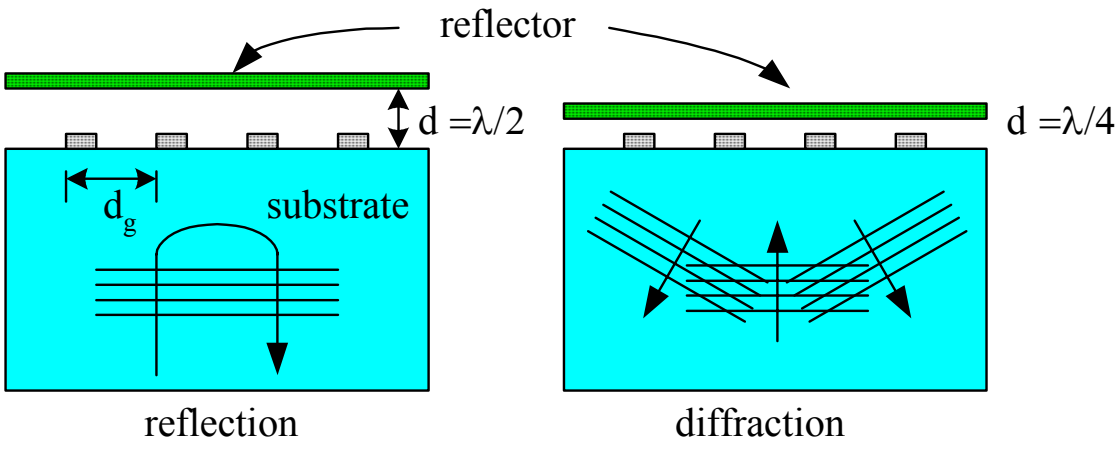

Figure 3 Schematic of the phase sensitive diffraction grating

The intensities of the reflected and diffracted orders are determined by the light that is directly reflected from the fixed diffraction fingers and also the light which passes through the fingers and travels to the reflector and back, thus accruing some additional phase which depends on the reflector distance, *d*. Both fields are superimposed and, as a result of interference, the intensity of each diffracted order depends on this reflector-substrate gap distance. Two intuitive cases are illustrated in Figure 3. When $d=\lambda/2$, where λ is the optical wavelength, the light traveling to the reflector and back undergoes a phase shift of 360^{o} and the system acts as a perfect mirror. In other words, there is pure reflection and no diffraction in this case. When $d=\lambda/4$, however, the light from the reflector has a relative phase of 180^{o} and all of the incident light power returns in the higher order diffracted beams. For all other values of *d*, both reflection and diffraction occur. The intensities of these orders can be monitored to obtain information about the reflector position.

Well known analytical techniques from scalar diffraction theory can be employed to formalize the analysis of the structure in Figure 3. A relatively simple analysis results if the wave fronts of both the incident light and the diffracted light are assumed to be plane. This is, of course, the far field or Fraunhofer approximation. In this case, the 1-D form of the Fresnel-Kirchhoff integral which relates the complex amplitude distribution *G* of an optical disturbance in the diffracted field to the amplitude distribution *g(y)* in the plane of an aperture reduces to

$$G(\upsilon) = \int_{-\infty}^{\infty} g(y) e^{-j\upsilon y} dy, \tag{3}$$

$$\upsilon = k\sin(\theta) = \frac{2\pi \sin(\theta)}{\lambda} = \frac{2\pi Y}{\lambda L} \tag{4}$$

where k is the wave number of the coherent light and θ, Y, and L are defined in Figure 4 which is a general schematic for the current analysis. Equation 3 is a superposition integral stating that the amplitude at a point in the far field is a phasor sum of the contributions from all wavelets of amplitude $g(y)dy$ occupying the aperture. The integral in Equation 3 is sometimes prefaced with a multitude of constants. Solving Equation 3 as it is written will provide the relative amplitude distribution in the diffracted field or, upon squaring – the relative intensity distribution which is the more important quantity as the intensity (not the amplitude) is ultimately measured. The simplistic form of the integral results from a series of geometrical assumptions that define the Fraunhofer approximation. As expressed in Equation 3, the distribution of the optical disturbance under these assumptions is the Fourier transform of the aperture function itself, where υ is referred to as the spatial frequency [22].

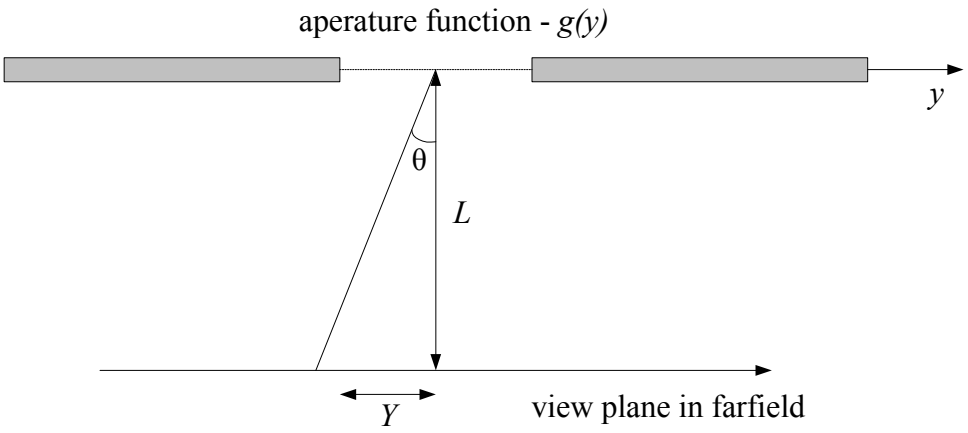

Figure 4 Schematic of the important parameters in computing the diffracted field

In this case, the aperture function that describes the phased grating is complex with uniform magnitude and a phase term that alternates in a square wave fashion. Without any loss of generality, such a function can be expressed as

$$g_{IG}(y) = e^{j\frac{\phi}{2}f(y)} = \cos(\frac{\phi}{2}) + jf(y)\sin(\frac{\phi}{2}) \tag{5}$$

where *f(y)* is the zero mean square wave function depicted in Figure 5 and ϕ is the relative phase difference between the light reflected from the grating fingers and the light reflected from the reflector. The latter travels an extra distance of 2*d*, and thus accrues an additional phase of

$$\phi = \frac{4\pi d}{\lambda} \tag{6}$$

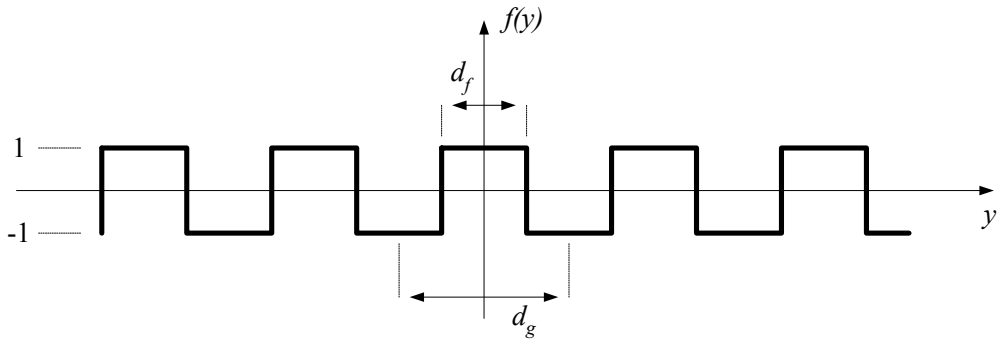

Figure 5 Zero mean square wave function describing the phase of the grating

The subscript *IG* on the aperture function in Equation 5 emphasizes that this particular function is unbounded and thus represents an infinite grating. The second form of g_{IG} makes use of Euler's identity as well as symmetry properties of the trigonometric functions. The Fourier transform of this function is

$$G_{IG}(\upsilon) = 2\pi \cos(\frac{\phi}{2})\delta(\upsilon) + j\sin(\frac{\phi}{2})\int_{-\infty}^{\infty} f(y)e^{-j\upsilon y}dy \tag{7}$$

where $\delta(\upsilon)$ is the impulse function. To evaluate the second term in Equation 7, we note that the Fourier transform of a periodic function consists of impulses with area equal to the Fourier series coefficients scaled by 2π and occurring at their respective harmonics of the fundamental spatial frequency

$$\upsilon_o = \frac{2\pi}{d_g} \tag{8}$$

A final form for the amplitude distribution in the diffraction field can then be expressed as

$$G_{IG}(\upsilon) = 2\pi \cos(\frac{\phi}{2})\delta(\upsilon) + j\sin(\frac{\phi}{2})\sum_{n=-\infty}^{\infty} 2\pi F_n \delta(\upsilon - n\upsilon_o) \tag{9}$$

where the Fourier series coefficients F_n for the periodic square wave are readily computed as

$$F_n = \frac{2\sin(n\pi \frac{d_f}{d_g})}{n\pi}, n \neq 0 \tag{10}$$

$$F_0 = 2\frac{d_f}{d_g} - 1 \tag{11}$$

From this analysis, we conclude that the diffraction orders occur at integer multiples of υ_o. The corresponding angles can be computed using the definition of the spatial frequency in Equation 4 which leads to the familiar diffraction grating equation

$$\sin(\theta_n) = \frac{n\lambda}{d_g}. \tag{12}$$

The relative amplitudes and intensities of these orders can be compared via Equation 9. In particular, it can be noted that when ϕ is equal to any integer multiple of 2π, the field consists of only the zero order which confirms the intuitive reasoning exemplified in Figure 3. If the grating is designed such that the fingers are half of the width of the period (i.e. $d_f/d_g = ½$), the zero order intensity is governed solely by the first term in Equation 9 and is zero when ϕ is any odd integer multiple of π. This is the second intuitive condition illustrated in Figure 3. For this grating geometry the intensities of the zero and first diffracted orders as a continuous function of the gap distance are

$$\begin{aligned} I_0 &= I_{in}\cos^2(\frac{\phi}{2}) = I_{in}\cos^2(\frac{2\pi d}{\lambda}), \\ I_{\pm 1} &= \frac{4I_{in}}{\pi^2}\sin^2(\frac{\phi}{2}) = \frac{4I_{in}}{\pi^2}\sin^2(\frac{2\pi d}{\lambda}) \end{aligned} \tag{13}$$

where the incident laser intensity, I_{in}, is used to scale the relative intensities provided by squaring the amplitudes given in Equation 9. I_{in} is the correct coefficient for the zero

order since, for d=0, all of the incident intensity is reflected back in this order. Another implication of this particular choice of grating geometry is the absence of the even diffracted orders as can be verified with Equation 10.

The intensities of the zero and first orders given in Equation 13 are plotted versus the gap distance in Figure 6. The third order is also shown to illustrate the diminishing intensity in the higher orders. One can use any of these diffraction orders to measure small displacements of the reflector with interferometric resolution. The highest displacement sensitivity and linearity for any diffraction order occurs when the second derivative of the expressions in Equation 13 with respect to gap thickness vanishes, which requires that d be an odd multiple of $\lambda/8$. Figure 6 also shows that the zero diffraction order is complementary to the first diffraction orders. Therefore, the output current, i, from a photodiode (PD) responding to a small displacement Δx of the reflector around this optimum gap thickness can be obtained by taking the derivative of the difference of these orders as

$$i = R\left|\frac{\partial\left(\mathrm{I}_0 - \alpha\mathrm{I}_1\right)}{\partial d}\Delta x\right| = R\mathrm{I}_{\mathrm{in}}\frac{4\pi}{\lambda}\Delta x \tag{14}$$

where R is the PD responsivity. The odd diffraction order outputs are scaled by a factor α to equalize the signal levels to the zero order. Alternatively, all orders other than the zero order can be collected and summed to form the complementary signal so that α=1 and no amplification is needed. It is clear that the method has the displacement sensitivity of a Michelson type optical interferometer. Deriving the output signal with this differencing scheme increases the signal level, uses the incident laser power efficiently, and reduces the laser intensity noise [23, 24]. This reduction in laser noise is discussed in more detail in the subsequent sections and is particularly critical when low-cost vertical cavity

surface emitting lasers (VCSELs) are used for microscale integration of acoustic sensors as discussed in the following section.

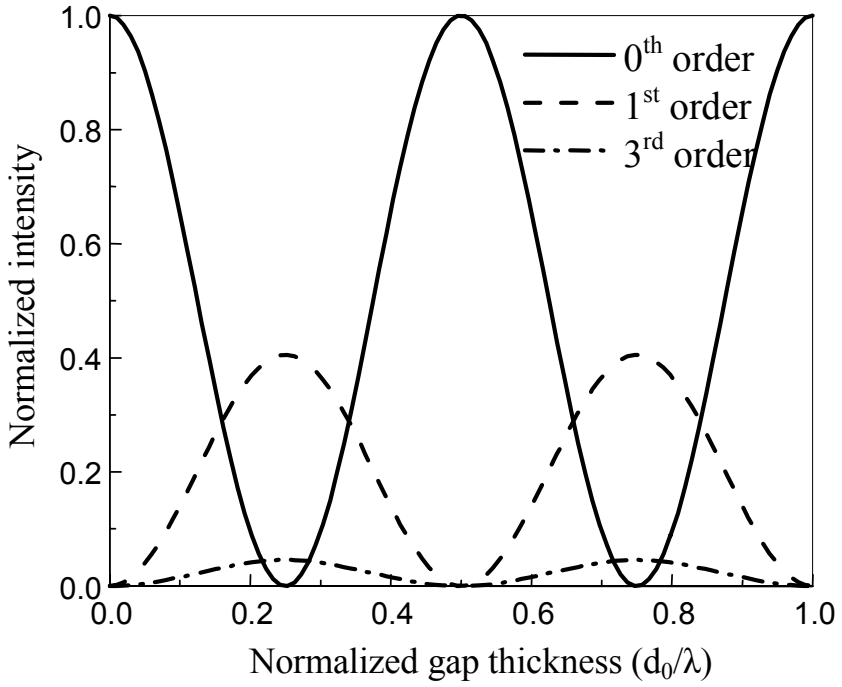

Figure 6 Zero, first, and third diffracted order intensities versus gap height

Microscale Integration of Acoustic Sensors

The most powerful feature of the detection scheme under analysis is the achievement of true interferometric displacement sensitivity in an optoelectronic system without beam splitters or critical optical alignment problems. As the analysis in this section shows, the method enables the integration of high fidelity micromachined acoustic sensors in volumes on the order of $\sim 1 mm^3$. Such sensors can be realized with a variety of physical embodiments such as the one shown in Figure 7. Here, the diffraction grating is fabricated on a transparent substrate such as a commercially available quartz or

sapphire wafer. The optical reflector is now a microfabricated compliant membrane that deflects due to sound pressure. The intensities of the diffracted orders are monitored with integrated photodiodes to obtain the sensor membrane displacement. These photodiodes can be fabricated on a separate substrate such as silicon or GaAs using standard, well developed complementary metal oxide semiconductor (CMOS) process runs. Depending on the particular design, a thin spacer on the order of ~1mm may or may not be needed to correctly align these PDs with the diffraction orders. A light source such as a focused beam from a HeNe or an optical fiber can be channeled to the system via an etched aperture in the PD substrate. Alternatively, for fully integrated sensors, a vertical cavity surface emitting laser (VCSEL) can be mounted directly on the surface of the PD as suggested in Figure 7. The voltage applied across the membrane and grating electrode adds sensitivity tuning and self calibration features which are discussed in subsequent sections. In the remainder of this section, the scalar diffraction analysis is extended to demonstrate how the sensor in Figure 7 can be integrated into microscale volumes.

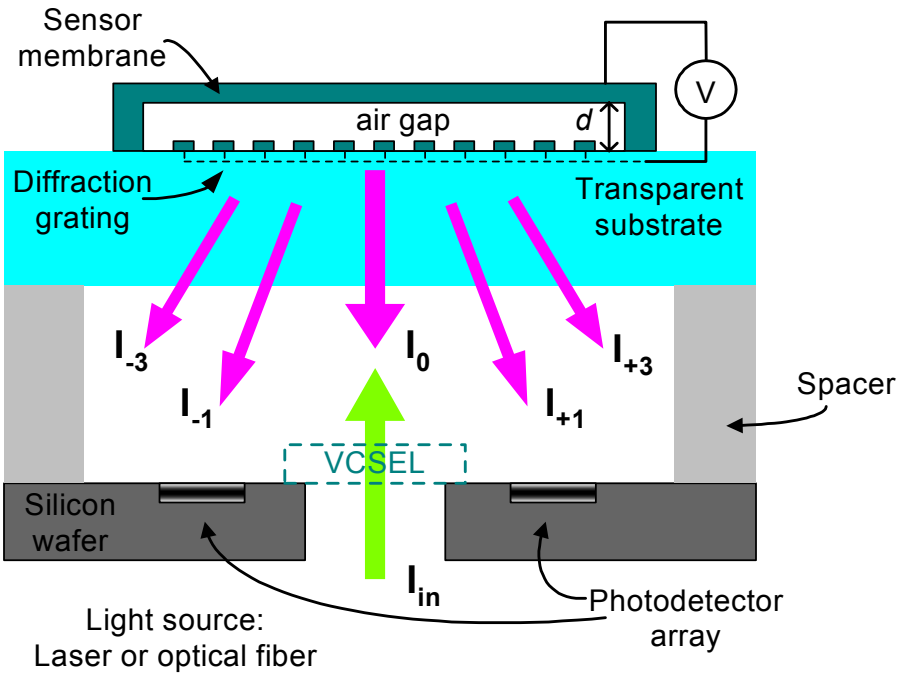

Figure 7 Schematic of a fully integrated diffraction based optical microphone

According to Equation 9, the diffraction orders occupy only an infinitesimal area in space which is not physically meaningful. This is a result of using the unbounded aperture function in Equation 5 which physically represents an illuminated region of infinite extent. The far field for such an aperture, as defined by the Fraunhofer approximation, is approached only as L approaches infinity. To model the actual intensity distribution in space of the diffracted orders, the infinite grating aperture function $g_{IG}(y)$ in Equation 3 can be multiplied by a windowing function, $w(y)$, to represent the fact that only a finite region of the grating is illuminated by the light source. Since the Fourier transform of the product of two functions is the convolution of each function's Fourier transform scaled by $1/2\pi$, the amplitude distribution of the diffracted field can be expressed as

$$G_{FG}(\upsilon) = \frac{1}{2\pi} G_{IG}(\upsilon) \otimes W(\upsilon) = \frac{1}{2\pi} \int_{-\infty}^{\infty} G_{IG}(\xi) W(\upsilon - \xi) d\xi.$$
$$= \cos(\frac{\phi}{2}) W(\upsilon) + j \sin(\frac{\phi}{2}) \sum_{n=-\infty}^{\infty} F_n W(\upsilon - n\upsilon_o) \tag{15}$$

where *W(υ)* is the Fourier transform of the windowing function and the subscript *FG* has been used to emphasize that this field is for a finite grating. Evaluation of the convolution integral shows that the spatial amplitude distribution of each order has the form of *W(υ)*. If the intensity of the incoming light source is uniform over the illuminated region, *w(y)* is a box function and *W(υ)* is the well known sinc function. This transform pair is expressed in Equation 16 where d_{IL} is the extent of the illuminated region and *h(y)* is the unit step function.

$$w(y) = [h(y + \frac{d_{IL}}{2}) - h(y - \frac{d_{IL}}{2})], \quad W(\upsilon) = \frac{2\sin(\frac{d_{IL}}{2}\upsilon)}{\upsilon} = d_{IL}\,\mathrm{sinc}(\frac{d_{IL}\upsilon}{2\pi}). \tag{16}$$

A particularly insightful expression for G_{FG} is obtained by combining Equations 15 and 16 and using the normalized spatial frequency variable $V=\upsilon/\upsilon o$ such that the orders occur at integer multiples of *V*. In this case, G_{FG} can be expressed as

$$G_{FG} = \cos(\frac{\phi}{2}) d_{IL}\,\mathrm{sinc}(\frac{d_{IL}}{d_g} V) + j \sin(\frac{\phi}{2}) \sum_{n=-\infty}^{\infty} F_n d_{IL}\,\mathrm{sinc}(\frac{d_{IL}}{d_g}(V - n)) \tag{17}$$

This form is insightful because it clearly shows that the shape of the diffraction field depends solely on the size of the illuminated region relative to the grating period. Shape in this context refers to the degree to which the orders overlap. For example, for d_{IL}/d_g=2, the field will be such that the first zeros of the sinc function governing the zero order will intersect the first zeros of the sinc function governing the first order. The wavelength of the incident light source relative to the grating period does not affect the

shape in this sense, but rather determines the angles at which the orders leave the grating as expressed in Equation 12. Together, Equations 12 and 17 can be used for the optoelectronic integration design.

A simple example is used to validate the feasibility of optoelectronics integration. A grating with 4μm period is assumed to be illuminated over 10 periods which corresponds to a 40μm spot size. The wavelength of the light source is taken as 850nm, which is the standard for commercially available VCSELs. The spacer in Figure 7 is taken as 1mm, which, together with a standard 0.5mm thick quartz substrate, makes the total propagation distance L equal to 1.5mm. Figure 8 shows the resulting intensity distribution for three different sensor membrane positions. The diffraction orders on this horizontal plane are well separated with a spacer thickness of only 1mm which enables integration in a small volume. Only a photodiode and a transimpedance amplifier are needed to convert optical signals to the electrical domain, resulting in very simple electronics.

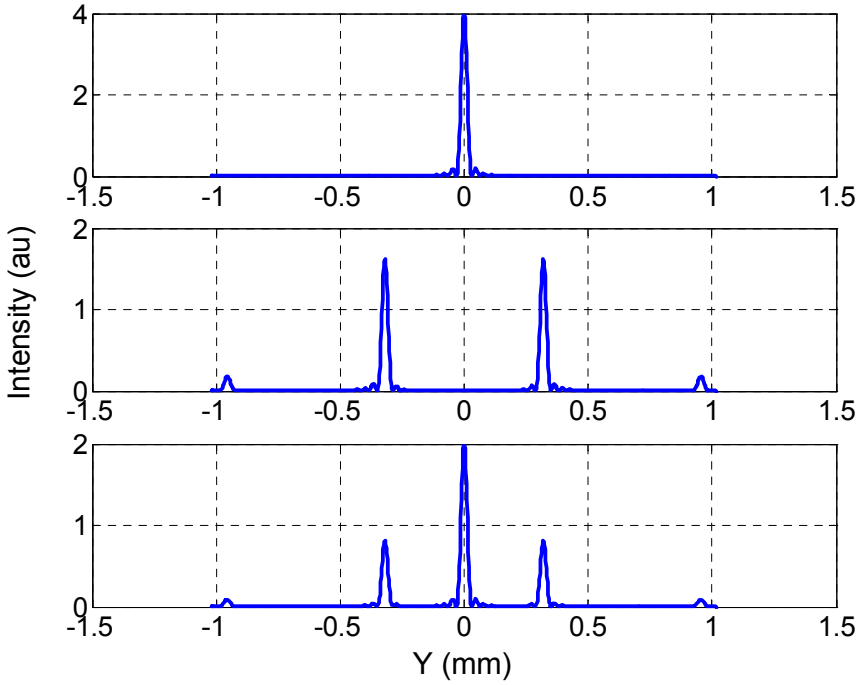

Figure 8 Plot of the diffracted field for gap heights of λ/2, λ/4, and λ/8.

The far field scalar analysis is useful for providing intuition and uncovering the essential physical trends of the method. However, with the tight integration dimensions given in the previous example, the analysis is closer to the near field rather than the far field regime. In addition, the Fraunhofer analysis cannot take into account complexities related to the divergence characteristics of the light source itself which can strongly influence the actual shape and size of the diffracted beams incident on the integrated PDs. The results of the previous analysis will accurately predict these beam sizes only if a well collimated light source is used. Therefore, these analysis results should be confirmed with a more sophisticated analysis using the 2D Fresnel diffraction integral. Furthermore, the effects of polarization can only be assessed using rigorous coupled wave theory based on Maxwell's equations. These analyses have been performed and the

details are described in the references [25, 26]. The important conclusions are summarized here: 1) for the wavelengths of most common light sources such as VCSELS and HeNe lasers, polarization effects are observed only for gratings with submicron periods, 2) the positions of the diffracted orders are fixed in space as suggested by the simple Fraunhofer analysis, and the expressions relating order intensity to gap thickness in Equation 13 maintain excellent accuracy, 3) the divergence characteristics of the light source strongly influence the diffraction beam characteristics, and the more detailed 2D Fresnel analysis should be used to improve results from the simple analysis before the optoelectronic design of microacoustic sensors.

To illustrate the third conclusion, the parameters used in the numerical example above to produce Figure 8 are used in a Fresnel analysis but with the VCSEL modeled as having a fundamental-mode Gaussian distribution with a 9μm waist [27]. The results of the 2D analysis are shown in Figure 9 where the X and Y axis together define the horizontal plane housing the integrated PD chip. These results show that one can build integrated photodiodes with CMOS electronics, where the photodiodes need to have 100μmx100μm active area and 275μm separation.

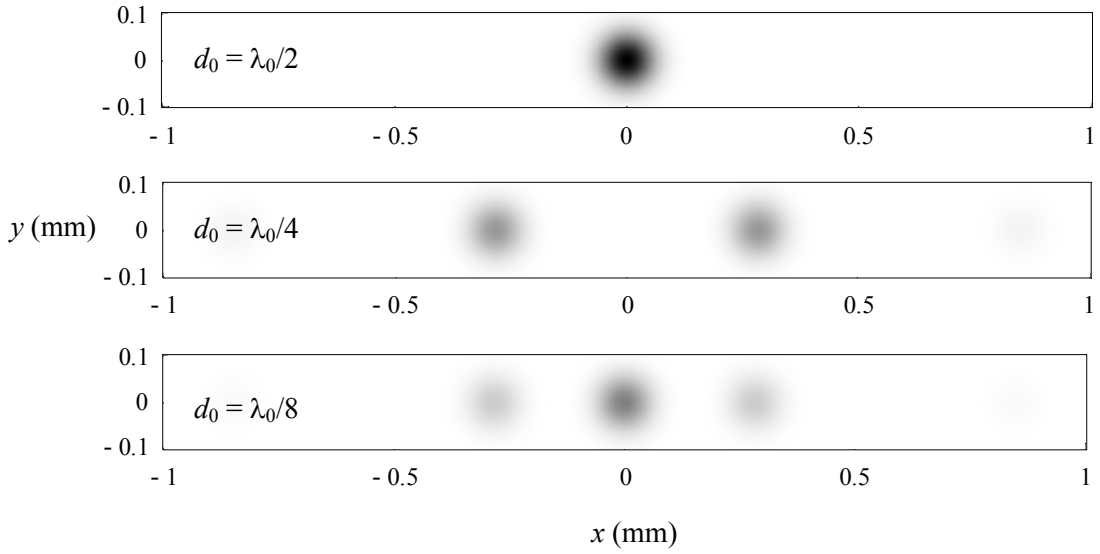

Figure 9 The diffracted field for three different gap heights as computed from a 2D Fresnel analysis

Differential Diffraction Order Detection

The displacement resolution or minimum detectable displacement (MDD) of the sensor (i.e. the noise-equivalent membrane displacement for SNR = 1) is determined as the ratio of the noise current generated at the PD amplifier output in A/√Hz to the detection sensitivity expressed in Equation 14, in A/Å. In general, the noise current consists of laser phase noise, detection electronics noise, laser intensity noise, and shot noise from the photodetectors. The total noise caused by the inherent phase noise of the laser is proportional to the path length over which the phase is modulated [28]. This distance can be on the order of meters for bench top interferometric systems, often making this a significant source of noise. In this case, however, the tight integration of the method minimizes this term as the phase is modulated over the gap height, *d,* which is on the order of 2μm. Furthermore, the only electronics required of the method are

transimpedance amplifiers to convert the photocurrent to an output voltage. Such amplifiers can be designed with noise levels well below photodetector shot noise. The two critical noise sources to consider are laser intensity noise and PD shot noise.

All lasers generate small fluctuations in output intensity. The amplitude of these fluctuations is proportional to the DC intensity, with the proportionality constant typically referred to as the relative intensity noise (RIN) of the laser. The RIN of high quality full-scale bench top lasers can be made quite low – often below photodetector shot noise. However, when inexpensive highly miniaturized light sources such as laser diodes or VCSELs are used as suggested in the integration schematic of Figure 7, RIN will be the dominant noise source of the displacement detection scheme. In this case, realizing high fidelity acoustic sensors with optical detection methods requires the implementation of a laser noise cancellation scheme whereby two complementary interference curves are generated and then subtracted to obtain the output signal. The diffraction based detection method under consideration automatically generates the complementary interference signals needed via the multiple diffraction orders. For example, the two PDs straddled across the VCSEL in Figure 7 can be designed to collect and sum all the higher order diffracted beams to form a signal with equal intensity and 180^{o} out of phase to the zero order. The following analysis quantifies the benefits of differential detection.

Equation 18 shows general expressions for the intensities of two complementary beams.

$$I = I_{in}\cos^2(\frac{\phi}{2}), \qquad I' = I_{in}\sin^2(\frac{\phi}{2}) \tag{18}$$

In both cases, changes in intensity are most sensitive to a small phase signal, $\phi_s(t)$, when ϕ is any odd multiple of $\pi/2$. The complementary photocurrents generated from linear

operation about one of these points can be obtained from a two term Taylor series expansion as

$$i = R\frac{I_{in}}{2}(1+\phi_s(t)), \qquad i' = R\frac{I_{in}}{2}(1-\phi_s(t)) \tag{19}$$

The complementary outputs in Equation 19 contain a DC photocurrent and the small signal photocurrent. Note that the first expression contains a positive signal term and the second expression contains a negative signal term. This would imply operation about a phase of $3\pi/2$ or any 2π increment of this value. Operation about a phase of $\pi/2$ on the other hand would result in a switching of the signs of the signal terms, but the important fact remains that the signals are always complementary. The intensity input from the light source can be expressed as the sum of a constant term, I_{DC}, and a zero mean RIN term $\alpha_n(t)I_{DC}$ as

$$I_{in} = I_{DC}(1+\alpha_n(t)). \tag{20}$$

To study the effect of the laser noise, Equation 20 is substituted into the Equations in 19. In addition, a PD shot noise term, $i_{shot}(t)$, has been added to each signal to create expressions for the PD output current that completely represent the presence of the signal and the two critical noise sources of the method.

$$i = R\frac{I_{DC}}{2}(1+\phi_s(t)) + R\frac{\alpha_n(t)I_{DC}}{2}(1+\phi_s(t)) + i_{shot}(t) \tag{21}$$

$$i' = R\frac{I_{DC}}{2}(1-\phi_s(t)) + R\frac{\alpha_n(t)I_{DC}}{2}(1-\phi_s(t)) + i'_{shot}(t). \tag{22}$$

The first term in each equation contains the DC photocurrent and the small signal current. From the second term, it is clear that the laser intensity noise is carried by the

DC photocurrent and a much smaller portion by the signal current itself. The shot noise from each PD is incoherent with respect to the other PD's shot noise, so separate labels have been retained for these two terms. Implementation of differential detection then yields

$$i - i' = RI_{DC}\phi_s(t) + R\alpha_n(t)I_{DC}\phi_s(t) + i_{shot}(t) - i'_{shot}(t) \tag{23}$$

Several important observations can be made about the resulting output current. The first term shows that differential detection results in doubling of the signal level. The sensitivity of the method can be obtained from this term by employing the relation between ϕ and the sensor membrane displacement given in Equation 6. The result is equivalent to that given in Equation 14. Second, we note that since the DC photocurrent has been subtracted out, the small signal current alone is left to carry the laser intensity noise. An intensity noise reduction factor, F, can be defined to quantify the gain as the ratio of the intensity noise with and without differential detection.

$$F = \left| \frac{\alpha_n(t)I_{DC}\phi_s(t)}{\frac{\alpha_n(t)I_{DC}}{2}(1+\phi_s(t))} \right| \approx \left|2\phi_s(t)\right| \tag{24}$$

For small linear signals, this reduction can be quite large. For example, for displacements on the order of 10^{-4} Å/√Hz, the corresponding amplitude of ϕ_s is $2\text{x}10^{-7}$ rads/√Hz. In light of this, it is clear that the detection scheme can be made shot noise limited even with the use of small, cheap surface lasers such as VCSELs. The shot noise terms in Equation 23 do not cancel because they are incoherent. Instead, their powers are additive which implies the amplitude of the shot noise increases by a factor of √2 with

differential detection. Shot noise has a flat distribution in frequency, with the amplitude spectral density in units of A/√Hz for a single PD computed as

$$i_{shot} = \sqrt{2qI_{DC}/R} \tag{25}$$

where q=1.6x10^{-19}C and I_{DC}/R is the DC photocurrent. As expressed in Equation 14, the detection sensitivity increases linearly with the incident laser power. Since the shot noise increases as $\sqrt{I_{in}}$, the displacement resolution has a $1/\sqrt{I_{in}}$ dependence. For example, for 1mW incident laser power and a photodetector with responsivity of 0.3, the MDD is ~ 1×10^{-5}Å/√Hz.

The previous development assumed access to perfect complementary beams from the optical detection system. However, due to optical losses, scattering, and polarization effects, the beams may not be perfectly out of phase nor will they have identical interference swings. When this is the case, operating the sensor about a gap height where the interference curves' slopes are equal and opposite in magnitude and their DC intensity outputs are identical will not be possible. This situation is depicted in Figure 10.

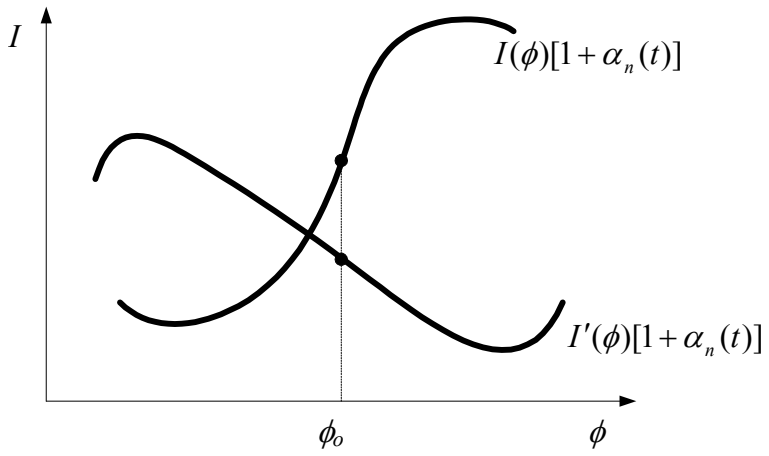

Figure 10 Schematic of imperfect interference curves

As before, $\alpha_n(t)$ is chosen to represent the intensity noise of the laser which effectively causes the curves in Figure 10 to oscillate randomly about a mean value of the interference function, $I(\phi)$, as expressed in the figure. With no noise, the intensity output resulting from small signal, $\phi_s(t)$, can be expressed as

$$I = I(\phi_o) + \frac{dI}{d\phi}\phi_s(t). \tag{26}$$

With the fluctuations in the curve caused by intensity noise accounted for, however, the complimentary output photocurrents from the PDs are written as

$$i = R[I(\phi_o) + \frac{dI}{d\phi}(\phi_o)\phi_s(t) + \alpha_n(t)I(\phi_o) + \alpha_n(t)\frac{dI}{d\phi}(\phi_o)\phi_s(t)] \tag{27}$$

$$i' = R[I'(\phi_o) + \frac{dI'}{d\phi}(\phi_o)\phi_s(t) + \alpha_n(t)I'(\phi_o) + \alpha_n(t)\frac{dI'}{d\phi}(\phi_o)\phi_s(t)] \tag{28}$$

Again, it is clear that the intensity noise in each signal is carried by both the DC intensity of the laser and the smaller signal term. When differential detection is implemented, the resulting signal is expressed as

$$i - i' = R(1+\alpha_n(t))[I(\phi_o) - I'(\phi_o)] + R(1+\alpha_n(t))[(\frac{dI}{d\phi} - \frac{dI'}{d\phi})\Big|_{\phi_o}\phi_s(t)] \tag{29}$$

In this case, it is more critical to choose a gap height such that the DC intensities from each interference curve are equalized rather than their slopes to ensure that the small signal current alone is left to carry the intensity noise. Even under these circumstances, the laser intensity should be made small enough so that the scheme is shot noise limited.

To illustrate the impact of the method's high displacement sensitivity for a microphone application, consider that 20dBA detection corresponds to a minimum detectable pressure of 2×10^{-4}Pa. For a 10kHz bandwidth, the minimum detectable

displacement of the method under consideration is 10^{-3} Å. Therefore, the required S_m of the membrane is only 5 Å /Pa, which can easily be achieved with standard micro fabrication materials using a membrane on the order of 300μm in diameter. Such a membrane would resonate near 200kHz. For comparison, a traditional silicon microphone would require a membrane approximately 100X softer to achieve a 20dBA noise level. Such a membrane would be ~5mm^2 and would resonate near 10kHz.

The value of the enhanced S_e can be used in several ways, depending on the design and application of interest. For example, an extremely low noise microphone can be realized if high S_m is retained by using a membrane structure similar to that of silicon microphones. Alternatively, some mechanical sensitivity can be traded for bandwidth by using slightly stiffer membranes to form high quality, miniaturized broadband microphones, as in the numerical example presented above. Lastly, for ultrasonic transducers a great deal of S_m can be traded for bandwidth by using cMUTs fabricated on transparent substrates.

Pulsed Laser Operation and Electrostatic Actuation

Two additional important features of the detection method presented in the chapter should be mentioned before closing. First, the high detection resolution of the method can be achieved with much lower power if the light source is pulsed with a low duty cycle. Semiconductor lasers such as VCSELS can be pulsed into the GHz range, so the average laser power can be reduced by a factor of 10^{-6} for audio bandwidth applications. Alternatively, the average power can be kept the same such that very high intensity pulses are used when the laser is pulsed. Recall that this improves the detection

resolution in proportion to $1/\sqrt{I_{in}}$. There are, of course, practical limitations with these approaches. Namely, the bandwidth of the PDs must be at least comparable to the signal delivered from the pulse. Also, there are limitations of laser intensity available from VCSELs. The key point, however, is that the method opens up a new design space for micromachined acoustic transducers without the limitations imposed by capacitive detection.

The second important feature of the method is the creation of an electrostatic actuation port that is electrically isolated from the optical displacement detection. Recall that the largest displacement sensitivity and linearity for any diffraction order occurs when the gap height is $\lambda/8$ or any odd multiple of this value. In practice, it can be difficult to fabricate this tolerance. Further, even if the gaps could be fabricated to this value, changes in ambient temperature, humidity, or barometric pressure can cause the membrane to deflect off of this value. Therefore, to ensure the operation of the sensor at one of these optimal points, the membrane can be electrostatically actuated by applying a bias voltage between the diffraction grating (fixed electrode) and the membrane (deformable electrode) as suggested in Figure 7. This electrostatic actuation port can also be used to apply dynamic signals to the membrane that can be used as self calibration signals. These features are demonstrated on prototype diffraction based optical microphones fabricated on silicon as described in the next chapter.

CHAPTER 3

DESIGN AND FABRICATION OF OPTICAL MICROPHONES

The goal of this thesis is to demonstrate successful operation of the diffraction based detection scheme by modeling, designing, fabricating, and experimentally characterizing diffraction based optical microphones with a hand-held set-up. Specifically, the demonstration of such a microphone with ~30dBA noise level is targeted. To accomplish this, microphone membranes with integrated diffraction grating bottom electrodes are micromachined with Sandia's dedicated fabrication technology. A small spacer fabricated using stereo lithography and a quartz window form the back-side cavity for the microfabricated chip and complete the front end package. In this chapter, the advantages of using Sandia National Laboratory's (SNL) fabrication process are discussed and the process flow for the fabrication of the microphones is presented. Micrographs of completed silicon chips and pictures of the completed package used for characterization are then presented.

Sandia's Dedicated Fabrication Platform

Generally speaking, there is a continuous spectrum of automation and dedication of MEMS fabrication processes. University level cleanrooms are typically at one extreme end of the spectrum as they are designed for prototype level work and one-off creations. A wide selection of materials are available including a variety of sputtered metals, sputtered dielectrics, thick (~100μm) photolithographic patterned structural polymers such as SU-8, and several types of chemical vapor deposited (CVD) materials

such as silicon nitride, silicon carbide, and polysilicon. Furthermore, the deposition tools can be varied over a wide range of operating parameters such as temperature, pressure, and power to make available a continuous spectrum of mechanical and electrical properties for a given material. The trade off for this flexibility is poor repeatability. Because the tools are used in multiple ways throughout the course of a day, the variance of the outcome for a given set a parameters will vary – typically resulting in poor yield of completed device runs.

At the other end of the spectrum are MEMS commercial foundries. In this case, flexibility is traded for high repeatability as each piece of equipment is dedicated to perform a specific task under constant operating conditions. Process runs with fixed material types and fixed material thickness and properties are offered. Furthermore, in an assembly line fashion, a particular platform lays out the order in which these materials are deposited onto the particular substrate being used. The device designer is left to choose only how each deposited layer will be etched via the creation of a mask set for photolithographic patterning before the next layer of material is deposited. SNL offers four dedicated processing technologies – the most well known being the Sandia Ultra-planar, Multi-level MEMS Technology (SUMMiT-V) which offers five structural layers of polysilicon interlaced with four layers of sacrificial oxide [29]. For device designs demanding less complexity, simpler processes are offered such as SwIFT-lite which consists of a structural nitride and polysilicon layer and a single sacrificial oxide layer.

In this investigation, we choose to develop the diffraction based optical microphones using SNL's SwIFT-lite process for several reasons. By demonstrating the fabrication compatibility with a dedicated process, the compatibility with almost any full

scale production foundry is also being demonstrated. In particular, compatibility with SNL's simplest platform lends further credence to the commercial viability of the approach since production costs scale with complexity. Choosing the most basic of processes with limited layers also emphasizes a major value proposition of the method - the creation of an interferometer without beam splitters or auxiliary optical components for alignment. Furthermore, the materials used in this process are the same as those for most production scale foundries as they have proven to be robust and reliable. For example, polysilicon and nitride are standard membrane materials that have undergone extensive reliability studies in MEMS device research.

Conceptual Layout of Microphone Structures

The layers available in the SwIFT-lite process are shown in Figure 11. The process begins by thermally growing 0.63μm of oxide on the surface of a silicon wafer. The next layer is 0.80μm thick low stress silicon-nitride deposited via low pressure chemical vapor deposition (LPCVD). In most applications, the combined purpose of these two layers is electrical isolation from the silicon substrate. A 0.3μm thick layer of phosphorus doped polysilicon is deposited via LPCVD to form a ground plane. Two structural layers of silicon nitride with 0.3μm and 0.8μm thickness, respectively, and 100MPa residual stress are separated by a 2.0μm thick sacrificial layer of oxide which is deposited using tetraethylorthosilicate (TEOS). The final layer is 2.5μm thick LPCVD structural polysilicon deposited above the upper nitride layer. The layer labels in Figure 11 are consistent with those used by SNL and their use is retained for discussion here.

Each of these layers are patterned via etch processes according to the designer's photolithographic mask layout before the subsequent layer is deposited.

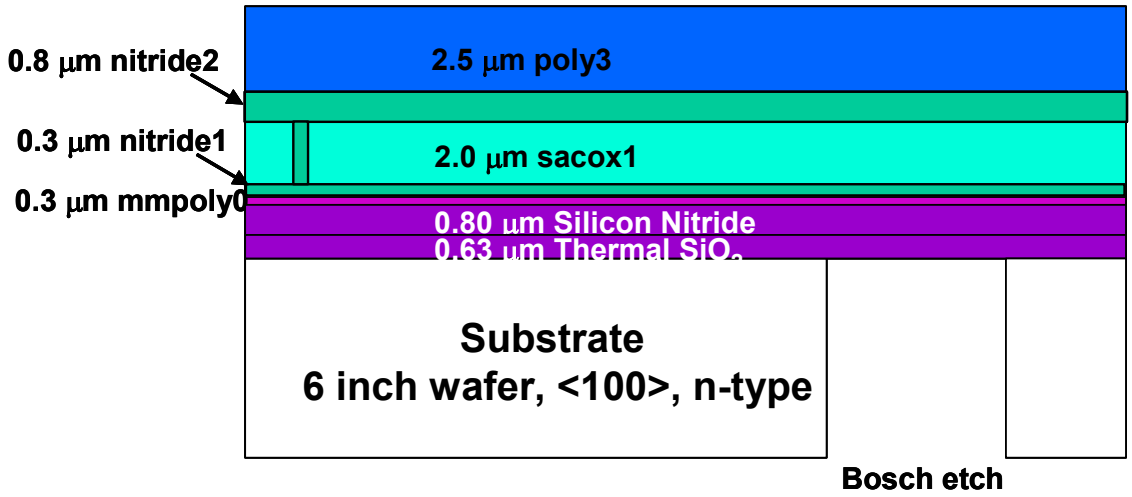

Figure 11 Layers available in SNL's SwIFT-lite fabrication platform

It is clear that the design process is strongly coupled with the fabrication process. With a soft prototype fabrication process, the natural order for prototype development is to model, optimize, design, and then fabricate. With a dedicated micromachining process such as SwIFT-lite, the fabrication constraints must be incorporated into the process from the start as only a discrete number of conceptual designs are compatible with the particular process being used. Since the thickness and tension of the structural layers are predetermined, the lateral dimensions alone can be tailored by the designer to get the stiffness and resonant properties desired from the structure.

The fabrication process flow chosen to fabricate the optical microphones is schematically shown in Figure 12. First, the nitride and oxide layers are etched to form an optical diffraction grating with a 5μm period. As shown in (a), larger holes are also etched in this layer which will enable the creation of a perforated back-plate. Next, the

thin mmpoly0 layer of polysilicon is deposited and patterned over the nitride grating as shown in (b). The first nitride layer (nitride 1) to follow is not needed for this particular design, so this entire layer is etched after its deposition and is therefore not shown in the fabrication sequence of Figure 12. The sacox1 layer is then deposited to form the sacrificial layer for creation of the nitride membrane. As emphasized by the schematic in (c), the deposition is conformal and takes the shape of the underlying topography. Although not drawn in (c), this effect also produces small corrugations over the diffraction grating region. In SNL's more complex processes such as SUMMiT, this topography in the sacrificial oxide is eliminated with a process known as chemical-mechanical polishing (CMP). In this case, however, the topography is not a major concern. As shown in (c), the sacrificial oxide is etched along a square perimeter to allow anchoring of the nitride membrane whose deposition follows in (d). Next, the poly3 layer of polysilicon is deposited and patterned on top of the nitride membrane to form the top electrode as shown in (e). This completes the surface micromachining stages of the fabrication process.

The next step is to etch a hole through the back-side of the silicon wafer with a deep reactive ion etch (DRIE) known as a Bosch process. This etch will efficiently attack both the substrate (single crystal silicon) and the polysilicon ground plane. In addition, the process has a high selectivity with respect to silicon dioxide and thus will be halted when it reaches the thermal oxide and sacox1 layers as shown in (f). A counter bore etch is first performed half way through the 400μm thick wafer to enhance the spatial resolution of the subsequent etch. Finally, the device is subjected to a dry hydrofluoric

(HF) chemistry which attacks any exposed silicon dioxide – including regions of both sacox1 and the thermal oxide. A schematic of the completed structure is shown in (g).

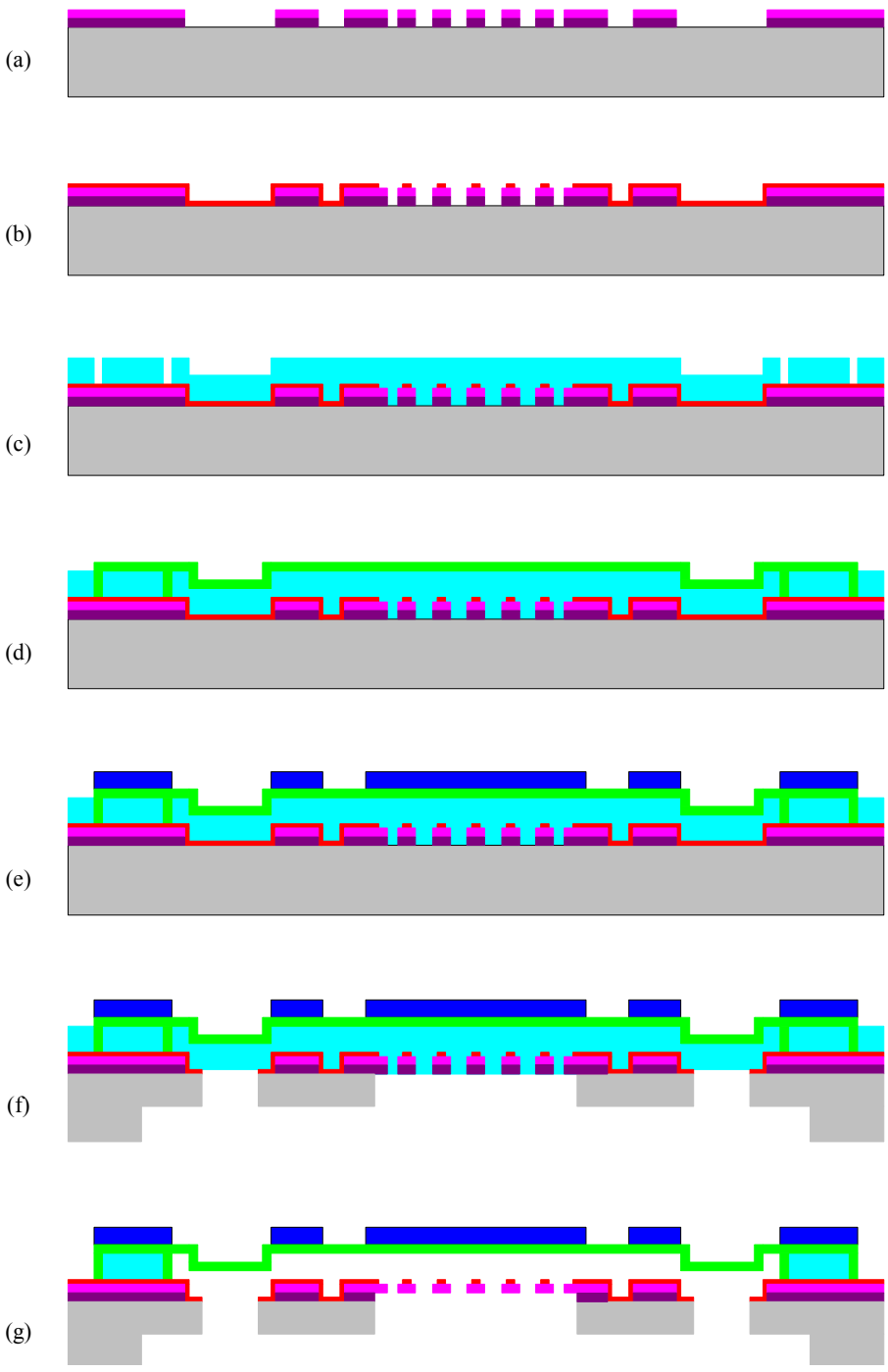

Figure 12 Fabrication process used to fabricate optical microphones with SNL's SwIFT-lite platform

Several details of the completed structure are worth noting. Since silicon nitride is neither optically reflective nor electrically conductive, the polysilicon top electrode (which is both) plays a critical role in enabling both the optical displacement detection and capacitive actuation of the membrane. As demonstrated in the following chapters, the latter enables tuning of the displacement sensitivity and broadband characterization of the structure in both air and vacuum environments. It is neither necessary nor desirable, however, to have polysilicon across the full extent of the nitride membrane. Doing so can increase the stiffness of the microphone and adversely affect the microphone sensitivity. In addition to the region directly above the grating, enough polysilicon should remain to allow the membrane to be actuated with reasonable voltages across the thin 2μm air gap. A coupled physics finite element model employed to study the electrostatic actuation of the membrane is presented in the next chapter.

This air gap is open to the much thicker back-side cavity formed by the bulk silicon wafer via the etched holes in the diffraction grating and the larger perforation holes etched through the 200μm thick back-plate. As shown in the completed schematic of Figure 12 (g), the top polysilicon electrode is not placed above these holes since capacitive actuation forces are minimal here due to the absence of the bottom back-plate. This perforation of the back-plate is a technique used in both MEMs microphones and traditional capacitive microphones to prevent severe stiffening of the structure which would otherwise occur from compression of the air trapped in the thin gap. For regular capacitive microphones, this technique presents a design conflict since the holes reduce the active capacitance of the structure and therefore degrade the electrical sensitivity. In addition to sensitivity, the back-plate design affects the bandwidth of the microphone as a

larger degree of perforation is needed to eliminate the gas stiffening at higher frequencies. These issues must be settled with compromise in capacitive microphone design. For the optical microphones under current consideration, the mechanics of the structure are decoupled with the displacement detection sensitivity so a large degree of perforation can be used to eliminate squeeze film effects up to ultrasonic frequencies. The only requirement is that enough of a bottom electrode remain to enable capacitive actuation of the membrane if this is a desired feature for the particular design. Dynamic models for the microphone response are also discussed in the following chapter.

Many details of the diffraction grating electrode are also worth noting. With the underlying thermal oxide etched away, the 5μm period diffraction grating is composed of the nitride layer and the thin polysilicon layer. Without the polysilicon, the fingers would be neither optically reflective nor electrically conductive. As shown in the zoomed in schematic of the grating in Figure 13, these layers are patterned such that each grating finger contains a 2μm wide layer of polysilicon centered on a 3μm wide nitride finger. The purpose of this design is to ensure a robust fabrication process. Otherwise the sides of each polysilicon finger would risk being exposed to the DRIE in step (f) which could result in a lateral etching away of this region if the etch were not properly timed. With the current design, the sacrificial silicon dioxide layer is ensured to cover and protect the polysilicon regions of the fingers during the DRIE.

A potential consequence of having the grating designed in this manner is polarization effects. The 0.5μm wide edges of nitride that straddle the 2μm wide polysilicon region are not completely transparent as the nitride does not have perfect transmittance. This makes the minimum feature size of the grating 0.5μm which is small

enough to make polarization issues relevant. To avoid these complications, a final fabrication step is the blank sputtering of a thin 100nm layer of gold on the back-side of the devices which is performed in the MiRC cleanroom at Georgia Tech.

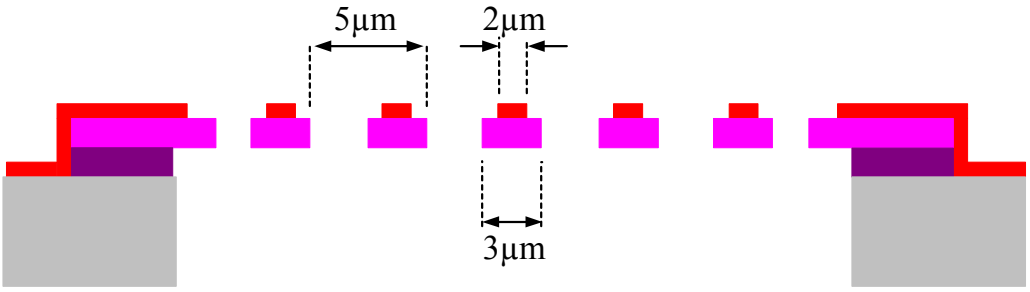

Figure 13 Detailed schematic of the diffraction grating fabrication

Figure 12 (g) and Figure 13 illustrate an additional issue related to the diffraction grating. The grating itself is not fabricated on the 200μm thick bulk silicon back-plate, but instead on the thin 0.8μm nitride which itself becomes an anchored membrane structure upon completion of the device. Ideally, this diffraction grating structure should be made as rigid as possible for two primary reasons. First, if the grating structure is compliant, it will deflect up towards the membrane during electrostatic actuation since this process exerts equal and opposite pressures on the top and bottom electrodes. This effect is not too critical since tuning of the displacement sensitivity depends on changing only the relative gap distance between the two. However, for optimal optical conditions, both reflectors should remain as flat as possible. For the microphone membrane, the relatively large size ensures a flat deflected region across the aperture area. The suspended diffraction grating membrane is made small relative to the microphone to increase its rigidity. An additional tactic that can be used is to simply electrically isolate the top polysilicon reflector from the active region of the top electrode. This way,

minimal electrostatic forces exist between the two. This technique, however, can only be used for the larger, softer microphone membranes. For smaller, stiffer membranes, the area above the grating must be employed as an active electrode to enable reasonable actuation voltages.

The second issue is related to the dynamic operation of the microphone. When the top membrane deflects due to acoustic pressure on the front-side, a pressure is generated on the back-side in the thin 2μm air gap. This pressure can also displace the diffraction grating in unison with the top membrane. When this occurs, the relative change in displacement of the gap distance caused by the acoustic pressure is reduced which results in a reduction in microphone sensitivity. The dynamic modeling presented in the next chapter shows that the completed designs successfully mitigate these concerns.

The finalized designs consist of a complete set of mask drawings in AutoCAD with each drawing layer converted into a physical mask used for photolithographic patterning during the actual fabrication. SwIFT-lite is a 10 step process requiring 10 such masks. The chip area available for the optical microphone production is 6340μm×2820μm, providing space to test 6 unique designs varying in membrane size and back-plate design. Figure 14 shows the AutoCAD mask drawings submitted for production.

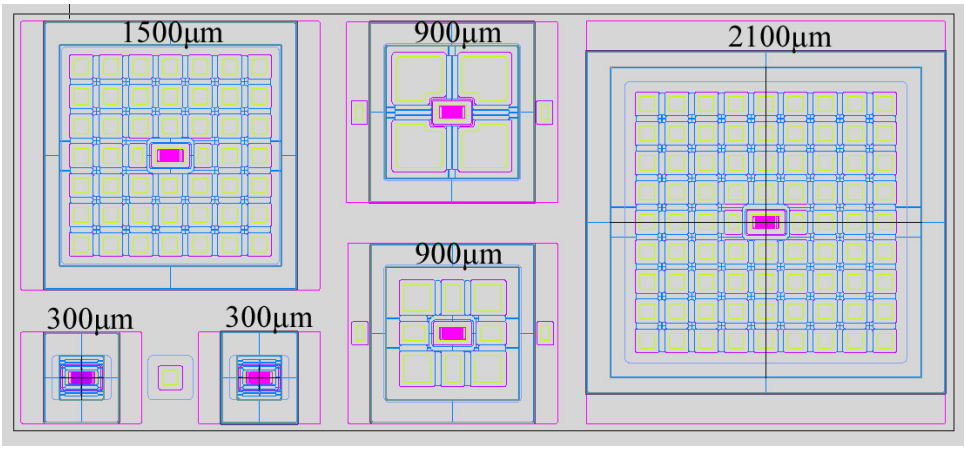

Figure 14 AutoCAD mask layout drawings used for fabricating optical microphones with SNL's SwIFT-lite process

The details of the device architecture are made clear in micrographs of the completed devices. Back and front-side micrographs of a 900µm device are shown in Figure 15 and Figure 17. The first plane observed in the back-side view is the surface of the 400µm thick bulk silicon wafer itself. At a distance of 200µm deeper into the page lies the back surface of the back-plate with 9 perforation holes etched all the way through. Looking 200µm deeper into the page through the center hole makes visible the diffraction grating structure etched into the lower nitride membrane. For the remaining 8 holes along the periphery, this plane makes visible the back-side of the nitride microphone membrane resting above the thin 2µm air gap. It is difficult to focus on all three planes simultaneously which is why Figure 15 appears somewhat fuzzy. A micrograph of the diffraction grating is obtained in a separate capture shown in Figure 16.

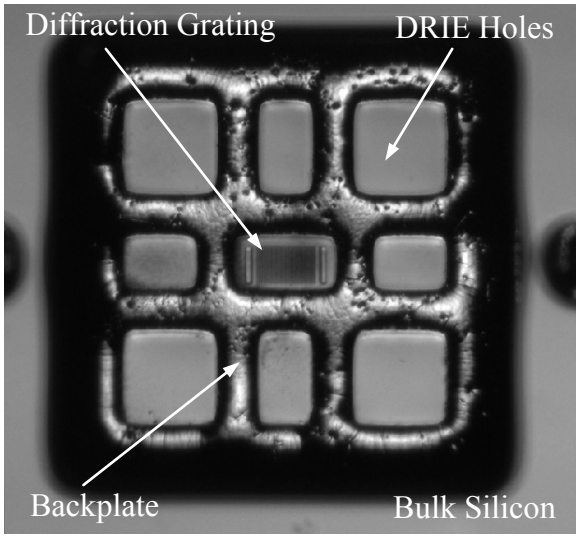

Figure 15 Back-side micrograph of a 900μm optical microphone

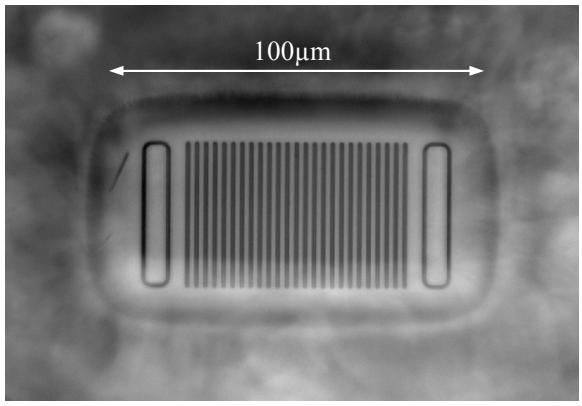

Figure 16 Zoomed micrograph of the diffraction grating structure in Figure 15

Figure 17 shows the top-side of the same device. Here the front surface of the bulk silicon substrate can be seen which has the electrically isolating silicon dioxide and nitride layers patterned across the entire surface. Enough of the poly0 ground plane is kept along the circumference of the device to provide a wire bond pad for this bottom electrode. As drawn schematically in Figure 12 (g), the top electrode is patterned above the membrane anchor which provides a robust wire bond pad for the top electrode. Thin

connectors stem from the bond pad to connect the remaining portions of the top electrode attached to the transparent silicon nitride membrane. Finally, the top reflector is observable in the center of the nitride membrane. In this case, the reflector is not made part of the top electrode as no connections can be observed in the figure. It should be noted that the top reflector, itself, has the appearance of a grated structure. This is due to the topographical processing issues discussed above related to Figure 12.

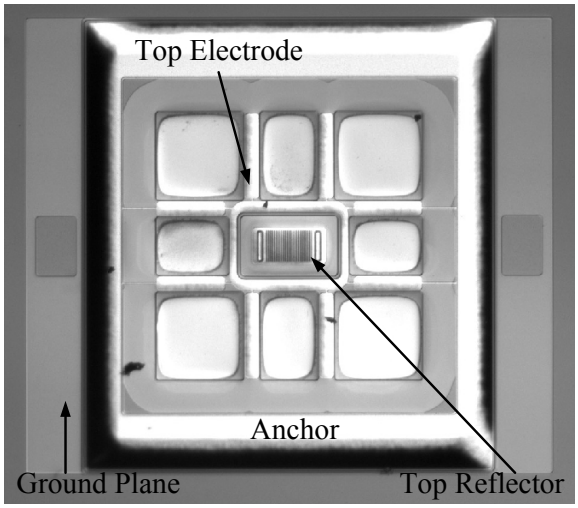

Figure 17 Top-side micrograph of the 900μm optical microphone shown in Figure 15

The five other devices have an almost identical architecture, but different overall membrane size and back-plate design. A particularly interesting design is shown in Figure 18. In this case, there are 4 very large holes etched along the outer periphery of the device. This type of structure has the ability to eliminate squeeze film damping effects into the ultrasonic frequency range. For good capacitive detection, a design like this would not be feasible. The particular membrane of primary importance for this thesis, however, is shown in Figure 19. This 2100μm device is the largest of the submitted designs and therefore exhibits the largest mechanical sensitivity. The

experimental acoustic characterization and microphone performance assessment presented in this thesis are for this structure.

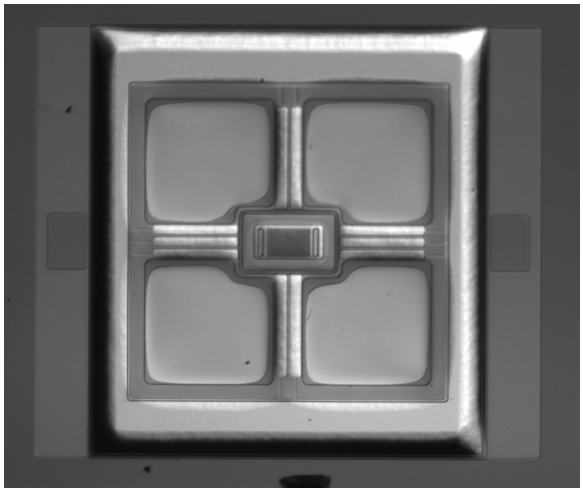

Figure 18 An additional architecture of a 900μm microphone membrane with 4 large DRIE holes

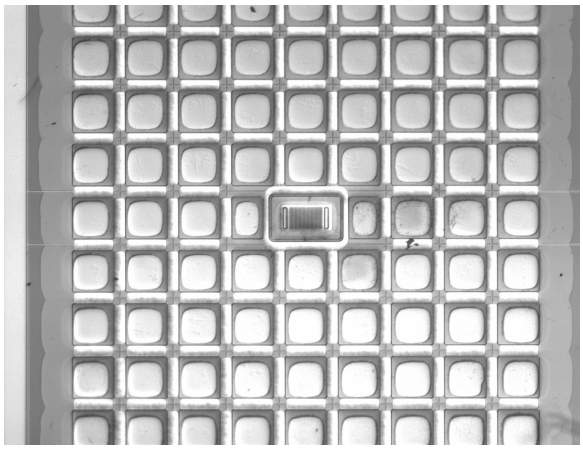

Figure 19 The 2100μm optical microphone

The final section in this chapter discusses the packaging of the silicon microphone membrane chips to form a complete front end package for experimental characterization.

Prototype Packaging of Completed Devices

As is, the microphone membranes fabricated on the silicon chips would not actually function as microphones, at least not with good sensitivity. The back-side of the chips are open so that an incoming acoustic pressure oscillation will act on both the front-side of the membrane and also on the back-side, thus producing no net pressure to drive the microphone membrane. A back-side cavity must be created to isolate the pressure on the back-side of the membrane from the acoustic pressure. However, it is typically not desirable to completely seal this cavity as this would create a pressure sensor responding at DC in addition to audio frequency acoustic signals. Since barometric pressure changes can be on the order of 50 Pa and acoustic signals are typically less than 1 Pa, a small barometric pressure vent hole is used to filter the response to these low frequency changes in pressure as they can damage the microphone membrane designed for a much smaller dynamic range.

This standard design is adopted here for the prototype packaging of the Sandia microphones. As shown in Figure 20, the air gap beneath the chip is created with a custom designed spacer fabricated with stereo lithography and a small window cut from a 0.5mm thick quartz wafer. The spacer is designed using the CAD program Solid Edge which is fed into GaTech's automated stereo lithography (SLA) tool. The design includes half circles cut out along regions of the spacer footprint which allow for the insertion of thin 100μm diameter tubing to create the barometric vent as shown in Figure 20.

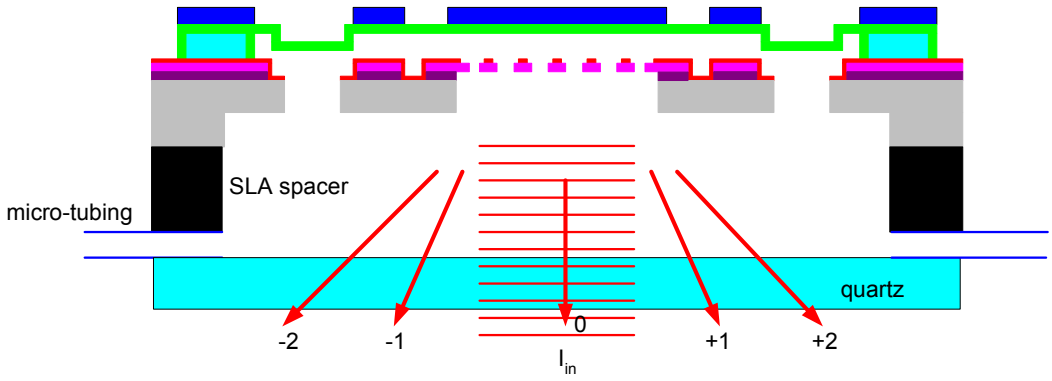

Figure 20 Prototype packaging scheme for the Sandia optical microphones

A picture of the completed spacer is shown in Figure 21. In addition to the small half circle cuts, a recess on the top of the spacer can be observed which aids in placing the 6.3X2.8mm Sandia chip. Figure 22 is a photograph of a completed assembly showing the SNL chip, the SLA spacer, the quartz window on the back-side of the spacer, and two channels of thin tubing. These three pieces are mounted together using UV cured epoxy. The epoxy is also used to fill any holes on the spacer not being used to house the tubing. As shown in the figure, this assembly is then mounted on a gold plated electronic chip carrier which provides leads for wire bonding as well as a convenient way to handle the completed front-end package. The chip carrier has a hole drilled through the center to provide optical access to the membrane and four holes in the corners which are used to mount this package to a hand-held experimental set-up described in detail in Chapter 5.

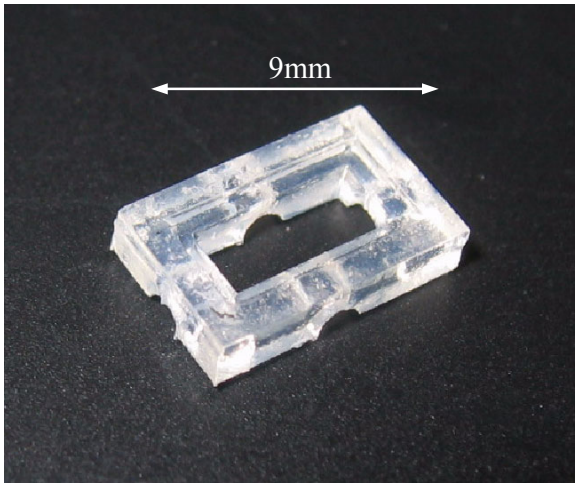

Figure 21 SLA spacer used for the optical microphone prototype package

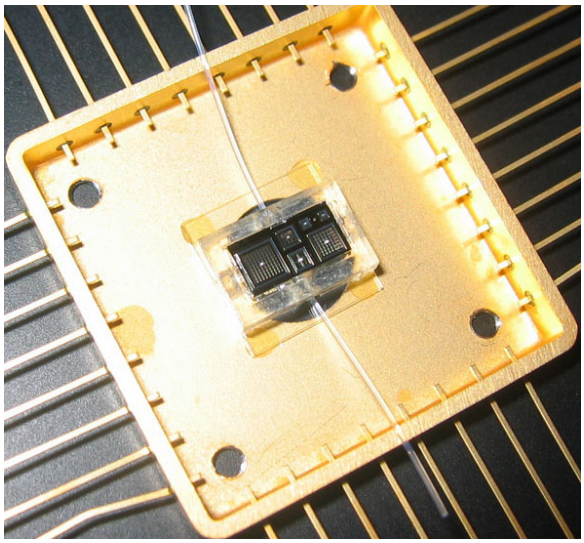

Figure 22 Photograph of a completed prototype package for the Sandia microphones

The modeling work presented in the following chapter shows the rationale for the particular designs of the optical microphones presented here. In particular, the model illustrates how the choice of membrane size, top electrode shape, and back-plate design provide prototype microphones with targeted mechanical compliance, resonant frequency, and actuation voltages.

CHAPTER 4

ACOUSTICAL AND MECHANICAL MODELING

Electrostatic actuation and dynamic response models for the microphone structures are presented in this chapter. The modeling work presented has two purposes: 1) to provide direction in the design phase and 2) to aid in the extracting of important physical parameters of the device structure during experimental characterization. Specifically, in the design phase, the model must be able to accurately assess the membrane deflection vs. DC bias behavior to ensure top electrode designs are sufficient for actuation. If the required voltage levels are too high, dielectric breakdown of the air gap can occur which typically leaves the membrane destroyed. There are also practical considerations which make low actuation voltages preferable. For example, the voltage level available on most microelectronic chips is typically 10 Volts – a constraint that should be considered for designs approaching full integration and commercial type packaging as required in hearing aids. Development of a finite element coupled field physics model is employed for this task due to the complicated membrane and electrode structure and the interaction between electrostatic forces with structural deformation geometry. A similar finite element model (FEM) is used to accurately map the membrane size, tension, and top electrode design to the microphone sensitivity and modal resonance frequencies. An equivalent circuit model for the dynamic response of the microphone that captures the essential interactions of the membrane structure with the air channels and cavities created from the prototype package is also presented. These three models also play an important role in the experimental characterization work presented in

Chapter 5 where they are fitted to experimental data to provide independent measures of the membrane sensitivity.

Electrostatic Actuation

Electrostatic actuation of the microphone diaphragm is important for several reasons. Simple control of the input DC actuation voltage allows the gap height to be controlled over a continuous range. By sweeping through a range of DC electrostatic actuation voltages while simultaneously recording the membrane deflection and the diffracted order intensities, the theoretical interference behavior laid out in Chapter 2 can be experimentally confirmed. More importantly, control of this voltage enables tuning of the displacement sensitivity whereby a gap height providing optical quadrature can be ensured. Dynamic pressure signals can also be applied electrostatically to characterize the frequency response of the device in both air and vacuum environments. The simplest model for electrostatic actuation is presented in the next section.

Review of the Parallel Plate Model

The simplest model for electrostatic actuation of a compliant diaphragm structure is the so-called parallel plate model. As the name suggests, the diaphragm is modeled as a flat rigid plate suspended from a spring with stiffness, K_{mem}, and resting in parallel above an additional flat rigid plate forming the bottom electrode. As illustrated schematically in Figure 23, the diaphragm typically consists of a nonconductive material for the membrane and an electrically conductive top electrode attached above. This is the case for the Sandia microphones, with silicon nitride as the membrane material and

polysilicon forming the top electrode. Taking the nonconductive membrane into account is important since it acts as a dielectric material and increases the total capacitance of the structure. For the structure shown in Figure 23, the parallel plate capacitance is

$$C = \frac{\kappa_{mem}\varepsilon_0 A}{\kappa_{mem} g + t_{mem}} \tag{30}$$

where κ_{mem} is the dielectric constant of the membrane material, ε_0 is the permittivity of free space, g is the gap height between the membrane and the bottom electrode, and A and t_{mem} are the area and thickness of the membrane.

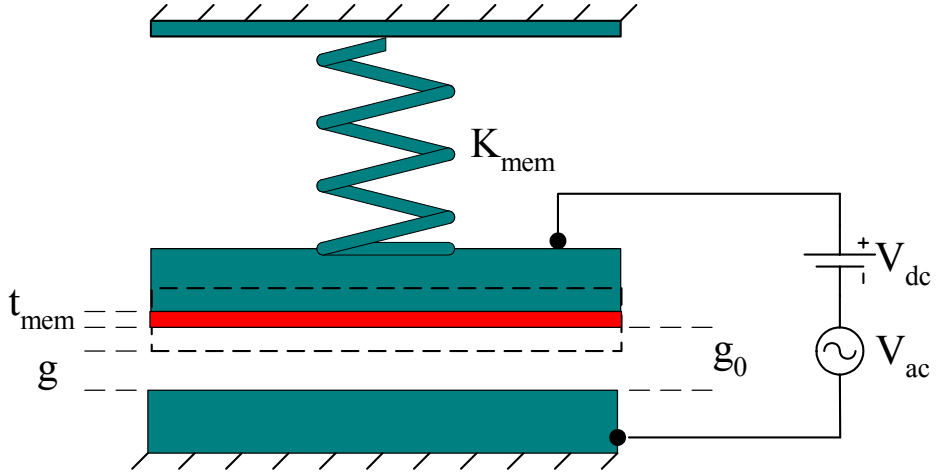

Figure 23 Schematic of the parallel plate model for electrostatic actuation

When an electrical potential, V, is applied across the two electrodes as shown in the figure, they become loaded with opposing polarity charges to generate an electrostatic attraction pressure. The magnitude of the pressure can be derived by first computing the uniform charge distribution for the given voltage and then integrating the forces across the plates caused by the Columbic attraction between these charges. Alternatively, a more elegant procedure is to start with an equation for the electrical energy stored in the capacitance and apply virtual work principles to obtain the pressure [30]. The principle

of virtual work states that, for the top electrode of a capacitor to be at static equilibrium while under an electric potential, the virtual work done by an external force, *F,* to move the membrane upwards through a virtual displacement, *dg,* must equal the virtual change in electrical energy, *dE,* caused by the same displacement, which implies that *F* can be obtained as *dE/dg.* The stored electrical energy in a capacitor is simply ½ CV^2, so computation of the downward acting electrostatic pressure, *P,* gives

$$P = -\frac{F}{A} = -\frac{1}{A}\frac{dE}{dg} = \frac{\kappa_{mem}^2 \varepsilon_0 V^2}{2(\kappa_{mem} g + t_{mem})^2} = \frac{C^2 V^2}{2\varepsilon_0 A^2} = \frac{Q^2}{2\varepsilon_0 A^2}. \tag{31}$$

where the last form provided is in terms of the charge, *Q,* across the plates. As suggested in Figure 23, the pressure generated by both static and dynamic signals is of interest. When the applied voltage in Equation 31 is written as the sum of a dc term, V_{dc}, and a dynamic term, *V(t)*, the electrostatic pressure is

$$P = \frac{C^2}{\varepsilon_0 A^2}[\frac{V_{dc}}{2} + V_{dc} V(t) + \frac{V^2(t)}{2}]. \tag{32}$$

Typically, the dynamic signals applied are much smaller than the DC bias. When this is the case, the last term in Equation 32 is negligibly small and a linear relationship exists between the applied dynamic electrical signal and the generated dynamic pressure.

A final issue which must be addressed before applying the parallel plate model to study electrostatic actuation of the Sandia devices is related to non-uniform top electrodes. The electrostatic actuation pressure across the plates only exists where regions of both a conductive top and bottom electrode exist across from each other. In the case of the Sandia devices and most other microphone designs, this is not the case since the back-plate is perforated. The most straightforward way to incorporate this complication into the model is to define a factor A_r as the ratio of the area where the

electrodes actually exist to the total are of the structure. For non-uniform top electrodes, this factor should preface the expression for the pressures in Equations 31 and 32 so that *P* represents the average the average pressure across the structure.

With this, the deflection of the membrane versus DC bias voltage can be studied. At static equilibrium, the electrostatic pressure must be balanced by the restoring force of the membrane as it displaces from an initial gap height of g_0 to a gap height of g as shown in Figure 23 and expressed in Equation 33.

$$0 = K_{mem}(g_o - g) - A_r \frac{\kappa_{mem}^2 \varepsilon_0 V_{dc}^2}{2(\kappa_{mem} g + t_{mem})^2} \tag{33}$$

Note that K_{mem} is defined here as the uniform pressure across the membrane per unit displacement and has units of *Pa/m*. Equation 33 is a third order polynomial in g with coefficients determined by the geometry, the material properties, and the input DC bias voltage. Many well known numerical techniques are well suited to solve for the roots and obtain g as a function of V_{dc}. Two of these roots are complex, and the third real root is the physical solution.

Despite its simplicity, the parallel plate model captures a fundamental phenomena of electrostatic actuation – electrostatic collapse. Since the electrostatic pressure grows large as the gap height becomes small, there becomes a point where the restoring force of the membrane is unable to balance the pressure. Mathematically, this results in no physical solutions to the polynomial in Equation 33. It can be shown that this occurs when the deflection is 1/3 of the total gap height [31, 32].

As argued previously, the collapse voltage is an important parameter for both regular capacitive microphones and the optical microphone under study. In addition to providing rough estimates of the collapse voltage during the design phase, the primary

usefulness of the parallel plate model is for extracting important parameters from the device by fitting experimental data to the model. However, because of the approximations inherent in the formulation, the model has limited use for both purposes. In addition to neglecting the fringing electric fields of the capacitance, the model neglects the fact that the membrane deflection is non-uniform. As a consequence, the charge across the electrodes is not uniformly distributed. A higher charge density must exist near the center of the membrane where the deflection is larger. This, in turn, results in a non-uniform pressure magnitude across the plates since the pressure is higher where more charge collects. Clearly, a numerical model incorporating electrostatic physics, the structural physics, and the coupling between the two is required to account for these complications. Such a model is described in the following section.

Coupled Physics Finite Element Model

Models based on the finite element method (FEM) have proven quite powerful for solving problems involving multiple physical domains. In particular, ANSYS offers a commercial multi-physics package which is well equipped with commands to handle the electrostatic modeling efficiently. The ESSOLV (electrostatic solve) macro available with ANSYS solves the electrostatic actuation problem with an iterative procedure as outlined in Figure 24. The first step is to create a generic unmeshed solid model defining the geometry of the structure. This solid model is then meshed with elements that have the capability to solve for the electrical charge distribution under a voltage load for any defined deformation of the structure. This model is an independently working file referred to as the electrostatics model in Figure 24.

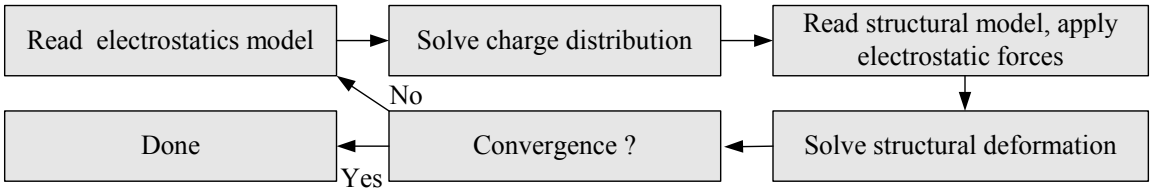

Figure 24 Flowchart summarizing the ESSOLV macro in ANSYS.

Next, the same generic solid model is meshed with structural elements that have the capability to solve for the deformation of the structure under any random loading. This is referred to as the structural model in Figure 24. The solution routine first solves for the charge distribution given the input voltage and then computes the electrostatic forces resulting from these charges to transfer to the structural model. Once these forces are written, the structural model is solved to obtain the resulting deformation. The new deformed geometry is then written to the electrostatic model where the charge distribution is recomputed. This solution procedure runs through several loops until the membrane converges to a deformed shape. At voltages near electrostatic collapse, the solution may require up to 15 iterations before converging. At voltages beyond collapse, the diaphragm deforms to a large unstable value and a maximum allowable displacement warning is returned by ANSYS [33].

A picture of the solid model created in ANSYS is shown in Figure 25. In this case, ¼ of the actual physical model is being used. When modeling in ANSYS, taking advantage of any symmetry the physical structure exhibits is desirable as this reduces the overall size of the model and the computation time. In this case, symmetry demands that the membrane and grating deform with zero rotation about x for the x=0 plane, and zero rotation about y for the y=0 plane. Including these as boundary conditions in the model

instead of solving the full model saves a great deal of computation time. It should also be noted that the gap height used to create the image of the model in Figure 25 is 20X the actual gap height of 2μm used in the simulations. This was done to make visible the back-plate and diffraction grating underneath the membrane.

The regions of the model that require meshing for the structural solution are the nitride membrane, the polysilicon top electrode, and the bottom diffraction grating electrode. The back-plate, which is assumed rigid, is distinguished from the compliant diffraction grating in Figure 25 by the different colors. The ideal element type for all of these structures is a SHELL element due to the their thin aspect ratios [34]. Indeed, the use of general solid elasticity elements is prohibited by this geometry. Since solid elements require aspect ratios close to unity, the thin layers used here produce an element count that exceeds the capabilities of ANSYS. The regions of the nitride membrane with the polysilicon top electrode can be modeled using a composite shell. In this case, the element SHELL181 is used. The model should also account for the fact that the nitride is under significant tension whereas the polysilicon top electrode attached to it has close to zero residual stress. If volumetric shell elements were able to be used, this could be done directly by reading initial stress values for each element with the ISTRESS (initial stress) command. To the best of the author's knowledge, this cannot be done to different layers within the same shell element. An alternative procedure used here is to assign mismatched coefficients of thermal expansion and apply a temperature loading to selectively induce stress in the nitride layer of the shell elements.

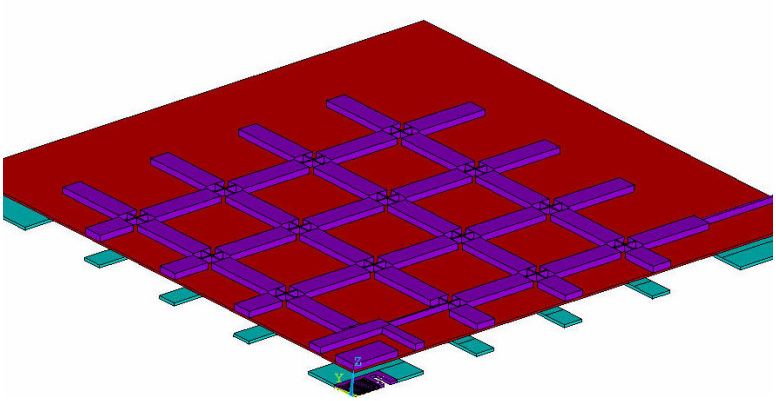

(a)

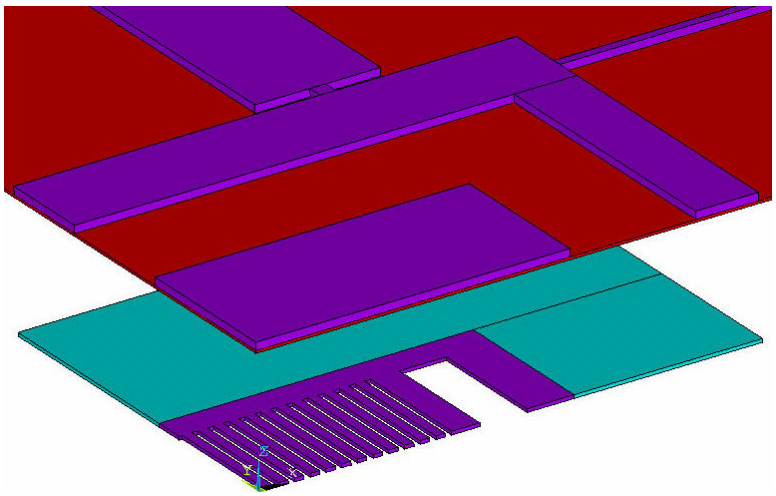

(b)

Figure 25 (a) The ¼ symmetry solid model used for electrostatic modeling in ANSYS and (b) a zoomed in view of the diffraction grating electrode

The solid model in Figure 25 represents the structure with all of its details including the thin 5μm stems connecting the larger polysilicon top electrode pads. These small features, however, force a fine, detailed mesh for the connectors themselves and the surrounding regions. Their inclusion results in a model with an element count five times the size of a model without the connectors. There is, therefore, motivation to leave them out of the model, especially when considering that even the simpler model can take up to

20 minutes to solve for a single voltage. A simple test was performed to assess the error in doing so. For a membrane with 100MPa of tension under a uniform pressure load, the difference in center deflection between a model with and without connectors is 5.6%.

The mechanical and electrical properties of the materials used are provided in the first few lines of the ANSYS programming language code written for the simulations, which is included in Appendix 1. The results from the model show that electrostatic pull-in behavior depends strongly on the value used for the residual tension in the nitride membrane. Sandia quotes a targeted value of 100MPa tension for this layer. Under these conditions, the model predicts a collapse voltage of 15 Volts which occurs after a membrane displacement of 1μm. There are no problems applying this voltage level, and the displacement range allows for more than a complete cycle of the interference curves to be traced with either HeNe lasers (λ~690nm) or VCSELS (λ~850nm) as the light source. In Chapter 5, measured electrostatic deflection data is presented against results from the FEM model described here. In this case, the tension in the nitride membrane is adjusted to fit the data, thereby providing an estimate of the membrane sensitivity. It is shown that a value of 75MPa for the tension produces an accurate fit to the data – which shows a collapse voltage near 12 Volts after a diaphragm displacement of 1μm. The corresponding mechanical sensitivity of the structure for this value is obtained with the FEM as 50.7Å/Pa. It should also be noted that the model predicts a mere $7x10^{-3}$μm upwards deflection of the compliant diffraction grating near collapse. This number is small due to the electrical isolation of the polysilicon optical reflector.

A final important detail to be discussed regarding the electrostatic model as well as the modal analysis presented in the following section concerns the necessity of using a

nonlinear structural solver in ANSYS. In order for the tension in the nitride membrane to affect its out of plane stiffness, the NLGEOM (nonlinear geometry) solver must be turned on. If it is not, no extra stiffening of the membrane caused by the initial stress will be observed. This is in agreement with the principle of superposition – in plane loading and in plane strain has no affect on out of plane loading or out of plane strain. This may initially seem counterintuitive to some readers since the mechanics equations describing the deformation of thin membrane structures are linear. The discrepancy is subtle and is related to boundary conditions. Figure 26 shows two cases.

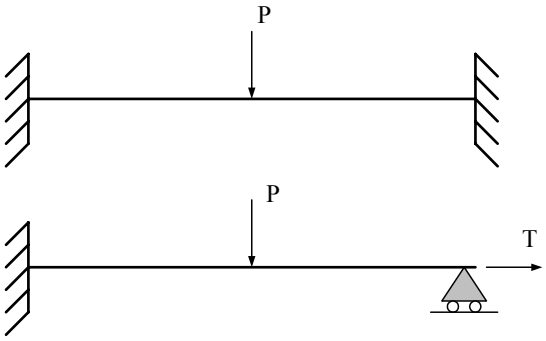

Figure 26 Schematic of two different boundary conditions for a structure under tension

In the first case, an initial tension is induced and the boundaries are kinematically constrained thereafter. Solving for deflection in this case is a nonlinear problem as the out of plane load P changes the tension. Iteration is required to solve for the equilibrium deflection. In the second case, the tension is held constant which results in a linear model. The common analytical linear differential equations for membranes correspond to the second situation. However, the results apply very well to the first case shown in Figure 26 for thin structures with large initial tension. Elements in ANSYS, however, are set-up for the most general case so a nonlinear solution must be implemented.

Dynamic Models

Two dynamic models are presented in this section. The first is a modal analysis of the microphone diaphragm. For a simple rectangular membrane under tension, this task can readily be handled with analytical equations. However, the top electrode adds both additional stiffness and mass to regions of the membrane. A finite element model is therefore used to perform the analysis. The most important modal frequency to assess is the fundamental, since this alone limits the bandwidth of the microphone. However, experiments in vacuum presented in Chapter 5 allow the first as well as several higher modes to be observed. This additional information can be used to verify the modeling results presented here. Adjusting the tension in the model to fit the first as well as the higher order modal frequencies provides an independent method for determining the microphone compliance.

The dynamic response of the microphone is complicated by the squeeze film damping in the thin air gap, which the modal analysis does not take into account. The DRIE holes eliminate the stiffening effect only up to a particular frequency which depends on the back-plate design. An equivalent circuit model is used to understand this effect as well as the factors determining the low frequency cut-off of the microphone.

Finite Element Model Modal Analysis

The solid model and shell elements created for the electrostatic model of the microphone membrane in ANSYS is also used for the modal analysis. As was done for the electrostatic model, a temperature loading is applied in an initial load step to create the tension in the nitride membrane. In order for ANSYS to take the tension into account

for the subsequent modal computations, the PSTRESS command must be issued. This command is identical in function to the NLGEOM command issued in the electrostatic model discussed above. Once this is done, the modal solution can be initiated with one of four different solvers available in ANSYS. The best solver to use depends on the application and type of model. ANSYS provides a discussion on choosing the appropriate solver in the help files [33]. In this case, a Block Lanczos routine is used to extract the first 14 mode shapes and corresponding mode frequencies as illustrated in Figure 27.

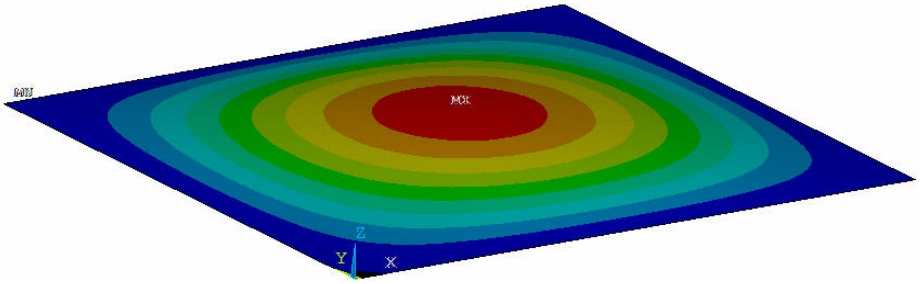

(a) f_1=43,739 Hz

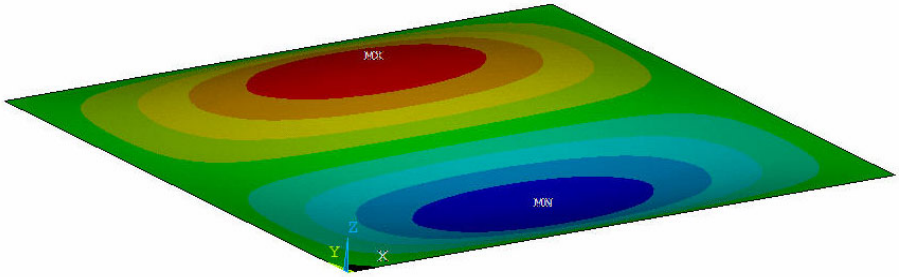

(b) f_2=69,668 Hz

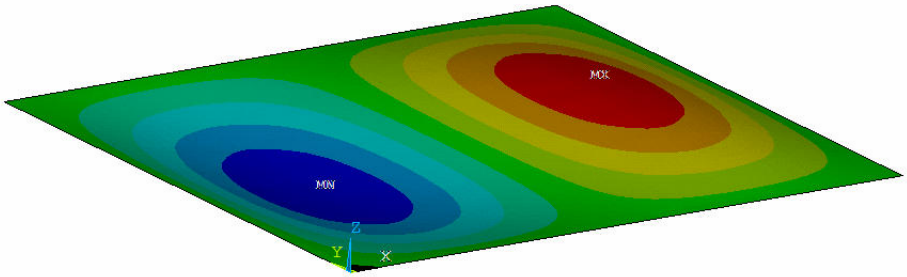

(c) f_3=69,901 Hz

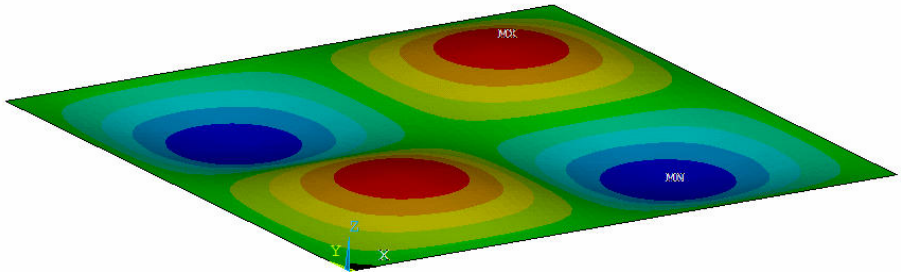

(d) f_4=88,601 Hz

Figure 27 FEM simulation of the first 14 mode shapes and corresponding mode frequencies of the microphone membrane

Figure 27 (continued)

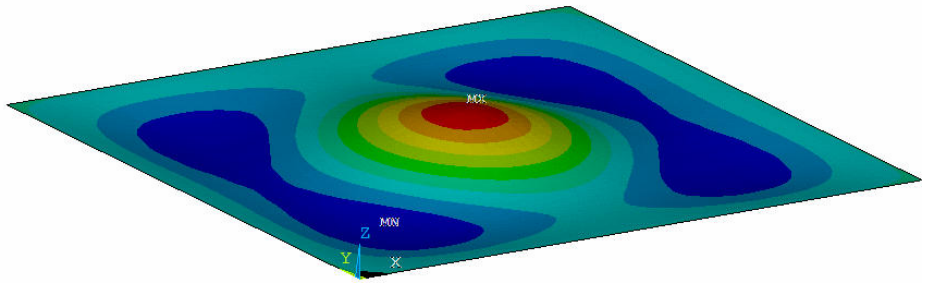

(e) f_5=98,165 Hz

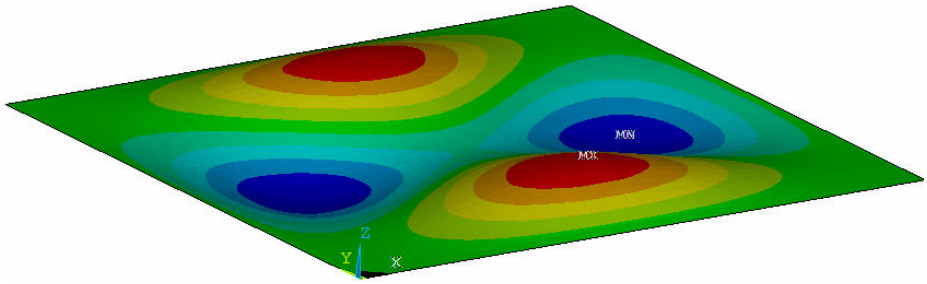

(f) f_6=99,437 Hz

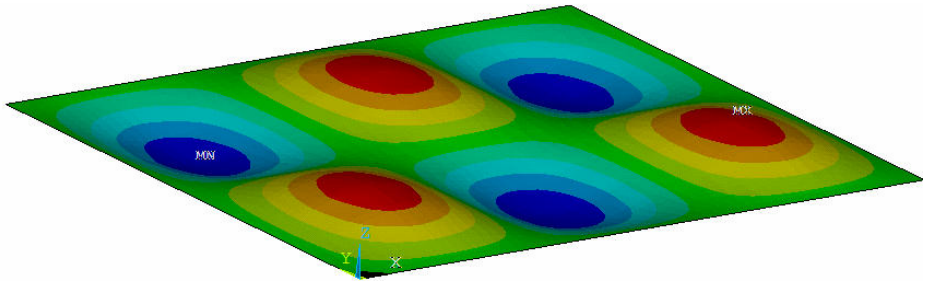

(g) f_7=113,849 Hz

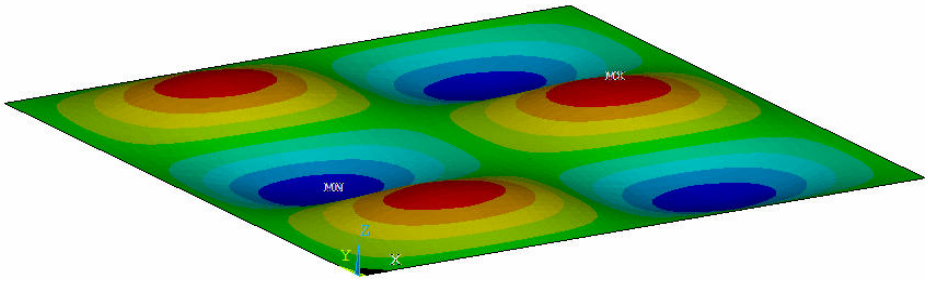

(h) f_8=114,209 Hz

Figure 27 (continued)

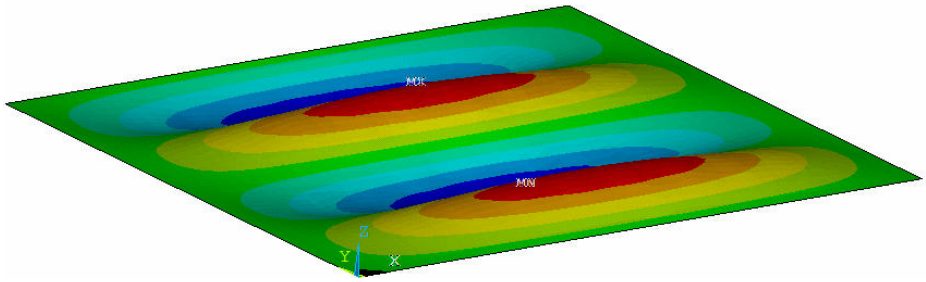

(i) f_9=131,181 Hz

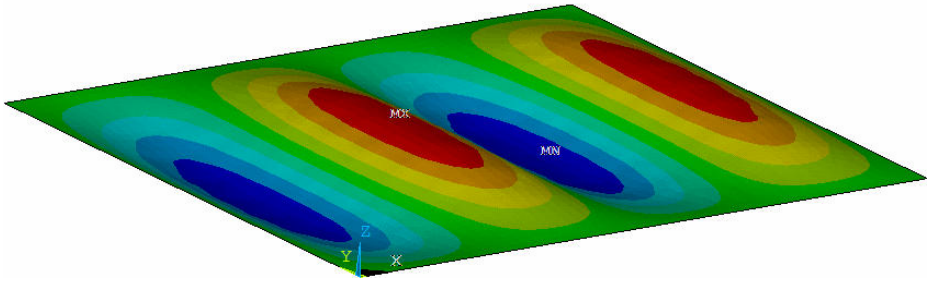

(j) f_{10}=132,024 Hz

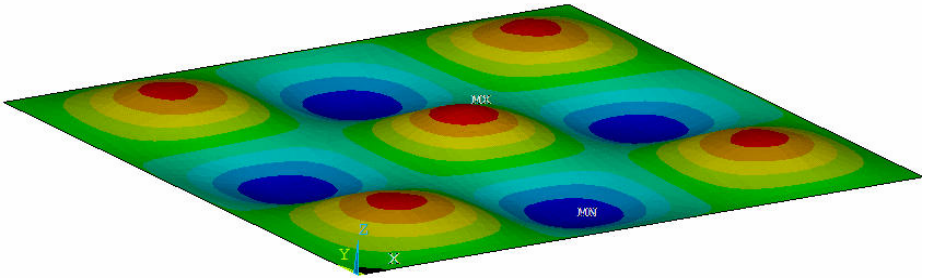

(k) f_{11}=133,793 Hz

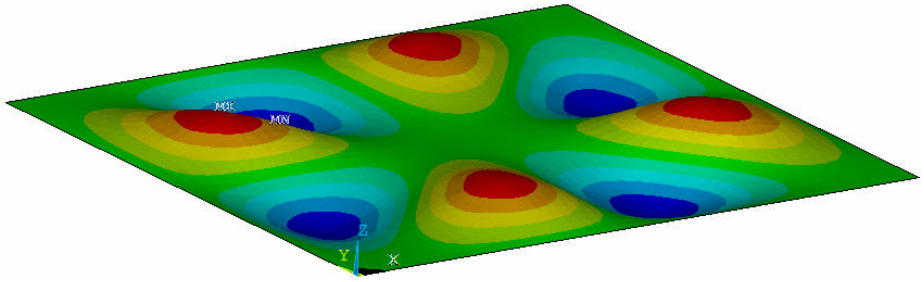

(l) f_{12}=142,580 Hz

Figure 27 (continued)

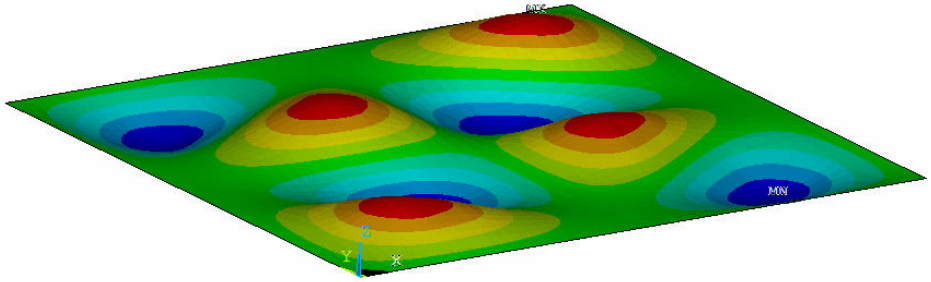

(m) f_{13}=142,898 Hz

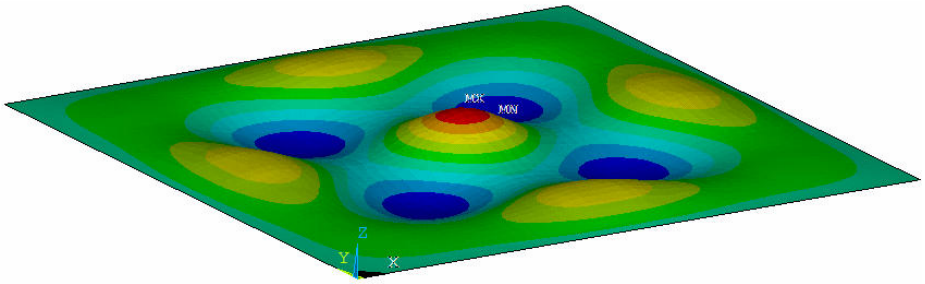

(n) f_{14}=160,295 Hz

As will be shown in Chapter 5, up to four resonance peaks can be observed when performing dynamic response tests of the membrane in a vacuum environment. The model presented here can then be used to fit these four resonant frequencies by adjusting the tension in the nitride in the membrane. The value for the tension can then be used to compute the membrane sensitivity to a uniform pressure load. This measure of the membrane sensitivity is independent of the measure discussed above, where the tension in the FEM is used to fit the electrostatic data. Recall that the modal analysis depends on the inertial properties of the membrane whereas the electrostatic simulations do not.

It is not expected that the first four resonances observed in the experiments are the first four modes shown in Figure 27. This is due to both the nature in which the

membrane is excited during electrostatic actuation and the nature in which the displacement is measured. In general, the vibration of a membrane at a particular frequency can have contributions from all modes. When a modal decomposition is performed, each mode's steady state contribution to the response is obtained by solving its single degree of freedom modal equation

$$\ddot{\eta}_i + \omega_i^2 \eta_i = \int_A P(x,y)\psi_i(x,y)dA\, e^{j\omega t} \tag{34}$$

where $\psi_i(x,y)$ and ω_i are the mode function and modal frequency, and $P(x,y)$ is the distributed pressure function determined by the electrode shape. The right hand side (RHS) of Equation 34 is the modal force acting on the i^{th} mode. The contribution of each mode depends on how close its modal frequency is to the excitation frequency and the magnitude of this modal force. Mode shapes that resemble the shape of the pressure function such as the first mode in Figure 27 dominant the response near their modal frequencies.

The pressure generated from electrostatic actuation resembles a uniform pressure in the sense that it is nearly symmetric across the membrane. Therefore, mode shapes with zero average displacement will have close to zero modal excitation. For example, it is not expected that the second, third, and fourth modes in Figure 27 will produce modal resonances in the dynamic response. A second requirement for appearing in the dynamic response is a nonzero displacement near the center of the membrane. As illustrated in the fabrication schematics in Chapter 3, the diffraction grating area is a small region of the overall diaphragm structure so the method essentially measures the displacement only at the center of the structure.

With this said, inspection of Figure 27 shows that the first, fifth, eleventh, and fourteenth modes should correspond to the first four modal resonances observed in the experiments. If the model is accurate, adjusting the tension parameter in the FEM should bring all four modal frequencies into alignment with the first four modal resonance frequencies observed in the experimental data. As will be shown in Chapter 5, this is indeed the case. A tension value of 80MPa was used to produce the results shown in Figure 27, and this value provides excellent agreement for all four frequencies. Table 1 below shows the comparison.

Table 1 Comparison between FEM and measured data of the first four observable mode frequencies for the 2100μm microphone.

	FEM	Experiment
Mode 1	43,739Hz	45,000Hz
Mode 5	98,165Hz	100,000Hz
Mode 11	133,793Hz	130,000Hz
Mode 14	160,295Hz	160,000Hz

The FEM also shows that when the nitride is under this tension, the microphone has a mechanical sensitivity of 44.3Å/Pa. This value is within 14% of that determined using the electrostatic fit. The modal method used here is expected to provide the better estimate since the density, which is well known, is the only other significant variable fed into the model. In addition to the nitride tension, the electrostatic model is sensitive to values for the dielectric constant of the nitride as well as the initial gap height.

It should also be noted that during electrostatic actuation of the membrane, a small upwards pressure is applied to the diffraction grating from the fringing electric fields. This could therefore potentially cause an observable resonance in the response. A modal analysis of the diffraction grating however shows that the first mode is at 883kHz

which is, as expected, much higher than the membrane modes. Figure 28 shows the fundamental mode shape of the diffraction grating.

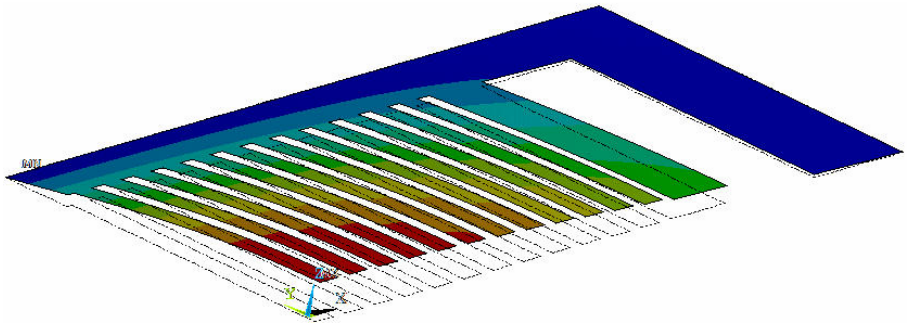

f_1=883,176Hz

Figure 28 FEM results showing the fundamental mode of the diffraction grating.

For completeness, it should be noted that Equation 34 is valid for an analysis without damping. With certain assumptions regarding the damping, the only modification needed to the modal decomposition is the inclusion of a modal damping term in Equation 34. It should also be noted that this equation is correct if the modes have been mass matrix normalized. ANSYS returns such normalized modes in preparation for use in a stead state harmonic response analysis to an arbitrarily shaped pressure input swept over a desired frequency range, which provides the dynamic response of the structure. In this case, however, simulating the full response of the membrane in this manner is superfluous since the results depend primarily on the damping, which is difficult to model even for the response in vacuum. Squeeze film damping in the thin 2μm gap adds additional complexity to the microphone response in air. For these reasons, a simple model based on equivalent circuits is presented which captures many important features relevant to the design of the optical microphone.

Equivalent Circuit Models

Equivalent circuit models have long been used to provide an understanding of the complicated workings of acoustic transducers. These models are based on the fact that many systems, regardless of the physical domain, can be modeled as networks with effort and flow variables. These variables are defined such that their product gives the power transferred to the portion of the network the effort acts across. For example, in electrical systems, these variables are voltage and current. Equivalent circuit models make explicit the nodes in the network where the flows divide but effort remains equal, and conversely, where effort divides but flows remain equal. Using electrical circuits as an analogy, conservation considerations dictate the enforcement of Kirchhoff current and voltage laws for the network.

Figure 29 (a) shows the prototype package of the microphone with the relevant dynamic entities labeled and (b) shows how these entities are connected in an equivalent circuit model. P_{front} is the pressure acting on the microphone membrane. This can represent the pressure from either acoustic or electrostatic excitation. The volume of air displaced by the membrane while responding to this pressure must either 1) compress in the 2μm air gap with compliance and resistance represented by C_{gap} and R_{gap}, 2) push the diffraction grating electrode with compliance C_{back} in towards the cavity region, or 3) flow through the back-plate holes with resistance R_{back} to the cavity with compliance C_{cav}. Of course, combinations of all three are allowed. This is made explicit in the parallel channels of the equivalent circuit model in Figure 29 (b). Finally, whatever volume of air enters the cavity must either compress there or leave through the acoustic vent with resistance R_{vent} where the outside pressure is seen. For acoustic excitation, P_{vent} will be

the same as P_{front}. For electrostatic actuation, the end of the vent will be a pressure release and P_{vent} is assumed zero.

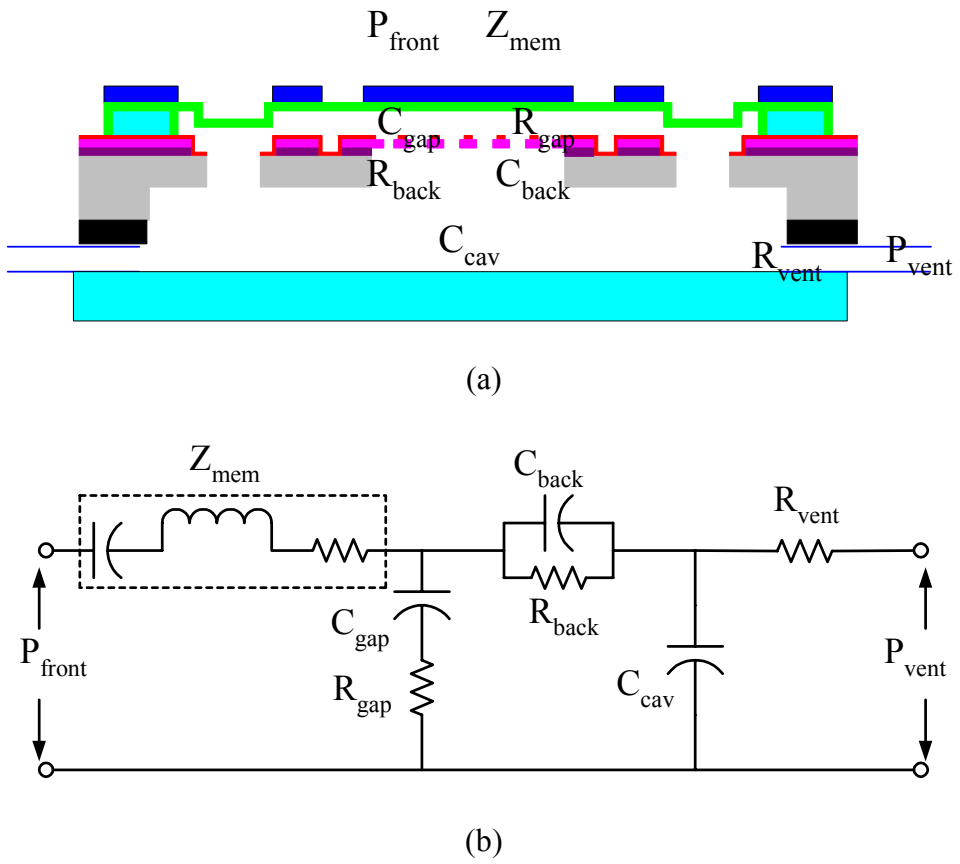

Figure 29 (a) Schematic of the microphone package with the relevant dynamic entities labeled and (b) equivalent circuit schematic for (a)

It is clear from this discussion that the flow variables in the circuit analysis are volume flow rates. Therefore, all impedances computed should be acoustic impedances, defined as the pressure over volume velocity relationship for the particular element. The membrane properties are readily estimated using the finite element results above. The compliance of the diffraction grating is also computed using a FEM analysis. For the designs presented in this thesis, this grating is very stiff so it is, for all practical purposes, completely rigid. The compliance of the gap and cavity air volumes is computed

assuming isentropic compression of the air as an ideal gas [35]. The vent resistance can be estimated using a simple equation for laminar flow in a round channel. The total resistance associated with the flow through the back-plate holes is difficult to approximate. This resistance is caused by the flow of the fluid as it displaces laterally towards the holes, and also by the resistance of the fluid displacing through the holes. This parameter affects the response in profound ways as the following analysis shows. The details related to computation of the impedance values are provided in Appendix 3, which is a MatLab code used to solve the circuit.

Solving the circuit in Figure 31 to an acoustic input requires the superposition of solutions obtained using each of the two pressure sources. However, the acoustic pressure acting at the vent and the vent resistance are essentially decoupled from the remainder of the circuit for the operational frequency range of the microphone. The vent resistance and the cavity compliance are, however, responsible for determining the low frequency cutoff of the microphone. An equivalent circuit model for low frequencies is shown in Figure 30 to illustrate why this is the case.

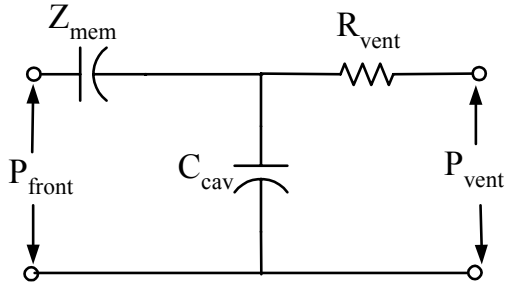

Figure 30 Low frequency equivalent circuit of the model in Figure 29

At low frequencies, the air can oscillate freely through the DRIE holes in the back-plate so the gap capacitance and the back resistance have been taken out. Under

these conditions, the pressures in the gap and cavity are the same and the driving pressure of the microphone membrane is $P_{front} - P_{cav}$. The cavity pressure can be obtained by summing the value obtained using P_{front} as the source with P_{vent} shorted, and the value obtained by solving with P_{vent} as the source and P_{front} shorted. The cavity pressure resulting from the first solution is zero at low frequencies due to the parallel vent resistance, and remains very small across all frequencies since the membrane is much stiffer than the cavity. The cavity pressure is therefore determined by the second solution, which is essentially a voltage divider between the vent resistance and the cavity capacitance since the membrane is, again, much stiffer than the cavity. The simple voltage divider shows that cavity pressure is then

$$\frac{P_{cav}}{P_{vent}} = \frac{1}{1 + j\omega\tau} \tag{35}$$

where ω is the acoustic frequency and $\tau = R_{vent} \times C_{cav}$ is the time constant for these two elements. Since the vent pressure is the same as the front pressure for acoustic excitation, the ratio of the driving pressure of the microphone membrane, P_{drive}, to the acoustic pressure at the front can be expressed as

$$\frac{P_{drive}}{P_{front}} = 1 - \frac{P_{cav}}{P_{front}} = (1 - \frac{1}{1 + j\omega\tau}) \tag{36}$$

Equation 36 describes the low frequency cutoff behavior of the microphone package. For example, at the frequency where the magnitude of this ratio is 0.7 the microphone will register a pressure 3dB lower than the actual acoustic pressure in the field With the exception of this low frequency cut-off, which does not exist for the electrostatic actuation case since the vent pressure is shorted, the response for both types of excitation are expected to be the same

The major factor affecting the response at frequencies above the low frequency cut-off of the microphone is the back-plate resistance. At higher frequencies this resistance prevents the air in the gap from entering the large cavity and the large stiffness of the air gap adds in series with the membrane impedance to stiffen the response. Results of the circuit simulation for four values of the back-plate resistance are shown in Figure 31.

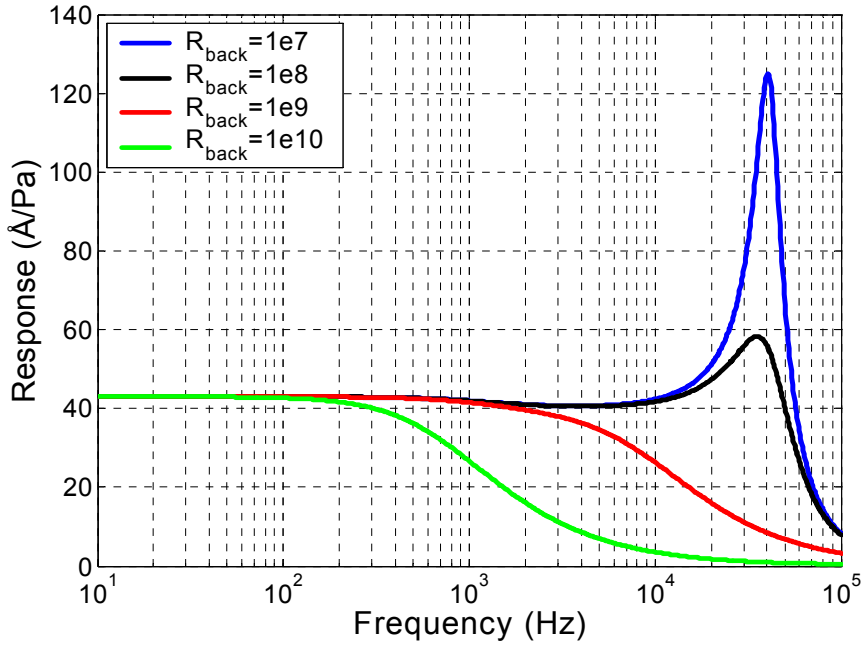

Figure 31 Equivalent circuit simulation of microphone response for 4 back-plate resistances

In the first case, the cutoff caused by the back-plate is above the fundamental resonance of the membrane, so the bandwidth of the microphone is limited by this resonance. In the second case, the back-plate resistance takes effect very near the resonance and serves to dampen the peak substantially. This is the ideal back-plate design since the resonance peak is eliminated but no bandwidth is sacrificed. The third

and fourth back-plate resistances produce a cutoff of the microphone before resonance and a substantial portion of the bandwidth is sacrificed. The units for the resistance values presented in Figure 31 are Pa×sec/m^3. An important observation is the fact that the values used in the plot are each separated by an order of magnitude. The implication is that, in the design phase, the model used to estimate this effect must only be accurate within an order of magnitude to tailor the response as desired. This is fortunate considering the difficulty involved in modeling this phenomena. More sophisticated efforts employing computational 2-D and the 3-D models based on the full set of Navier Stokes equations are the subject of recent investigation [36-39].

A primary utility of the models presented in this chapter is fitting with measured data. The detailed experimental characterization of the microphone is the subject of the next chapter.

CHAPTER 5

CHARACTERIZATION AND MODEL VERIFICATION

This chapter presents the detailed characterization of the optical microphones. A portable hand-held test bed is constructed with integrated PDs and amplifiers to allow the microphone to be transported and tested in several environments – including a custom designed bench top vacuum chamber and an anechoic acoustic test chamber. The characterization begins by calibrating the displacement sensitivity of the microphone. This requires precise measurement of the microphone diaphragm deflection under DC bias loading which is accomplished with a non-contact white light optical profilometer. This, in conjunction with measurements with the hand-held set-up, provides experimental validation of the theoretical interference behavior presented in Chapter 2. With the displacement sensitivity characterized, the dynamic response of the device to both electrostatic and acoustic excitation is studied. The response of the microphone together with the internal noise measurements presented in the subsequent chapter fully characterizes the performance of the optical microphone.

Development of a Hand-held Microphone Test Bed

The hand-held test bed constructed for the characterization of the diffraction based optical microphones is shown in Figure 32. Two views are provided to aid in the observation of the fundamental components. An ultra low noise (ULN) laser diode module from Coherent Inc. is secured firmly to a custom designed aluminum box. Light from the laser passes through an aperture machined in the box, as labeled in Figure 32

(b), entering a hollowed out Al spacer which serves as the lens holder as shown in (a). A spherical lens at the end of the holder focuses the beam to a sub - 50μm spot onto the back of the particular microphone membrane tested. The front end package, as described in Figure 22, is mounted on a miniature XY stage, as shown in Figure 32 (b), to allow the diffraction grating to be precisely positioned on top of the laser spot. Note that the package is mounted with a tilt via small spacers causing the diffracted field to reflect back on an angled plane. All of the diffracted orders can then be focused down to a line with the cylindrical lens before hitting the PD array which is placed below the lens holder and mounted on another miniature XY stage.

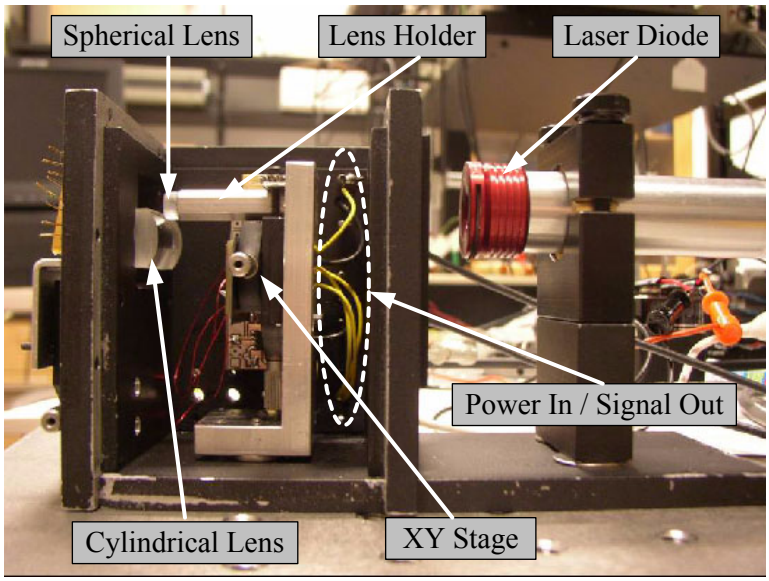

(a)

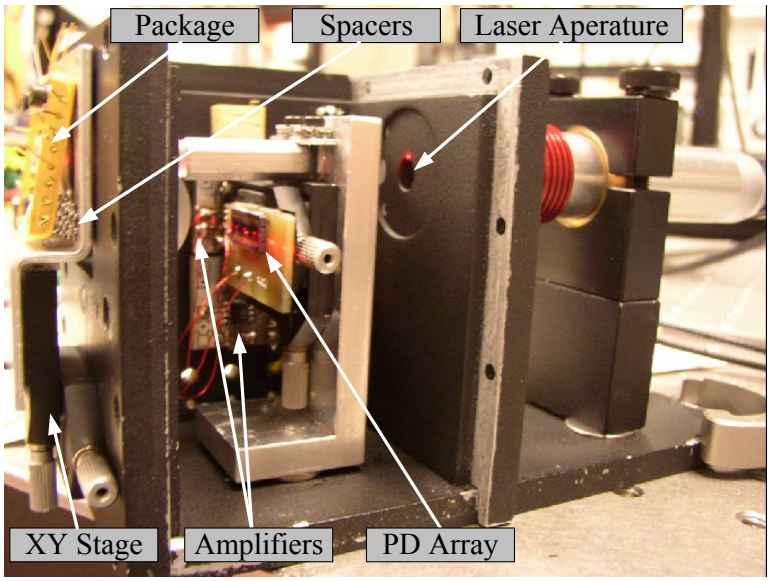

(b)

Figure 32 Photographs of the hand-held experimental characterization test bed (a) from the side and (b) from an angle

The set-up is designed to capture the zero order and both first orders. The PD array used contains 12 independently working cells. The array was therefore wired to create 3 independent elements by connecting the smaller elements in series. The zero and

first orders can be observed illuminating the PD array in Figure 32 (b). Figure 33 shows a zoomed in view where a white piece of paper is used to make the light more visible. In this figure, the -1 and zero orders are on the PD array, and the +1,2,3 orders are incident on the paper.

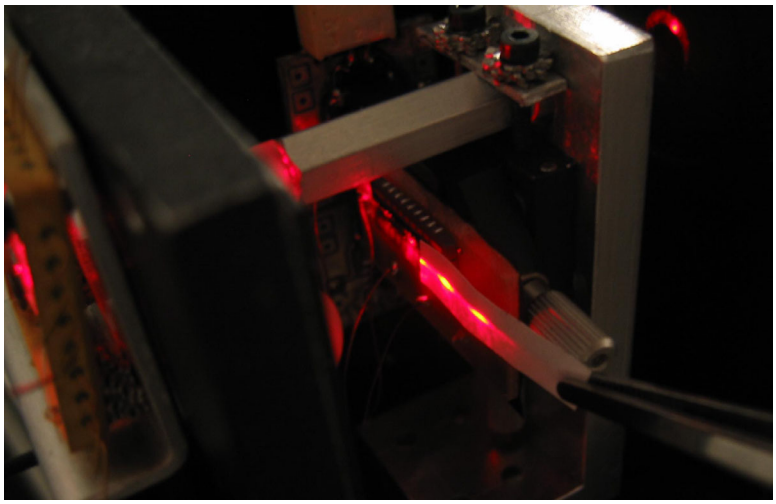

Figure 33 Photograph of the PD array illuminated with diffraction orders

The photocurrents from the zero and +1 order are each fed to transimpedance amplifiers mounted on the back wall of the test set-up as labeled in Figure 32 (b). The zero order amplifier is given a fixed gain of 100kΩ whereas the first order amplifier is designed with a variable gain with a range from 0-1MΩ. The variable gain allows the first order signal amplitude to be equalized to the zero order signal for differential order detection and laser noise reduction. The voltage outputs from the amplifiers are fed to SMA connectors mounted on the opposite of the box wall (not shown in figures). The power cabling for the amplifiers is also routed through small holes drilled in the box wall. Finally, it should be noted that the top and remaining side of the box are not shown in the

figures as they would hide the components from view. A closed and electromagnetically shielded box is formed with the addition of these two final pieces.

The remainder of this chapter presents several measurements that provide important optical and mechanical properties of the microphone structure. In these experiments, the hand-held test-bed interacts with a variety of standard laboratory test apparatus. Figure 34 is a schematic of the most general experimental set-up used for the device characterization. The microphone package, laser diode, photodiodes, transimpedance amplifiers, and SMA connectors are enclosed inside a dotted line to emphasize that these components are part of the hand-held test assembly. The output voltages from the zero and first order amplifiers are monitored with an oscilloscope, and the microphone diaphragm can be actuated acoustically or electrostatically using both DC signals from a voltage controller and AC signals generated with a function generator. As shown in Figure 34, these signals are combined using a simple mixing circuit which is discussed further in the following sections. All of the test equipment can be controlled with the bench-top computer shown in the figure using standard GPIB and HP VEE software to automate data taking.

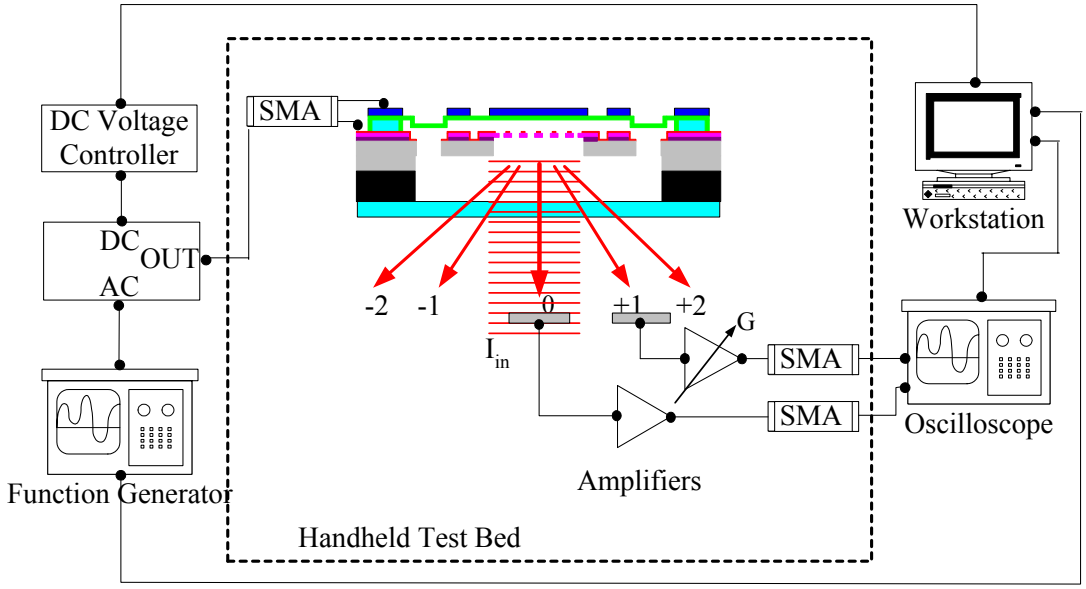

Figure 34 Schematic of the experimental set-up used for device characterization

Displacement Sensitivity Calibration

Calibrating the displacement sensitivity of the optical microphone is a two step process. First, the diaphragm deflection vs. electrostatic actuation voltage data is obtained with a Wyko external white light interferometer. The hand-held experimental set-up is then used to record the intensities from the diffraction orders as the DC bias is swept again through the same range of actuation voltages. This allows the diffraction order intensities to be mapped to the diaphragm deflection thus experimentally tracing the interference curves theoretically described in Chapter 2.

Electrostatic Pull-In Measurements

The Wyko optical profilometer used is part of the MiRC at Georgia Tech. The functioning of the tool resembles that of a microscope, with different magnification

objectives placed above a motorized stage. For these experiments, the front end package shown in Figure 22 is mounted flatly and securely on the profilometer stage. A low noise, high resolution DC power supply is used to adjust the voltage across the two gold plated leads on the package that are, in turn, wire bonded to the top and bottom electrodes of the microphone membrane. The profilometer can then be used to profile the membrane topography for any given voltage.

Figure 35 shows the scan of a 2100μm membrane. Only a quarter of this membrane can be obtained in a single scan due to a limited range on the available objectives. This, however, is sufficient for the purpose. The image in Figure 35 is color mapped such that each color corresponds to a different elevation. Note that the measurement is clearly able to distinguish between regions of the top electrode and regions of the nitride membrane.

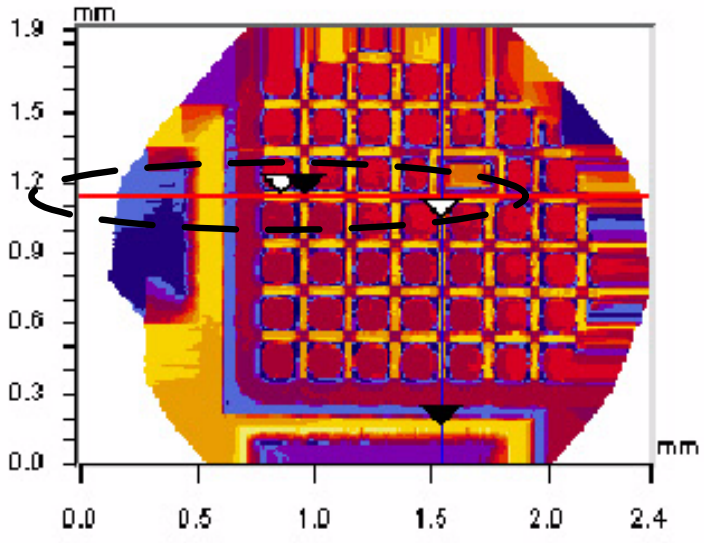

Figure 35 Topographical scan of the microphone diaphragm via white light interferometry

More detailed information is obtained by 2D profiling the data which is one of many post processing features of the tool. The cross section used for the 2D profile is highlighted in Figure 35 with a dotted line. Figure 36 shows an example of such a profile taken at a DC bias value of 10V with various features of the diaphragm labeled. The membrane anchor is clearly observed at the outer most region of the scan. Immediately to the right of the anchor, however, is a large gap in the profile. These gaps are regions of the nitride membrane where the top electrode does not exist. Since the nitride is optically transparent, the profilometer cannot measure the membrane deflection in these regions. The top electrode and optical reflector regions which are labeled in Figure 36 (a) are more than sufficient for profiling the membrane deflection. The center deflection of the membrane is recorded as the anchor height minus the reflector height. For the scan shown in Figure 36, a deflection of 0.5µm is measured.

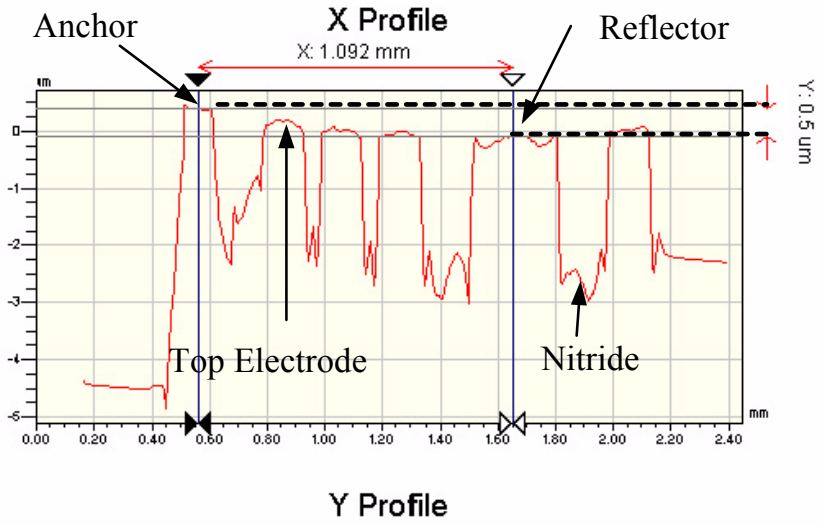

Figure 36 2D Profile of the microphone diaphragm deflection at a DC bias of 10 Volts

The gap height is recorded in this fashion for several other bias levels to trace the behavior over the complete actuation range. This measured data is shown as black circles

in Figure 37 where the gap height is plotted versus the DC bias voltage. As discussed in Chapter 4, a third order polynomial provides a theoretical basis for a least squares fit to the data. This fit is also shown in Figure 37 and provides an accurate way to interpolate the data. The remaining set of points on the plot is the FEM simulation results for this 2100µm membrane, which show excellent agreement with the measured data. As noted in Chapter 4, the tension value used for the nitride in this simulation is 75MPa. The corresponding diaphragm sensitivity for this value as determined by the FEM model is 50.7Å/Pa.

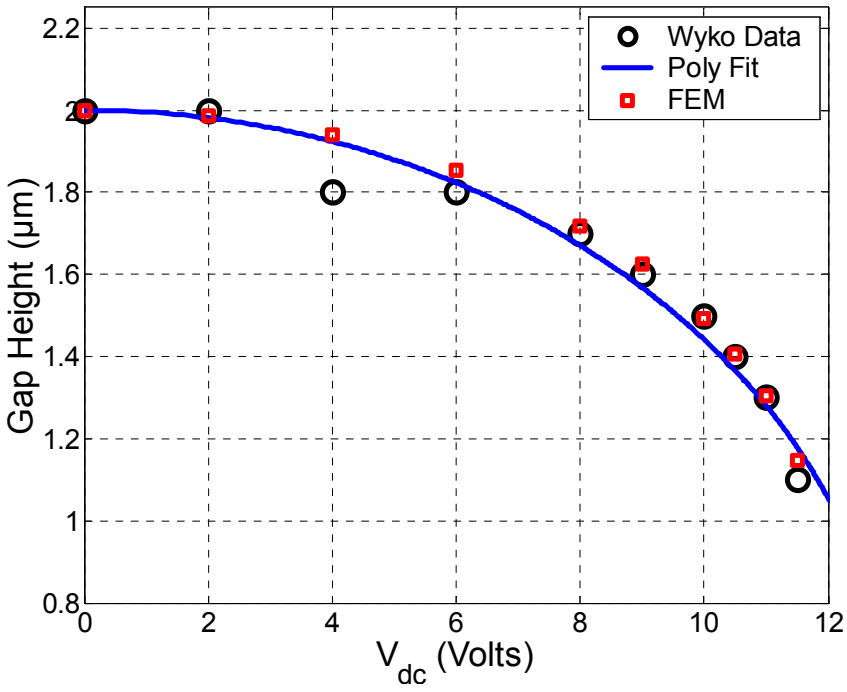

Figure 37 Measured data and FEM results for the electrostatic pull in of a 2100µm Sandia microphone.

The next section explains how this data, together with data obtained from diffraction based detection, provide the information required to experimentally trace the

optical interference curves and therefore calibrate the displacement sensitivity of the method.

Experimental Validation of Interference Curves

The same front end microphone package used for the electrostatic pull-in measurements is then returned to the hand-held test bed as shown in Figure 32. The same range of actuation voltages are used to pull the diaphragm in towards the substrate as the PD amplifier outputs for the zero and first diffracted orders are measured with an oscilloscope as suggested in Figure 34. In these experiments, the computer is programmed to send a voltage sweep from 0-10V to the DC power supply while storing each measured voltage value from the oscilloscope. The results of this experiment are shown in Figure 38. The transimpedance amplifiers used in the set-up have an inverted output which is why the voltage values are negative. In this case, the more negative the voltage value the higher the diffracted order intensity.

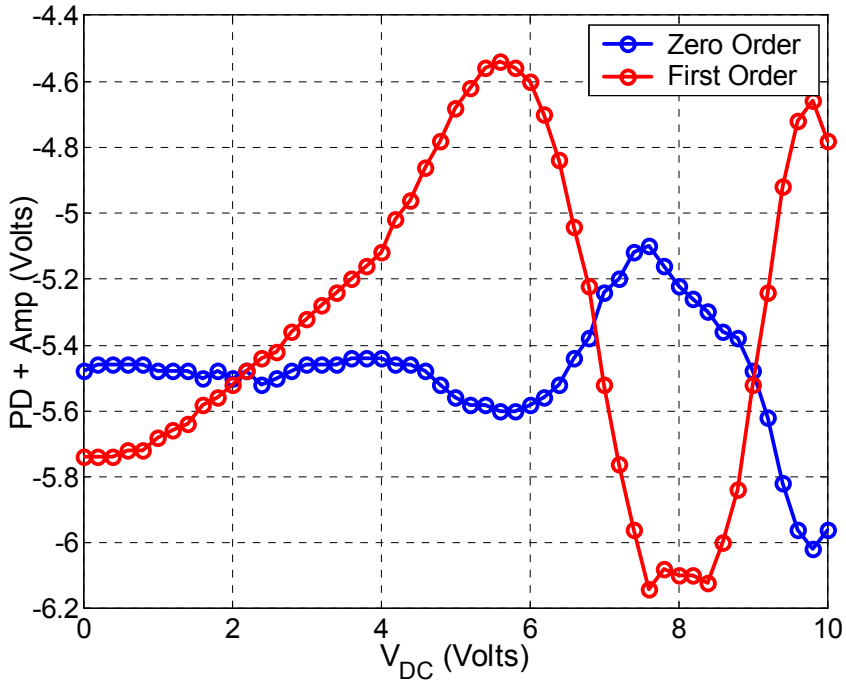

Figure 38 Measured intensities of the zero and first diffracted orders versus electrostatic actuation voltage

Note that these curves are cyclical but not periodic due to the nonlinear relationship between pressure and voltage during the electrostatic actuation. In order to obtain a plot of the diffracted order intensities versus gap height, the information in Figure 37 is utilized to map the DC bias actuation voltages to the corresponding gap. The result of this mapping operation is shown in Figure 39. Several features are worth noting. First, the period of the interference curves match well with theory. The distance between the peaks and the troughs of the curve is approximately 0.15µm. This can be estimated, for example, by taking note of the peak in the first order intensity at a gap height of 1.85µm and the trough in the first order intensity at a gap of 1.7µm. Recall that this change in gap should correspond to ¼ of the optical wavelength, which in this case is 0.15µm for the 630nm wavelength HeNe laser being used.

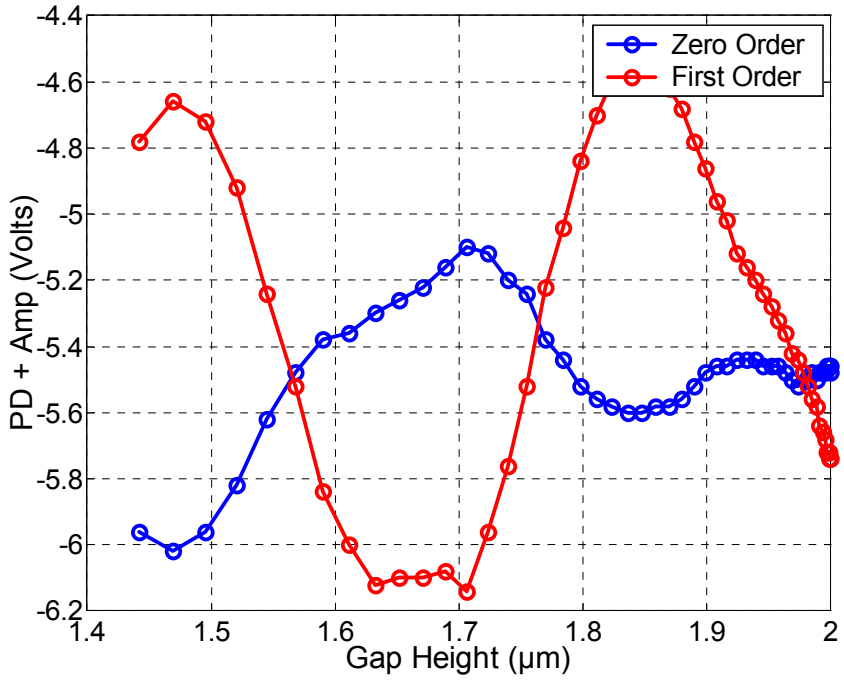

Figure 39 Mapping of the measured diffraction order intensities to the membrane gap height

A second important observation is the fact that the swing in intensity of the zero and first diffracted orders are not equal and they do not come close to zero intensity. Recall that, according to Equations 10 and 11, all orders other than the zero order should go through zero intensity at gap heights of λ/2 multiples since the grating system acts like a perfect mirror in this situation regardless of the grating period and fill factor. This implies that there are significant optical losses in the system. The intensity swing of the zero order is particularly lower than expected – with a value of approximately 20%. It is expected that these curves can be improved a great deal with further post processing of the Sandia chips. It is possible that the gold sputtering did not result in a total reflective layer as it might have been too thin. The same data taken on Al cMUT membranes provide much better optical results as presented in Chapter 7.

The data in Figure 39 can be used to compute the displacement sensitivity versus gap height with simple differentiation. The results are shown in Figure 40. When differential order detection is used, the actual displacement sensitivity is the sum of the values for each order.

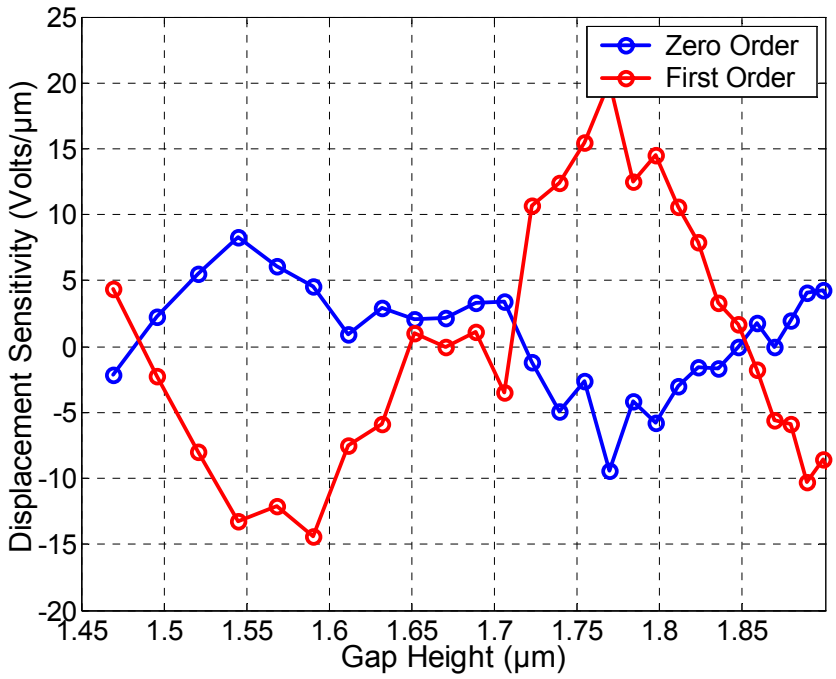

Figure 40 Displacement sensitivity of the Sandia microphone versus membrane gap height as computed from Figure 39

In the next section, electrostatic actuation is used to apply dynamic signals to the device for characterization in vacuum and air environments.

Dynamic Response to Electrostatic Input

Measuring the dynamic response of the optical microphones in vacuum is important because it allows the dynamics of the mechanical structure alone to be

observed without complications caused by squeeze film damping in the back-side cavity or acoustic radiation impedance on the front-side of the device. This data is important because it aids in confirming and disconfirming hypothesis explaining certain anomalies of the dynamic response air, which is of course the more relevant case for the microphone application. For a properly sealed microphone cavity, the electrostatic response should be identical the response to acoustic signals over the audio frequency bandwidth. This is shown to be the case in the final section of the chapter.

Experimental Set-up

Applying dynamic pressure across the microphone membrane requires the application of a dynamic voltage signal on top of a larger DC bias level. The simple circuit used to combine the DC bias with the dynamic signal is shown in Figure 41. The DC bias is again applied with the HP DC power supply and the AC signal is applied with a function generator. The source impedance of these two pieces of equipment is small and is therefore not represented in the circuit.

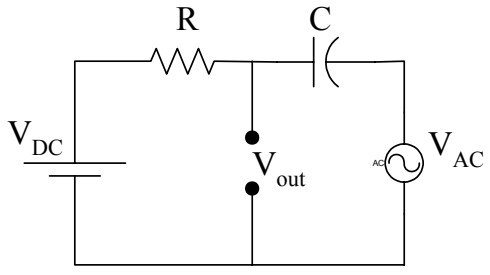

Figure 41 Circuit used to combine the DC bias with the dynamic voltage signal

A simple Thevenin analysis as depicted in Figure 42 is useful for examining the low frequency cutoff behavior of the AC source and the source impedance caused by the two mixing components.

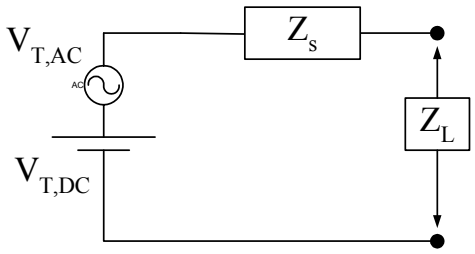

Figure 42 Thevenin Schematic of the mixing circuit used for electrostatic excitation

The analysis provides the following expression for the source terms and the source impedance:

$$V_{T,DC} = V_{DC} \tag{37}$$

$$V_{T,AC} = V_{AC}[\frac{R}{R + 1/(j\omega C)}] \tag{38}$$

$$Z_s = \frac{R}{1 + j\omega RC} \tag{39}$$

At high frequencies, the open circuit AC voltage is exactly as applied by the function generator. There is, however, a low frequency cutoff to be aware of if too small a capacitance is used as Equation 38 shows. For these experiments, a 2μF capacitor and a 100kΩ resistor are used which enables signals as low as 10Hz to be applied. In order to ensure that this open circuit voltage is applied across the microphone, which is represented as the load in Figure 42, the microphone impedance must be large compared to the source impedance of the mixing circuit. The electrical impedance of the microphone is the high impedance presented by its very small capacitance, and the source

impedance of the mixing circuit above the low frequency cutoff is the impedance of the capacitor used in the circuit as can be verified in Equation 39. Therefore, in order to apply the voltage across the microphone to generate electrostatic pressure signals, the capacitance used in the circuit should be large compared to the device capacitance. As can readily be verified with Equation 30, the capacitance of the diaphragm structure is in the sub pF range, so the 1μF capacitor used in the circuit is sufficiently large. Dynamic signals can therefore be applied from 10Hz to MHz frequencies with this set-up, with the upper frequency limited only by the electronic test equipment.

The mechanical response of the microphone is defined as the diaphragm displacement resulting from an applied uniform pressure. The membrane displacement can be assessed from the displacement sensitivity calibration measurements. The remaining task is to relate the applied dynamic voltage signal to pressure. This can be estimated with Equation 32 which is based on the parallel plate approximation. A more accurate way, however, is to employ results from the finite model simulations and the profilometer measurements illustrated in Figure 37. When results of the FEM modal analysis are compared to resonant peaks in the dynamic response as described in Chapter 4, the membrane compliance is determined as 44.3Å/Pa. Therefore, the membrane deflection resulting from a particular DC bias voltage as determined from the data in Figure 37 can be converted to an equivalent uniform pressure acting across the membrane. The result of this mapping is shown in Figure 43 where pressure is plotted versus DC bias.

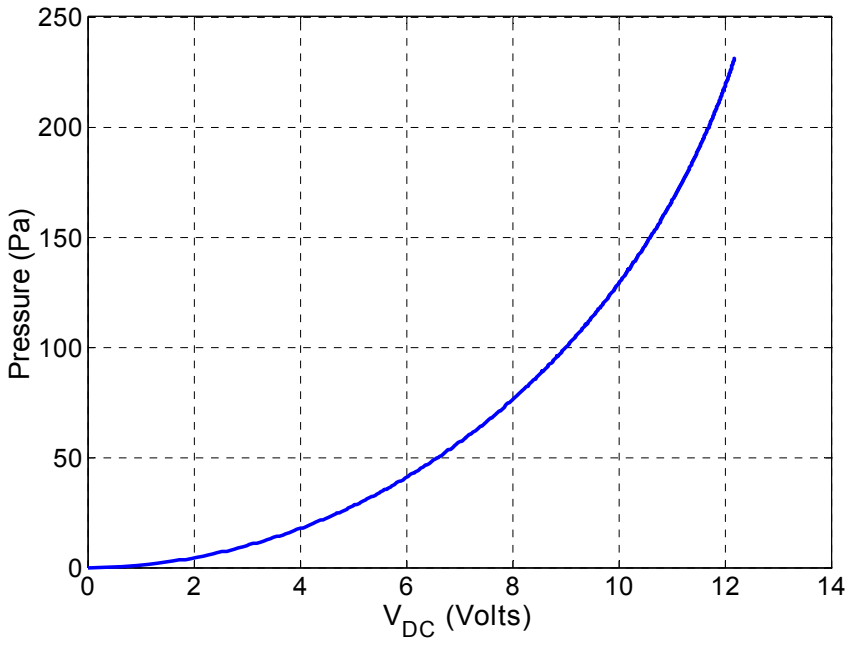

Figure 43 Plot of the applied electrostatic pressure vs. DC bias voltage

The relationship is nonlinear as expected. With this information, the dynamic voltage signal can be scaled by *dP/dV* to obtain the dynamic pressure, where the derivative is evaluated about the particular DC bias level being used. The experimental set-up and procedure discussed in this section are applied to measurements in vacuum and air environments.

Measurements in Vacuum

A small bench top vacuum chamber was constructed for the measurements in vacuum. Figure 44 shows a photograph of the experimental set-up used for taking the data. The chamber was custom designed to accommodate the electrical connections required for the experiments. This was accomplished by using an Al plate as the bottom component of the structure with several holes drilled to route standard BNC cabling, a

power cable for the laser driver, and a swage lock to connect to a vacuum pump. An additional tapped hole is used to house a vacuum gauge capable of measuring in the 0.1 to 50torr range. All of these holes are on the back-side of the plate so they cannot be seen in Figure 44. The chamber lid and sealing ring were borrowed from a commercially available vacuum set-up. Figure 44 shows the test bed and microphone package mounted inside the chamber while pumped down to a pressure of 5.0torr, the minimum pressure achievable with this set-up.

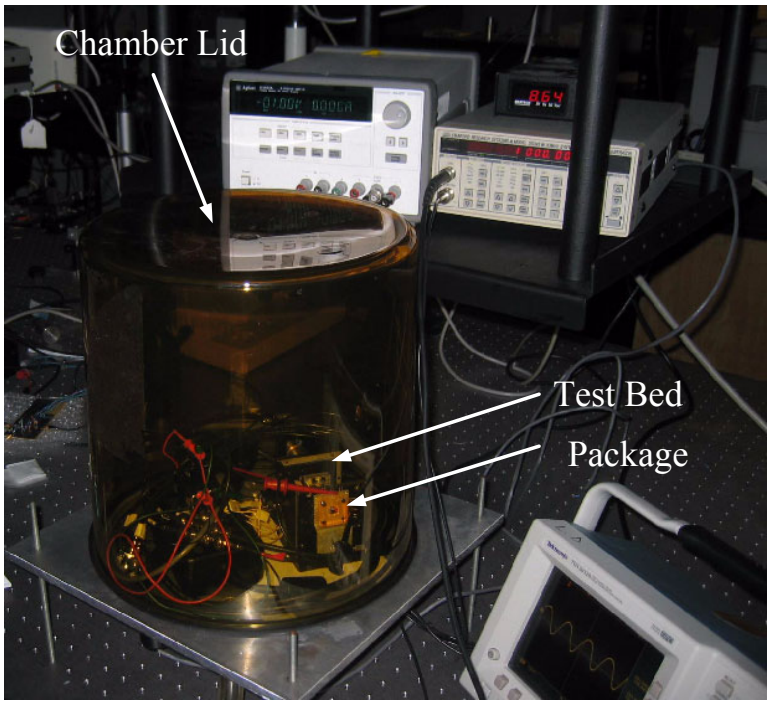

Figure 44 Photograph of the experimental set-up used for dynamic response testing in vacuum

The dynamic response is obtained by measuring the displacement of the microphone diaphragm resulting from an applied impulse pressure. An impulse of 1.6×10^{-6} sec duration is generated using a single cycle of a 600kHz square wave from the function generator operating in tone burst mode. This input pressure and the resulting

output signal from the photodiode monitoring the first order intensity are captured with a digital oscilloscope. The experiment is repeated with a burst frequency of 10Hz and the results are averaged to enhance the signal to noise ratio of the experiment. The input voltage and PD signals are then converted to units of pressure and displacement, respectively. Time traces of these signals are plotted in Figure 45.

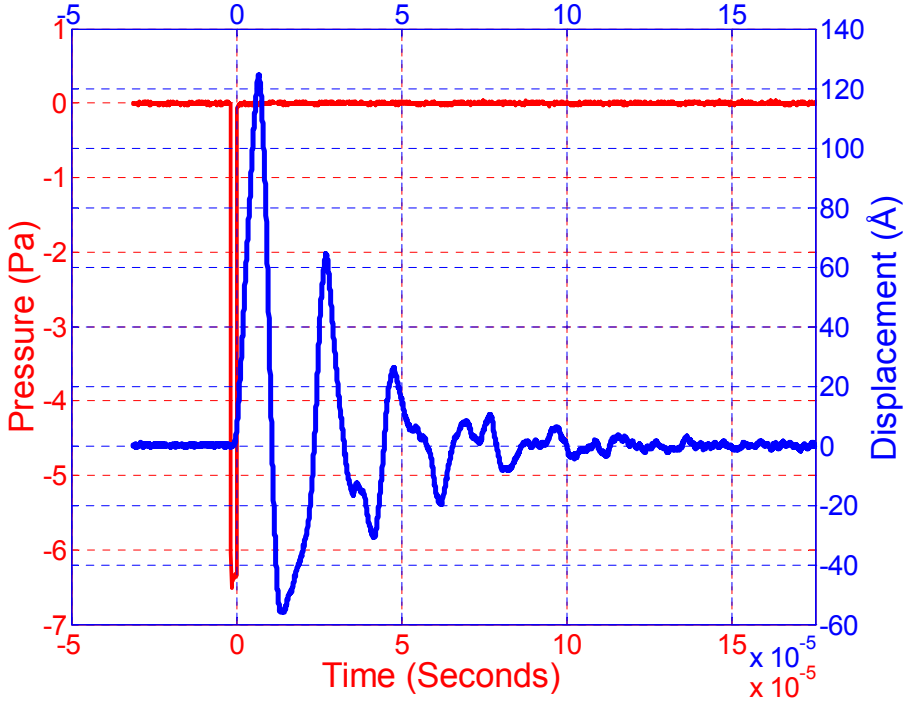

Figure 45 Time traces of the applied impulse pressure and resulting impulse response of the microphone in vacuum

The impulse pressure in Figure 45 is negative because it is referenced to the DC pressure caused by the DC portion of the electrostatic input, which in this case is 4.8V. It is clear from the response that both a fundamental and higher order modes are represented. This is made explicitly clear when the frequency response is computed as the ratio of each signal's discrete Fourier transform (DFT) coefficients. The digital data from the oscilloscope is transferred to MatLab for this computation, where the built in

FFT function is used. The response is complex containing both magnitude and phase information. The magnitude of the response is shown in Figure 46.

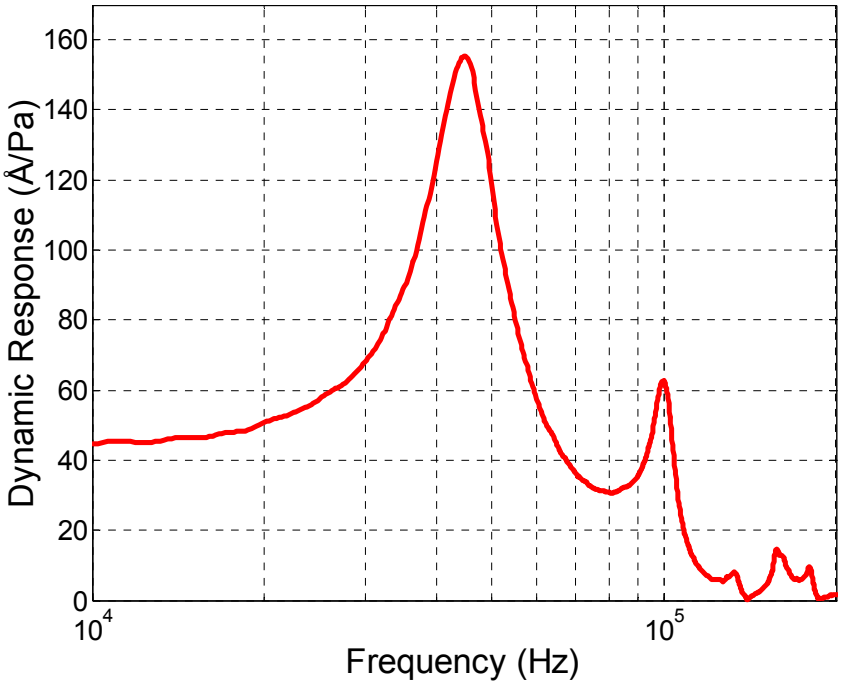

Figure 46 The dynamic response of the microphone in vacuum

At low frequencies, the response approaches a static membrane compliance close to 40Å/Pa as expected, suggesting that the displacement sensitivity has been performed accurately. Five modal resonances can be observed in the plot at frequencies reported in Table 1. Resonance is defined here to occur at frequencies where the response exhibits a local maxima. The fundamental resonance occurring at 45kHz provides an upper limit to the useful bandwidth of the microphone. As discussed in detail in Chapter 4, the remaining four peaks observed do not correspond to the four subsequent modes of the diaphragm as only modes that are excitable and have nonzero displacement at the center can be observed. It is argued in Chapter 4 that the three resonances following the

fundamental correspond to the fifth, eleventh, and fourteenth modes. The FEM results presented there agree well with the measured data in Figure 46.

The compliance of electrostatically coupled devices can become strongly dependent on the DC bias voltage near collapse due to a phenomena called electrostatic softening, which is commonly exhibited in cMUTs [5, 40]. To this point, the causality involved in electrostatic actuation has been the following: the applied voltage creates a charge, the charge creates a pressure, and the pressure displaces the membrane diaphragm. However, if the voltage across the diaphragm is held constant as the membrane displaces downward due to either external pressure or its own momentum, additional charge is forced to collect on the diaphragm. As the last form in Equation 31 makes explicitly clear, the electrostatic pressure acting on the diaphragm depends solely on the charge and nothing else. Therefore, the downward displacement results in the application of a downward electrostatic pressure that acts in an opposite direction of the restoring spring force of the diaphragm. The value of this negative spring is proportional to the *dQ/dg* behavior of the diaphragm capacitance, which can become large at large DC bias values. This electrostatic softening behavior is not observed for devices operating under constant charge, such as most capacitive microphones, as the last form of Equation 31 again makes clear.

As might be expected, this softening effect lowers the resonance frequency and enhances the compliance near DC. This is demonstrated with the optical microphone by simply repeating the impulse experiment with larger DC bias levels applied. Three different cases are shown in

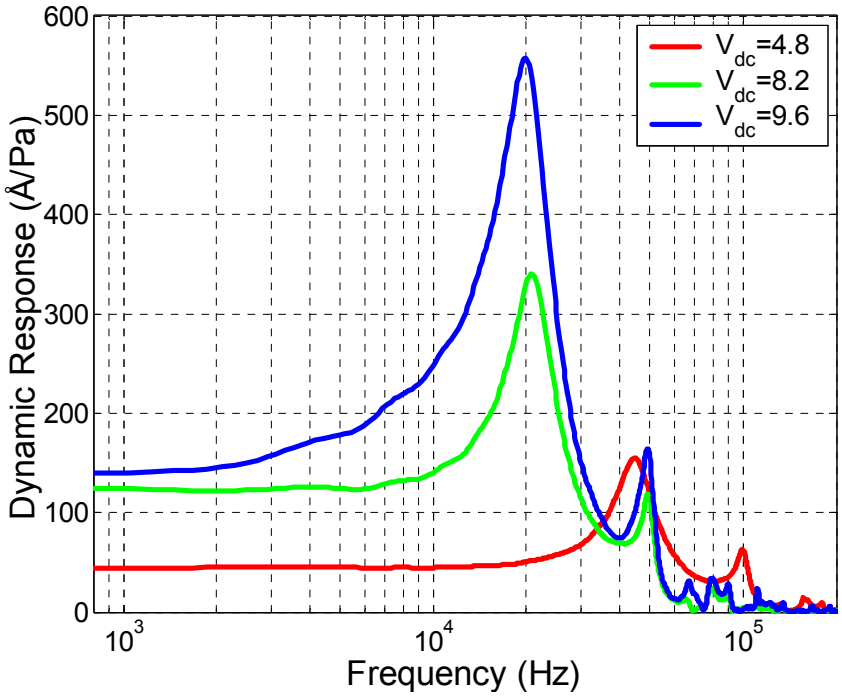

Figure 47 Dynamic response of the microphone in vacuum at different bias levels

The fundamental resonance of the membrane shifts from 45kHz down to 20kHz when a DC bias of 9.6V is used, lowering the resonance by more than a factor of ½. Based on a simple first order model for the membrane, one would expect the diaphragm compliance to quadruple which is indeed the case as can be observed from the low frequency compliance value of 150Å/Pa. In future designs, this electrostatic softening feature may be useful for creating microphones with adjustable bandwidth and sensitivity. However, as experiments presented in the next section make clear, the bandwidth of the current design is limited by the presence of the air in the back-plate to frequencies well below the fundamental resonance of the diaphragm.

Experiments in Air

The frequency response of the structure in air to electrostatic excitation can be obtained straightforwardly in a manner identical to that for the vacuum case. Time traces of the impulse pressure and the resulting impulse response of the microphone are shown in Figure 48.

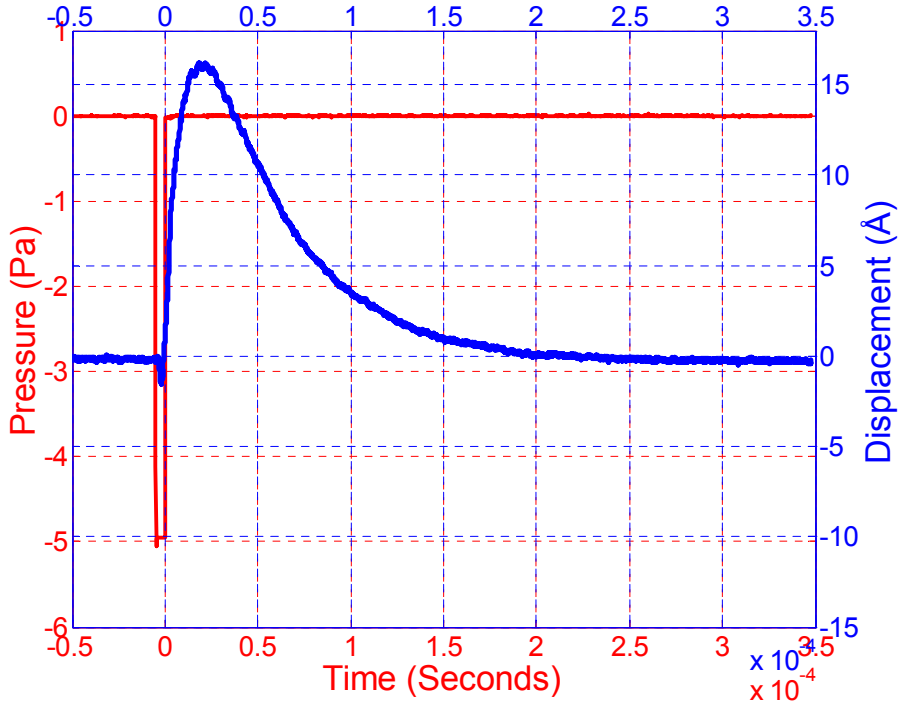

Figure 48 Impulse response of the microphone diaphragm in air

In vibratory systems terminology, the response shown in Figure 48 is referred to as over damped as the damping is strong enough to prevent the momentum of the membrane from executing even a single vibratory oscillation. This data is used to compute the frequency response of the microphone in a manner identical to that above for the vacuum case. The magnitude of this response is plotted for three different membrane–back-plate gap heights Figure 49.

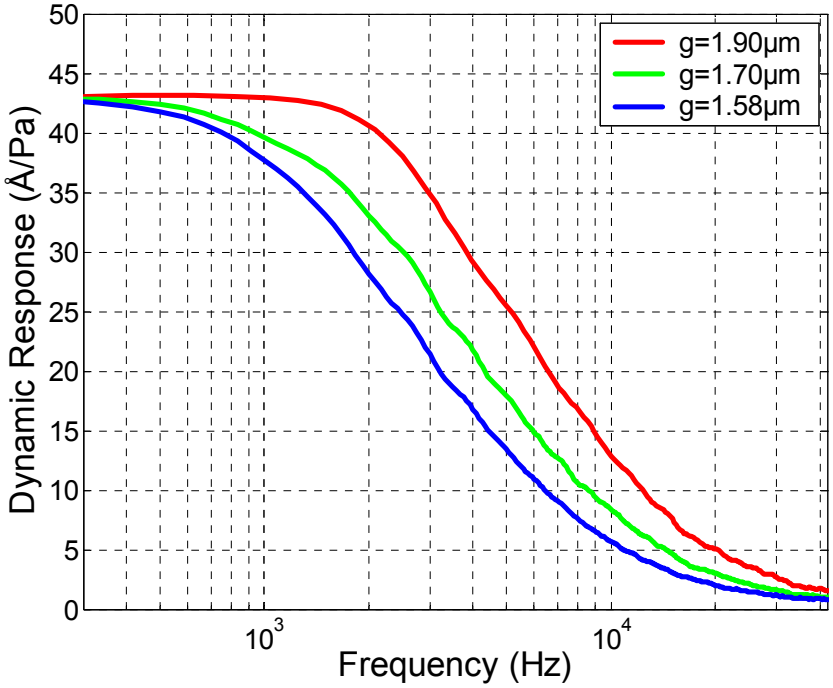

Figure 49 Dynamic response of the microphone in air for three different gap heights

For the first gap height of 1.9µm shown in red, a substantial roll off in the response begins around 2kHz. The modeling work for the dynamic response in air presented in Chapter 4 suggests that this roll off is due to squeeze film effects in the thin air gap. At lower frequencies (below 2kHz), the air in the thin gap has time to displace radially and exit to the large back-side cavity via the DRIE holes in the back-plate. At higher frequencies, however, the substantial flow resistance caused by the close proximity boundaries of the back-plate and the diaphragm prevent the air from displacing and it instead becomes trapped in the thin gap. At these frequencies, the air compresses and adds substantial stiffness to the structure.

This hypothesis is supported by several observations. First, it can be certain that the mixing circuit presented in Figure 41 is not causing a cutoff in the applied voltage

amplitude since the simple Thevenin analysis shows that no upper cutoff frequency is expected. Furthermore, if the phenomena were related to the electrical input circuitry, it should also appear in the vacuum tests. The roll-off is therefore due to a mechanical or acoustical effect related to the presence of the air. In addition to the squeeze film effects in the gap, these effects could potentially be related to radiation impedance on the front-side of the membrane or the air in the much larger back-side cavity formed by the SLA spacer and the quartz window. As the modeling work presented in Figure 31 suggests, the cutoff frequency in the response should depend on the flow resistance associated with the diaphragm – back-plate gap. This resistance, in turn, is strongly dependant on changes in the gap height for thin gaps. To a first order, this resistance scales as $1/g^2$ [41]. This hypothesis therefore implies that the cut off frequency in the response should depend on the gap height which can be controlled via the applied DC bias voltage. Since neither the radiation impedance nor the stiffness of the back-side cavity depend on the gap height, the hypothesis can be confirmed by performing the impulse tests at several DC bias values and observing the shift in the response. The results of these tests are also plotted in Figure 49 for gap heights of 1.7μm and 1.58μm where the expected shift is indeed observed.

As confirmed in the following section, the dynamic response to acoustic signals is expected to be similar to the response to the electrostatic signals presented here. The roll off is therefore an undesirable feature since it limits the bandwidth of the microphone to only a portion of the audio range. This resulted from not having an adequate model for mapping the back-plate geometry to the back-plate flow resistance in the design phase of

these microphones. As discussed in Chapter 4, such a model should be accurate within an order of magnitude to enable designs with diaphragm resonance limited bandwidths.

Dynamic Response to Acoustic Signals

The electrostatic responses measured in air and vacuum in the previous section are useful for developing an understanding of the device properties, but the response to acoustic excitation is most pertinent to the microphone performance. For a free-field microphone, the acoustic response is defined as the response of the microphone to the acoustic pressure that exists in the field before the insertion of the microphone and related packaging, which can cause significant scatter at high frequencies where the size of the microphone becomes comparable to the acoustic wavelength [35]. For commercially packaged measurement microphones, thin pre-amp packages are placed behind the microphone head so that scattering is mitigated over the frequency range of interest. The hand-held test-bed is not, of course, optimized for minimal acoustic form factor. The acoustic response is therefore expected to resemble the flat electrostatic response at low frequencies when properly sealed, but is expected to show some complexities at high frequencies due to acoustic scattering.

The experimental set-up used for the acoustic response tests is shown in Figure 50. To eliminate reflections from surrounding surfaces and simulate the free-field test condition, the measurements are performed in an anechoic chamber which is part of the Integrated Acoustics Laboratory (IAL) at Georgia Tech. A white noise generation system including a custom amplifier and speaker is used to create a broadband acoustic field aimed towards the microphone being tested which is mounted on a soft piece of

foam to minimize vibration coupling through the wire mesh chamber floor. The microphone output is fed into a dynamic signal analyzer where the amplitude spectrum is computed, time averaged for accuracy, and recorded. The noise source is not perfectly white but instead contains several peaks and troughs up to 10dB in magnitude throughout the 100Hz-10kHz range. Accurate measurement of acoustic response therefore requires normalization to a calibrated broadband measurement microphone with a known flat response. Two such microphones are used for this purpose – a ¼ inch GRAS microphone and a ½ inch Larson Davis model 2541 microphone.

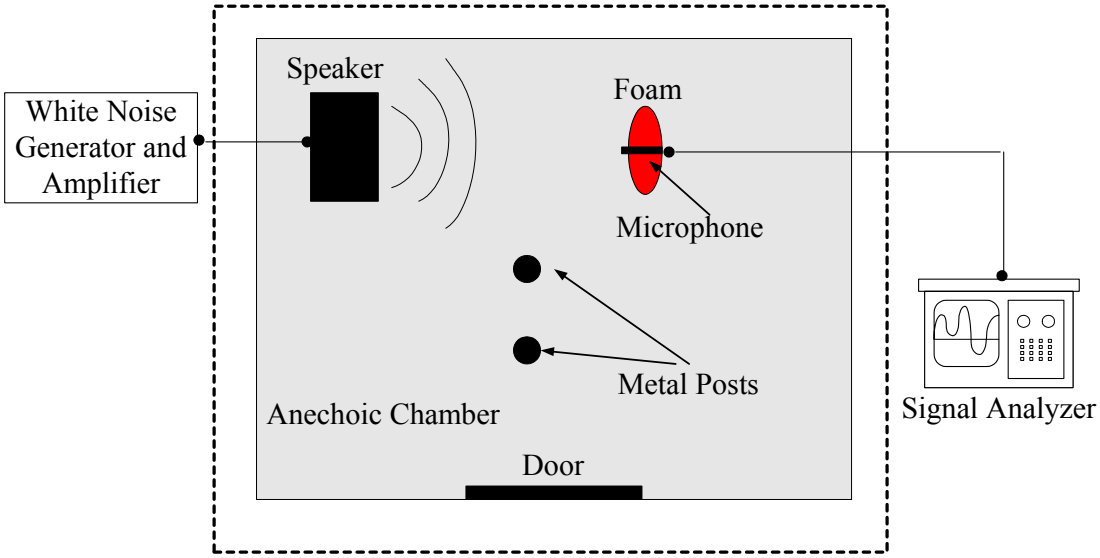

Figure 50 Experimental arrangement for acoustic response testing

In a first series of measurements, the spectra of all three microphones (i.e. optical microphone, GRAS, and Larson Davis) are recorded separately with the configuration shown in Figure 50. Testing with only a single microphone present at a time provides the best approximation to the free-field condition. To demonstrate the legitimacy of the measurement approach and normalization procedure, the recorded spectra of the Larson

Davis and GRAS microphones are normalized with respect to each other to obtain the response labeled Experiment 1 in Figure 51. The flat response shows that the normalization procedure sufficiently accounts for the complexities of the source shape, and also shows that the mounting conditions sufficiently reduce any vibration coupling that could potentially corrupt the measurement. To asses the potential effects of acoustic scattering caused by the relatively large optical microphone test-bed, the spectrum of the Larson Davis measurement microphone is recorded in a second type of experiment where all three microphones are set in close proximity on the mounting foam together. This spectrum is normalized to the Larson Davis spectrum as recorded in experiment 1, which is the accurate spectrum of the free field pressure. This normalized response, labeled as Experiment 2 in Figure 51, shows peaks and troughs as large as 10dB in magnitude at frequencies above 1kHz. Since the vibration mounting conditions are unchanged, it is clear that these complications are related to acoustic scattering caused by the presence of the optical microphone test-bed. These results show that a flat response should be expected only when free-field conditions are strictly adhered to.

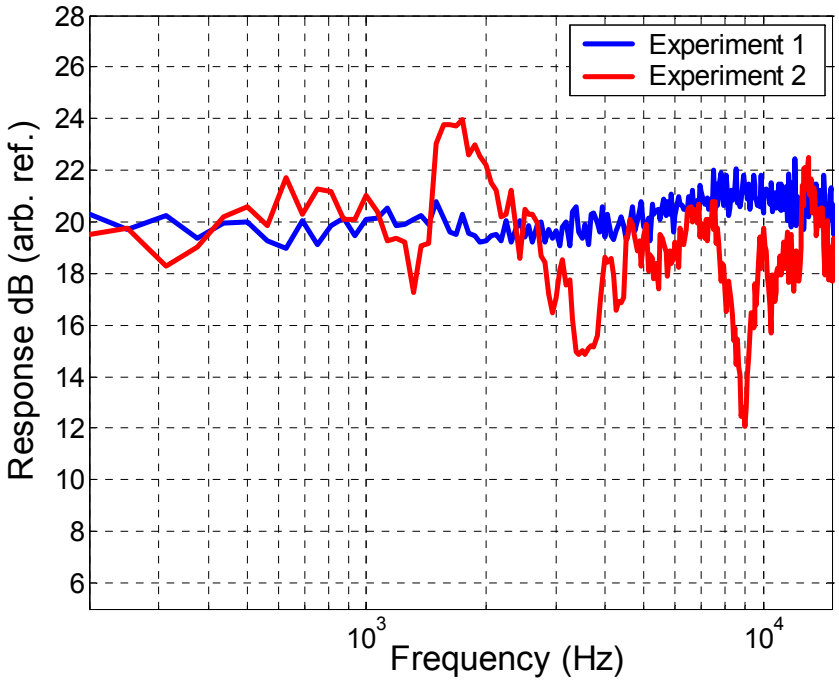

Figure 51 Normalized response of two calibrated measurement microphones for two different experimental conditions.

The free-field response of the optical microphone can be determined by normalizing its measured spectrum with either of the calibration microphones' spectrum as measured with the first type of experiment described above which best approximates the free field condition. The result, shown as Response 1 in Figure 52, is nominally flat at frequencies below 2kHz implying that the microphone package is effectively sealed. Above 2kHz, the response shows a steady increase that is most likely due to the form factor presented by the test-bed. The overall decay in response in the 6kHz to 15kHz range is expected due to the squeeze film damping in the microphone air gap as was also observed in the electrostatic characterization. In addition to these properties, there are several peaks and troughs in the response throughout the 3kHz-15kH range, for example those occurring at 4kHz, 8kHz, and 9kHz. These are most likely a result of vibration

induced by the mounting of the front end microphone package depicted in Figure 22 to the hand-held test-bed. This vibration is not coupled from the mounting of the test-bed to the surrounding structure, but rather it is induced by the bombardment of the test package with the acoustic signal itself. This is evidenced by the fact that the response shown in Figure 52 is obtained regardless of the test-bed mounting conditions. The same result is obtained in additional experiments with the set-up mounted on a steel post and hanging from the chamber ceiling which effectively eliminates all vibration coupling from the surrounding structure.

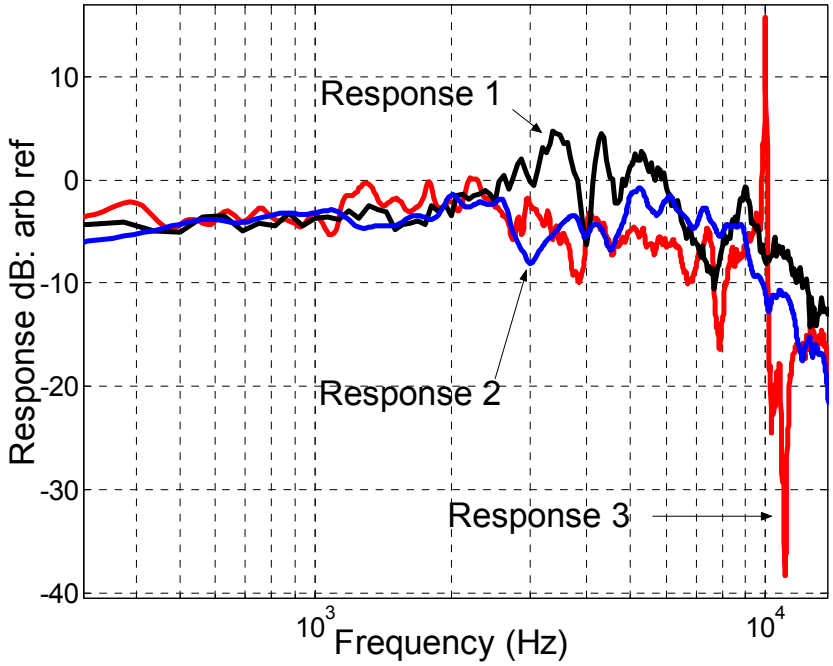

Figure 52 Normalized response of the optical microphone with different packaging conditions.

The source of the vibration is most likely the cascade of spring loaded spacers used to adjust the tilt of the front-end microphone package which is required for alignment of the diffracted orders onto the photodiode array. These spacers are shown

and labeled in Figure 32 which is a photograph of the test apparatus. If this is the case, the measured response should show dependence on the number of screws and spacers used and also the degree to which the screws are tightened. This has been demonstrated with measurements made on different occasions after the microphone package has been detached and reattached to the setup. Figure 52 shows two additional normalized responses, labeled Response 2 and Response 3, measured under different conditions. The location and magnitude of the fluctuations in the response are different for each case. Future designs should incorporate a different attachment method for the prototype package to eliminate this packaging dependant variability induced by vibration.

The dB reference for the plots in Figure 51 and Figure 52 has been arbitrarily chosen since the shape of the response is the primary characteristic under investigation. At low frequencies where the response is flat and resembles the electrostatic actuation response, it is known the mechanical response of the microphone diaphragm is 44Å/Pa as has been determined with the characterization work presented earlier in this chapter. It should be noted that the response sensitivity of capacitive microphones is typically expressed in units of V/Pa as opposed to Å of diaphragm displacement. This same measure is readily computed for the optical microphone as the product of the membrane compliance and the displacement sensitivity. From the displacement sensitivity plot in Figure 40, a total sensitivity of 30V/μm can be achieved with differential detection at a gap height of 1.76μm. Recall that this value is obtained by summing each order's individual displacement sensitivity. With a diaphragm compliance of 44Å/Pa, the sensitivity is 132mV/Pa. This figure alone, however, does not provide a meaningful comparison since this value can be made much larger or smaller by simply adjusting the

voltage gain of the transimpedance amplifiers. A meaningful comparison can only be made when noise is considered. This is the subject of the next chapter.

CHAPTER 6

OPTICAL MICROPHONE PERFORMANCE

For many if not most applications, the most important measure of microphone performance is the pressure detection resolution, which is limited by the pressure equivalent noise signal generated by the internal noise of the device. This level is typically quoted in dB over a certain bandwidth, or simply in dBA for acoustic transducers designed to perform in the audio frequency range. Acoustic signals cannot be measured below this level as they cannot be distinguished from the noise itself. This chapter presents the measurements performed to asses the internal noise level of the diffraction based optical microphones. These measurements show a displacement resolution of 6×10^{-4}Å/√Hz at 1kHz which is limited by thermal acoustic noise caused by the back-plate resistance. The resulting A weighted sound pressure level of the optical microphone is 39.9dBA, which is adversely affected by the limited bandwidth of the microphone which shows a 3dB upper cutoff frequency of 2kHz. The dominant noise sources across the entire frequency range are characterized and recommendations are made for future designs.

Displacement Resolution

The displacement resolution of the sensor is obtained as the measured rms output noise amplitude in volts divided by the calibrated displacement sensitivity measured in Chapter 5. A displacement signal with the resulting rms amplitude would have a signal to noise ration of 1, and is therefore the minimum detectable displacement (MDD) of the

sensor. The noise voltage can be expressed in terms of its amplitude spectral density which allows the displacement resolution to be expressed in Å/√Hz as a function of frequency. In general, this noise voltage can be dominated by the major internal sources – PD shot noise, laser noise, and thermal acoustic noise – or it can be dominated by external ambient acoustic and vibration noise. In order to eliminate these ambient sources and measure the internal noise of the microphone, the device is tested in the anechoic acoustic test chamber.

As measurements in this chapter illustrate, the noise level measured by the optical microphone becomes limited by the acoustic chamber noise at low frequencies. Therefore, while it is not the intent of this work to completely characterize all the variables affecting the acoustic noise floor of the anechoic chamber, efforts were taken to lower this floor as much as possible. The most important variable affecting the measurement is the mounting of the microphone inside the chamber. This is illustrated with several measurements made using a ½ inch Larson Davis model 2541 microphone. This microphone is accurately calibrated with the use of a custom hand-held signal generator that completely encompasses the microphone cartridge while applying a 114dB pressure signal at 250Hz. Figure 53 shows the recorded noise spectrums with the microphone mounted in three different configurations as measured with a Stanford Research Systems (SRS) SR785 dynamic signal analyzer. In the first case, the microphone is secured to a steel post which anchors to the building floor. In a second configuration, the microphone is mounted on a piece of soft foam directly on the wire mesh floor of the chamber. The lower noise floor measured with the use of the soft foam suggests that the noise is dominated by vibration rather than airborne acoustic noise.

This is made clear in the next measurement shown in Figure 53, where an even lower noise floor is measured with the microphone hanging in the center of the chamber to effectively isolate it from any vibration of the surrounding structure. A final improvement in the noise floor was made by shutting down the HVAC system which generates noise in the immediate vicinity outside of the chamber. The last measurement shown in Figure 53 is performed using a "shorting" cartridge fastened to the microphone preamplifier which presents the same capacitance as the actual microphone head but is clamped and therefore does not respond to sound or vibration. This measurement allows the internal electronic noise of the microphone to be measured which, as expected, is significantly below the acoustic noise in the chamber.

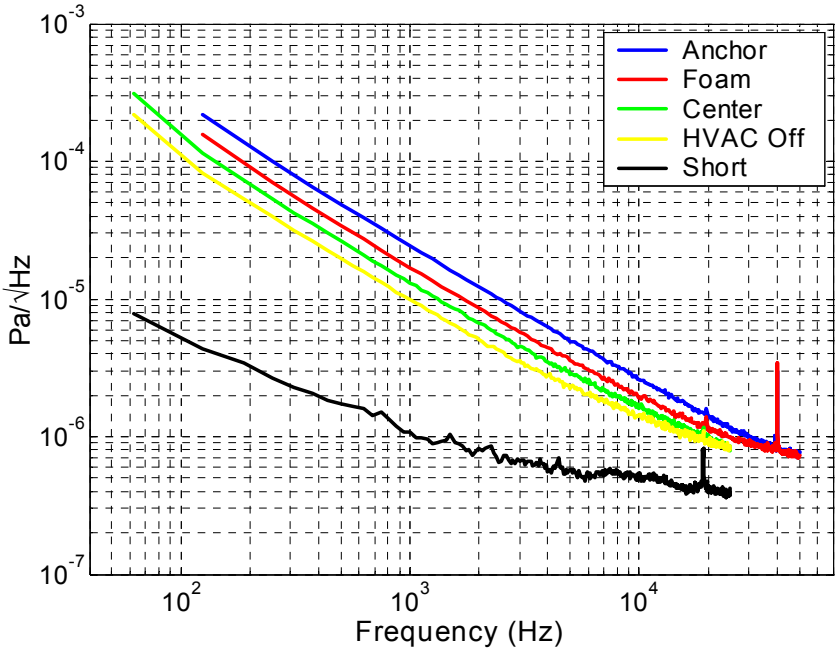

Figure 53 Noise spectrum measured in the anechoic chamber for various mounting conditions

The corresponding A weighted noise levels for these measurements are shown in Table 2. The minimum acoustic noise floor obtainable under these conditions is

28.8dBA, which is adequate for measuring the internal noise of the optical microphone. It should be noted that the values presented in the table, as measured with the signal analyzer, are within 1.5 dBA of measurements performed using a hand-held Larson Davis model 824 sound level meter.

Table 2 A weighted noise levels of the noise spectrums shown in Figure 53

Steel	36.7 dBA
Foam	33.9 dBA
Center	31.3 dBA
HVAC Off	28.8 dBA
Short	10.9 dBA

The optical microphone on the hand-held test bed is suspended in close vicinity to the Larson Davis microphone inside the anechoic chamber as the noise voltage spectrum at the amplifier output is recorded for several different membrane – back-plate gap heights, which is controlled via application of the applied DC bias level. Two independent calibration procedures can be used to convert the voltage output to the equivalent diaphragm displacement. The most direct method is to simply divide the output voltage by the calibrated displacement sensitivity as measured with the external profilometer and summarized in Figure 40 of Chapter 5. For example, at the optimal bias point, the sensitivity of the zero and first order are 10V/μm and 20V/μm, respectively, and 30V/μm when differential detection is used. Alternatively, a speaker can be placed inside the anechoic chamber to generate a known pressure as measured by the calibrated Larson Davis microphone. Since the mechanical compliance of the optical microphone membrane has been characterized in Chapter 5, this acoustic pressure applies a known reference displacement to the microphone diaphragm. The method has been applied here

to measure displacement sensitivity with units of V/μm within 15% of the values measured in Figure 40.

The recorded noise spectrums with the applied displacement signal at 1kHz are shown in Figure 54. The measurement labeled chamber is simply the ambient acoustic noise as measured by the Larson Davis microphone multiplied by the membrane compliance of the optical microphone. In other words, this would be the displacement spectrum of the optical microphone if limited by the ambient acoustic noise in the chamber. To determine the noise level of the sensor in the absence of all ambient acoustic and vibration noise and also internal thermal noise, the spectrum is first recorded with the microphone diaphragm held rigidly collapsed to the back-plate. This measurement is in perfect analogy with the shorting cap measurement performed using the Larson Davis microphone as it represents the minimum noise level obtainable for the particular laser diode, laser power, and displacement sensitivity of the device. In these experiments, a 5mW laser diode is used with 1.8mW captured in the zero order and 0.6mW captured in a single first order which are together used for the displacement detection. To illustrate the benefits of using differential diffraction order detection for both increased displacement sensitivity and reduced laser intensity noise, the measurement is performed using the first order only and also using the difference of the zero and first orders. As can be observed in Figure 54, the shot noise limit is approached at high frequencies where differential order detection provides a 14dB improvement over single order detection. Since the increase in displacement sensitivity resulting from differential detection is only 3.5dB as shown in Figure 40, it is clear that differential detection plays an important role in reducing the laser intensity noise.

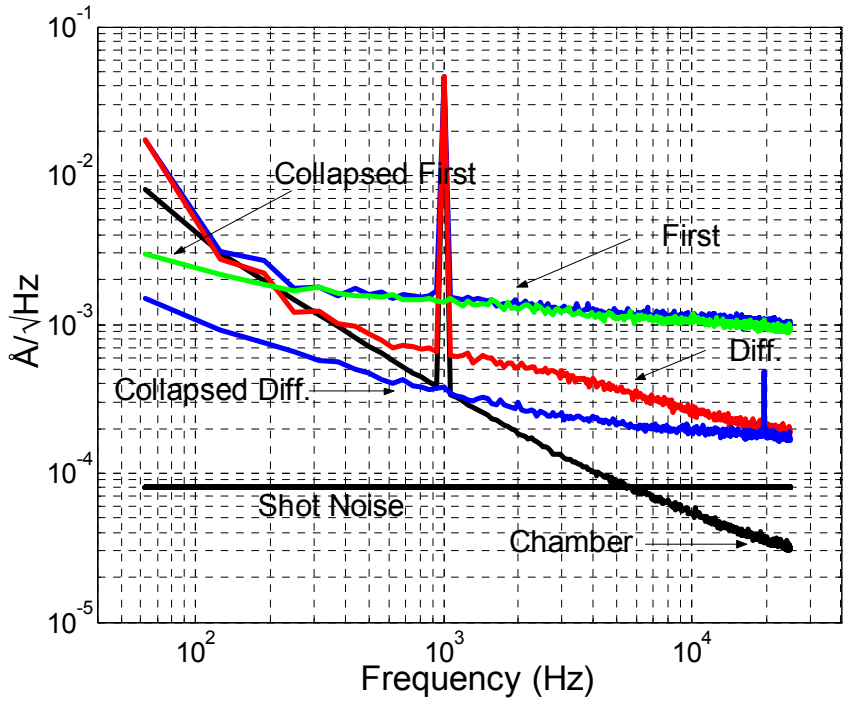

Figure 54 Displacement noise spectrum of the 2100μm diaphragm

The diaphragm is then released from collapse and biased to a gap height of optimal displacement sensitivity where the noise spectrum is again recorded with and without differential detection. When the first order alone is measured, the noise is dominated by the ambient acoustic noise at frequencies below 200Hz where the spectrum is observed to match the chamber spectrum but then becomes dominated by the laser intensity noise at higher frequencies where the spectrum is identical to the first order collapsed measurement. With differential detection, however, the displacement detection is able to remain chamber noise dominated up to 600Hz before the presence of an internal noise source dominates in the 600Hz-10kHz range. This internal noise is different from the fundamental limit as determined by the collapsed measurement in both scale and

frequency dependence. The following analysis shows that this is thermal acoustic noise caused by the large back-plate flow resistance.

The parameters in the equivalent circuit model presented in Chapter 4 have been completely characterized with the experiments summarized in Chapter 5. The diaphragm properties have been determined with dynamic measurements made in vacuum, and the back-plate flow resistance can be adjusted so that the model accurately fits with the measured response data in air. For example, for the simulation using a back-plate resistance of 1×10^{10}Pa×sec/m^3 in Figure 31, the response closely resembles the measured response data presented in Chapter 5. With the parameters determined, the same equivalent circuit can be used for a thermal acoustic noise analysis of the sensor by placing pressure sources in series with each resistive element as is shown in Figure 55. The effective thermal agitation pressure, P_n, from each acoustic resistance, R, has a flat distribution in frequency and can be computed with units of Pa/√Hz as

$$P_n = \sqrt{4kTR} \tag{40}$$

where k is Boltzman's constant and T is the ambient temperature[42, 43].

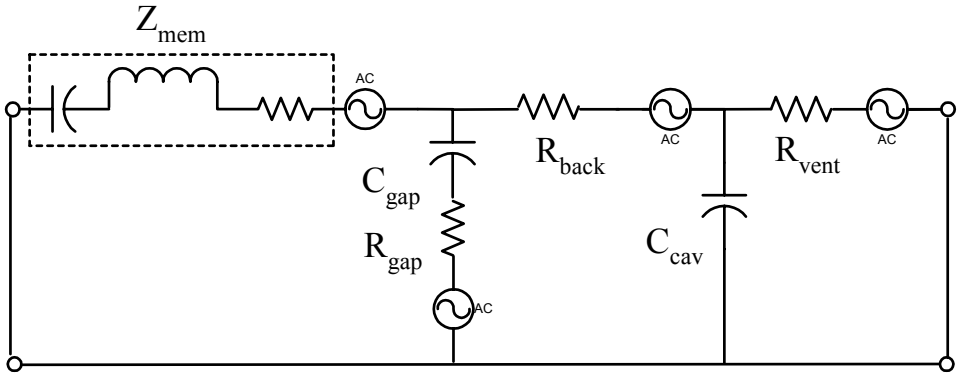

Figure 55 Thermal noise circuit for the optical microphone

The back-plate resistance is an order of magnitude larger than any other resistance in the circuit, and the thermal agitation pressure generated by its presence can be computed using Equation 40 as 1.1×10^{-5}Pa/√Hz. Since the gap impedance is large relative to the membrane and since the cavity impedance is small, this pressure is essentially applied across the membrane impedance and the back-plate resistance in series which gives rise to a frequency dependence observed in the noise spectrum of Figure 54. Results from a complete simulation of the circuit are presented in Figure 56 against the measured spectrum from Figure 54.

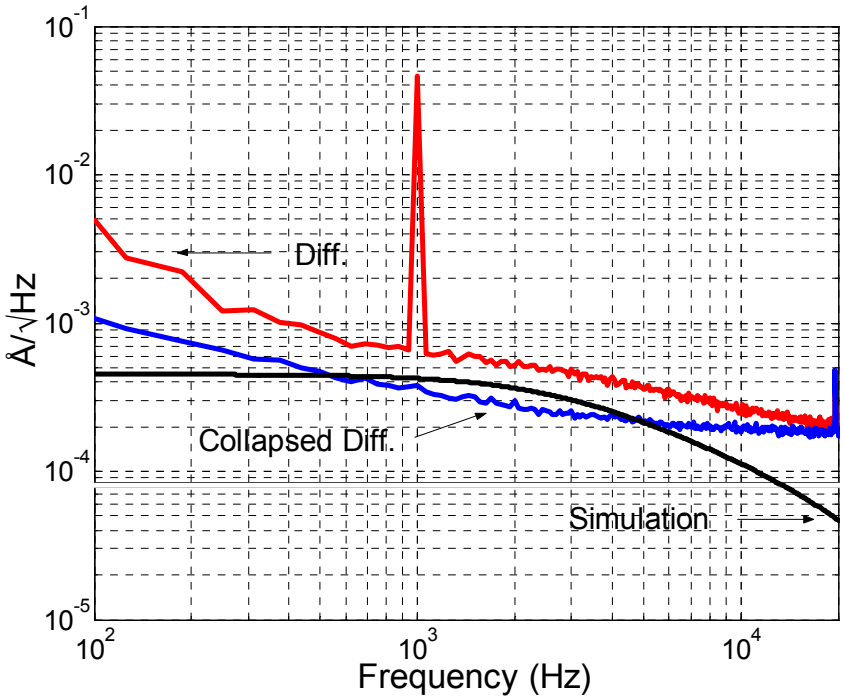

Figure 56 Simulated thermal noise plotted against the measured noise spectrum

The simulated thermal noise is similar in shape to the observed noise spectrum but slightly less in amplitude. The observed noise, however, is expected to consist of the incoherent addition of the thermal noise and the uncancled laser intensity noise

represented by the collapsed measurement in Figure 56. This total simulated noise is plotted in Figure 57 against the measured spectrum. The similarity in both scale and frequency dependence confirm that the thermal noise is indeed the dominant noise source over the 600Hz-10kHz range

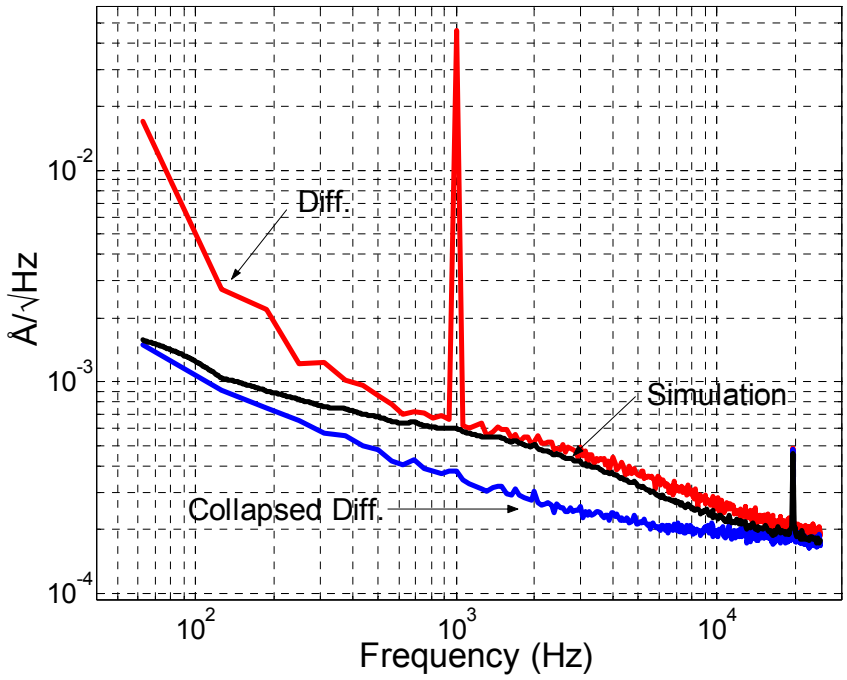

Figure 57 Total simulated noise plotted against the measured noise spectrum

An additional note regarding the measured noise spectrum in the frequency range below 600Hz is required. As mentioned above and illustrated in Figure 54, the noise level of the sensor in this range is approximately equal to the ambient chamber noise. However, the spectrums from the optical microphone for both the first order and differential order detection show small spikes at frequencies of roughly 125Hz and 250Hz which are not seen in the smooth curve measured by the Larson Davis microphone. Furthermore, these spikes are not seen in optical microphone spectrum

when the diaphragm is completely collapsed, which suggests that there is some additional noise source physically displacing the diaphragm. A measurement of the noise voltage spectrum from the DC Power supply used to bias the diaphragm shows that small oscillations in the DC bias voltage which act to actuate the diaphragm are causing this low frequency noise. The measured voltage spectrum is scaled by *dP/dV* which is obtained from Figure 43 to compute the actuation pressure, and this pressure is in turn scaled by the diaphragm compliance to obtain the equivalent diaphragm displacement plotted in Figure 58. The agreement between the magnitude and the frequency dependence of this noise source suggest that this is indeed responsible for the narrowband spikes at low frequencies.

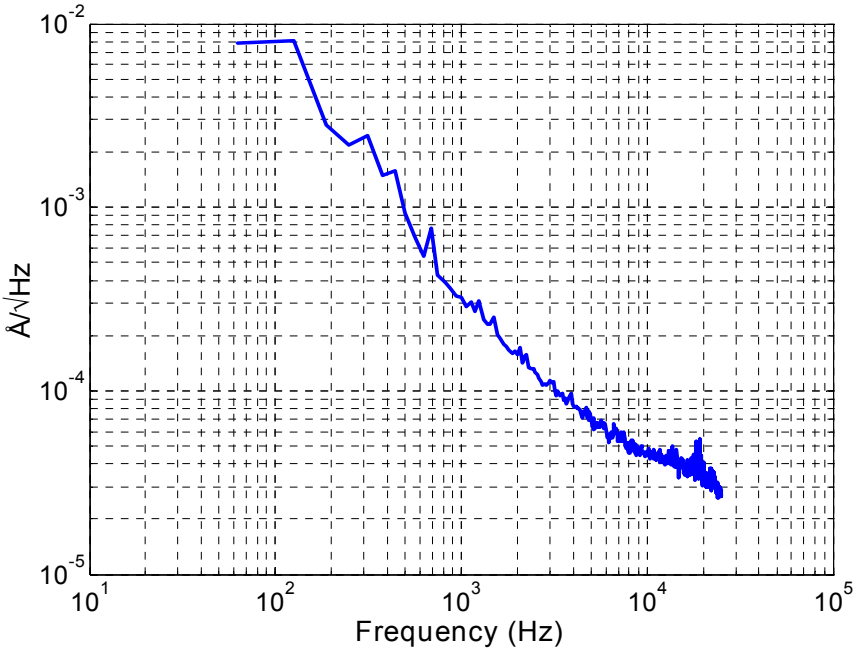

Figure 58 Displacement noise spectrum resulting from the DC bias source

In future designs with integrated actuation electronics, this noise voltage should be reduced below the desired level.

Sound Pressure Resolution

The sound pressure resolution of the optical microphone analyzed in the previous section is obtained by dividing the noise spectrum presented in Figure 54 by the dynamic response of the of the microphone structure in Å/Pa which is characterized in detail in Chapter 5. The microphone will only have good pressure resolution at frequencies where the sensitivity is high. Above the upper cut-off frequency of the microphone where the mechanical sensitivity is small, fluctuations in output voltage will correspond to large equivalent pressures.

The optical microphones designed and characterized in this work have poorly designed back-plates which limit the effective bandwidth to frequencies well below the diaphragm resonance of 40kHz. As can be observed in Figure 49, the 3dB cut-off frequency for the 2100μm structure is between 2-4kHz depending on the particular gap height being used. The resulting pressure resolution of the optical microphone computed with this response is shown in Figure 59. Although such a microphone would most likely not have meaningful application for audio applications due to the frequency response, an A weighted noise level of 39.9dBA can be computed to serve as an overall figure of merit.

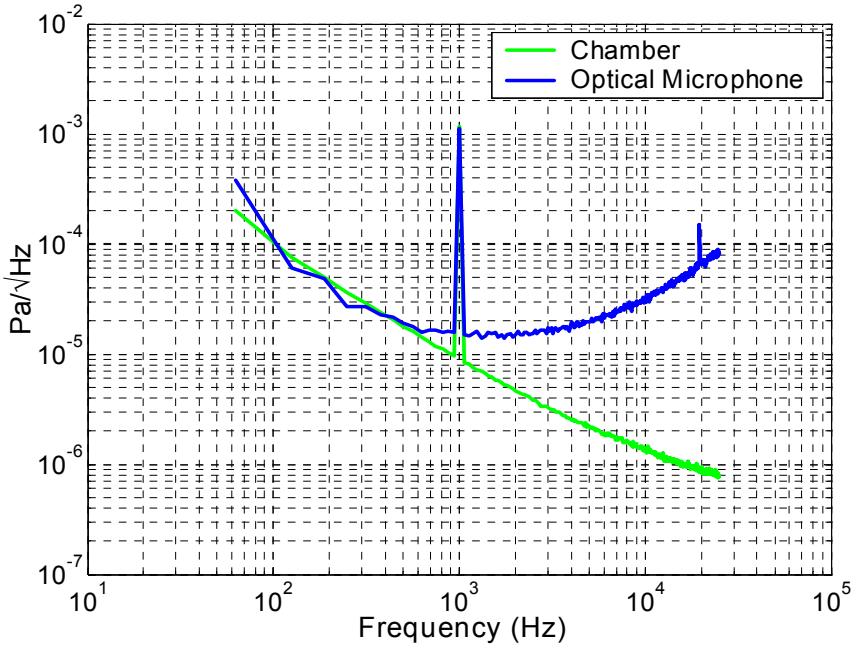

Figure 59 Noise spectrum of the optical microphone normalized to equivalent sound pressure

The microphone performance can benefit greatly from an improved back-plate design with a lower effective flow resistance. For example, the simulations in Figure 31 show that a back-plate resistance of 1×10^{8} Pa×sec/m^{3} would be ideal as this would effectively dampen the diaphragm resonance without sacrificing bandwidth. The equivalent thermal agitation pressure for this resistance as computed using Equation 40 is 1μPa/√Hz which results in 4×10^{-5}Å/√Hz of diaphragm displacement for the 2100μm diaphragm currently under consideration. This value is below even the shot noise limit as shown in Figure 54. Therefore, with this design the displacement noise spectrum is expected to be identical to the data measured with the collapsed diaphragm. Improving the back-plate design therefore both – 1) increases the microphone bandwidth and 2) lowers the internal noise across the 1kHz – 10kHz frequency range.

The corresponding A weighted rms displacement amplitude for the collapsed measurement is 2.4×10^{-2}Å. With the 44Å/Pa membrane currently in use, the resulting A weighted noise level can be computed as 29.0dBA which is close to the chamber noise floor. Furthermore, if a diaphragm with a 20kHz resonance is used the mechanical compliance is expected to increase by a factor of 4 to roughly 160Å/Pa. The A weighted noise level for such a diaphragm would be 17.5dBA. The back-plate resistances and diaphragm sensitivities described here are commonly found in the literature for both traditional sized microphones and silicon microphones [44, 45]. For example, Pederson et al. have fabricated 1.6mm and 2.1mm microphones with a flat response up to 18kHz using a process with a sacrificial air gap of only 1.5µm [46].

The possibility of improving the back-plate design can also be demonstrated to an extent with one of the 900µm Sandia devices currently available. This device, depicted in Figure 15 and Figure 17 of Chapter 3, has 160µm×160µm back-plate perforation holes as compared to the 2100µm device which has 80µm×80µm holes. Dynamic characterization of this 900µm device was also tested with the procedure outlined in Chapter 5 to obtain the response presented in Figure 60. The sensitivity units for this plot are not well known since this device did not undergo a detailed displacement sensitivity characterization. It is clear, however, that the 3dB cutoff frequency is approximately 15kHz which is a substantial improvement.

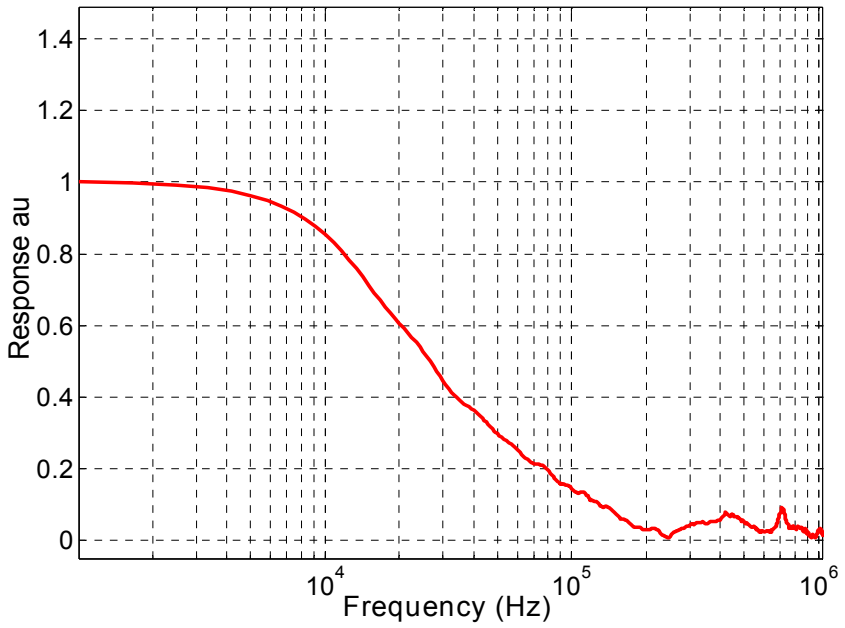

Figure 60 Electrostatic Response of a 900µm Sandia membrane in air

Sensitivity to Acceleration and Temperature

Although the dominant noise sources for the optical microphone have been completely diagnosed and characterized for the tests in the chamber, there are, in general, several other external noise inputs to consider. All microphones will have a certain sensitivity to acceleration. The particular packaging of the microphone can affect this sensitivity by determining how much acceleration applied to the package is actually transferred to the diaphragm anchors and also by determining how much air in the packaging channels is entrained with the motion of the microphone diagram. The later can effectively add significant mass which makes the device more sensitive to acceleration. A packaging independent calculation can, however, readily be applied to any microphone diaphragm to estimate the sensitivity so long as the fundamental

diaphragm resonance frequency is known. This calculation ignores any added acoustical mass and is based on a simple one degree of freedom oscillator. At frequencies away from resonance, the equivalent pressure applied to the diaphragm as a result of its acceleration is simply the acceleration multiplied by the diaphragm mass. The resulting diaphragm displacement, *d*, normalized to the acceleration input, *a*, is then

$$\frac{d}{a} = \frac{M}{K} = \frac{1}{\omega_{fund}^2} \tag{41}$$

where M and K are the membrane mass and stiffness, respectively, and ω_{fund} is the fundamental diaphragm resonance frequency. The literature for calibration measurement microphones such as the Larson Davis used in the anechoic chamber measurements expresses the acceleration sensitivity in terms of equivalent pressure in dB resulting from a 1m/sec^2 input [47]. The Larson Davis microphone which has a diaphragm resonance of 14kHz, for example, is quoted to have 62dB acceleration sensitivity. For the optical microphone, the high diaphragm resonance of 40kHz results in a lower sensitivity of 44dB.

A second type of actuation input which is particularly important to consider for micromachined sensors is thermal actuation. Structures will typically deform under heating and cooling due to thermal expansion. For traditional sized microphone components, thermal masses are such that disturbances in equilibrium temperature usually occur at frequencies below the desired measurement range. However, with MEMS devices, thermal masses are small enough to enable mechanical actuation into the kHz range via the application of a modulated heat source. Indeed, this has been shown to be a useful actuation technique for some devices [48]. For the optical microphone designs presented in this thesis, however, thermal actuation is not a major concern due to

the clamped boundary conditions enforced along the perimeter and the high residual tension in the nitride membrane. The finite element model presented in Chapter 4 was used to asses the displacement resulting from a temperature change and it was discovered that the primary displacement mechanism is Poisson stretching of the nitride membrane. An increase of 1 degree Celsius adds approximately 6MPa of tension to the nitride. The resulting thinning of the membrane is 0.1Å which corresponds to an equivalent pressure level of 42dB. An additional adverse effect of the change in tension is an accompanying change in mechanical sensitivity of the diaphragm. Since the stiffness of the diaphragm is primarily determined the tension, the sensitivity can change markedly over larger temperature changes. It should be noted, however, that the relationship between temperature change and change in diaphragm tension has not been studied over large ranges.

The remaining sections of this work present two other applications of the optical detection method – optical cMUTs and surface micromachined microphones.

CHAPTER 7

OPTICAL CAPACITIVE MICROMACHINED ULTRASONIC TRANSDUCERS

The diffraction based optical displacement method is also applied to cMUTs fabricated using aluminum membranes with diffraction grating bottom electrodes on quartz substrates. The receive sensitivity and dynamic range of these devices are characterized and compared against cMUTs with capacitive detection. The large displacement sensitivity of the optical method enables the demonstration of a 4mm×4mm phased imaging array. An experiment showing the imaging of two thin wires is presented in the final section of the chapter.

Fabrication of Optical CMUTs

To demonstrate the detection method, individual aluminum membranes and membrane arrays were fabricated on standard 0.5mm thick fused quartz substrates as shown in Figure 61. First, 0.2μm thick aluminum diffraction fingers were formed using e-beam evaporation and a standard lift-off procedure. A 50nm layer of chromium was used to promote good adhesion between the aluminum fingers and the quartz surface, and a 0.3μm thick layer of plasma enhanced chemical vapor deposition (PECVD) oxide was deposited over the completed fingers for electrical isolation. Second, positive photoresist was patterned in the shape of circular membranes to form a sacrificial layer for the membrane fabrication. The thickness of the resist determines the gap height of the completed structure and was 2 to 2.8μm in this case.

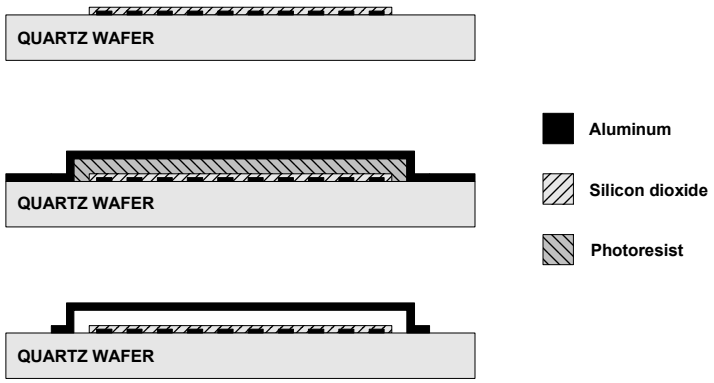

Figure 61 Fabrication schematic for CMUTs with optical diffraction gratings

One and two-dimensional arrays with 100, 160, and 200μm diameter membranes were patterned. Finally, 1μm thick aluminum membranes were sputtered and patterned, and the sacrificial layer was removed using acetone. An extended stem of the sacrificial photoresist is used to protect the bottom electrode during the sputtering and forms the etch channel which remains open to the atmosphere. These details are made clear in Figure 62 which shows a scanning electron micrograph (SEM) of a completed 2-D array of 100μm diameter membranes and a micrograph of the back-side of an individual cMUT element.

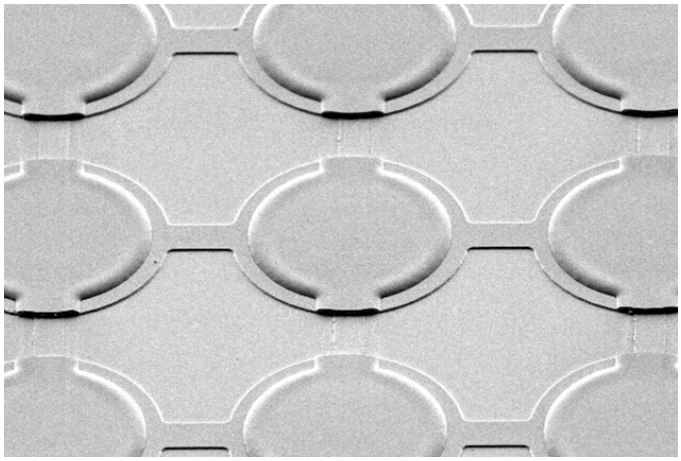

(a)

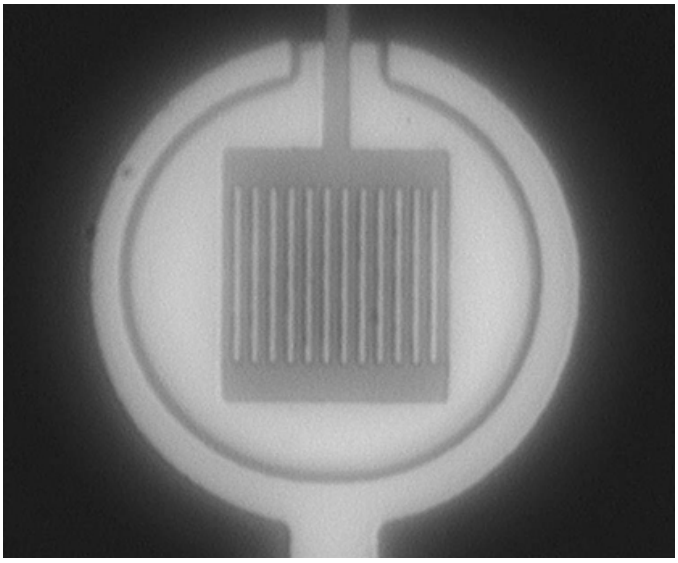

(b)

Figure 62 (a) SEM of a section of a cMUT with 100μm diameter membranes and (b) micrograph of the back-side of an isolated 100μm cMUT element

Note that since the substrate is transparent, the details of the bottom electrode can be seen, which in this case consists of a diffraction grating with 4μm period. As is the case with most new microfabrication processes, multiple iterations had to be performed before a successful recipe was developed.

Experimental Characterization

Several different bench top set-ups on optical breadboards have been used to experimentally test the detection scheme. The one which has proven the most convenient to work with is a compact hand-held set-up very similar to the one used for the optical microphones and shown in Figure 32. In this case, the light from a laser diode is focused to illuminate a single membrane in the cMUT.

Receive Mode

To verify electrostatic actuation capabilities, a DC bias voltage is applied to a 160μm membrane while the output of the first order photodetector amplifier is recorded. The collected data is plotted in Figure 63(a) where a full cycle of the intensity versus gap thickness curve is traced for both increasing and decreasing bias voltage.

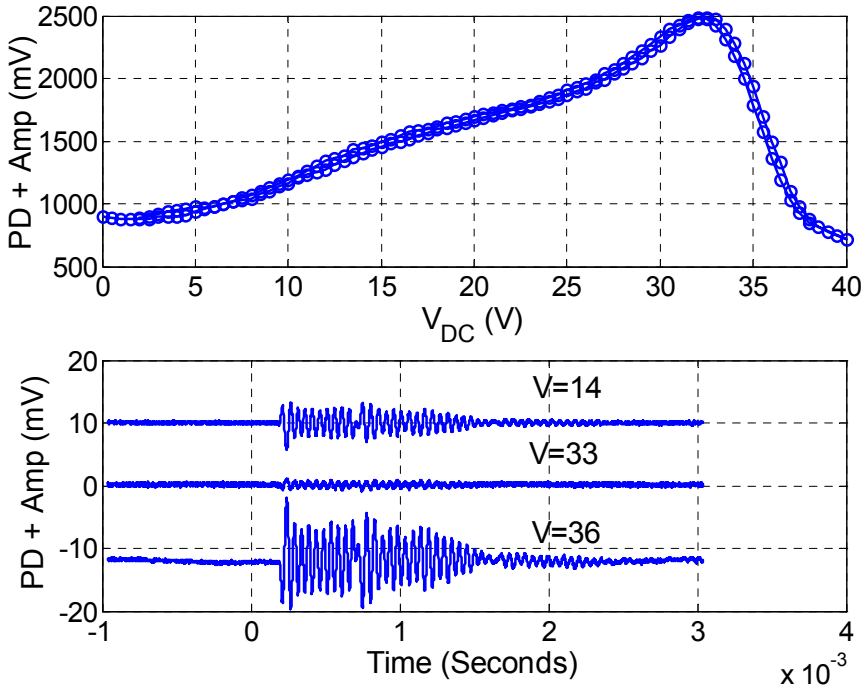

Figure 63 Diffraction order intensity versus actuation voltage (top) and sound received ultrasound at three bias voltages (bottom)

To demonstrate sound detection capability and the effect of DC bias on optical detection sensitivity, the membrane is subjected to an external acoustic signal at 20kHz. A speaker is driven by a 10-cycle tone burst generating a measured pressure of ~1Pa in air at the membrane surface while the DC bias of the cMUT is varied. The optical output signal measured at 3 different bias voltages are plotted in the bottom portion of Figure 63. Note from the top figure that a bias voltage of 33V produces a membrane deflection that corresponds to a peak in the intensity vs. gap thickness curve, where the sensitivity to small displacements is expected to be small and nonlinear. Indeed, the poor sound recording at this bias level shows this to be the case. A bias level of 36V, however, corresponds to a point of maximum slope and the sound measurement shows the enhanced detection sensitivity as expected. Also note that at the DC bias of 14V, the

optical intensity is biased to the same level as at 36V, but the received signal is much weaker. This is due to the stronger electrostatic softening effect at higher bias voltages where the mechanical stiffness of the membrane is reduced due to the non-linear nature of the electrostatic force [49, 50].

Since the displacement sensitivity of the optical detection method does not depend on the acoustic frequency, the bandwidth of the method is limited by the photodetectors and detection electronics, which can extend from DC to GHz frequencies [51, 52]. Improved sensitivity at low frequencies is especially important for ultrasound applications in air. Furthermore, the sensitivity does not depend on the device capacitance, which eliminates the problems associated with parasitic capacitance especially for small array elements. These features of the optical detection method are demonstrated in Figure 64, where the vibration amplitude of a single cMUT membrane is measured by recording the photodetector output while sweeping the frequency of electrostatic actuation in the 1kHz-1MHz range. In this particular case, the cMUT membrane is 1μm thick and has a 180μm diameter. Since this is an unsealed device, the air in the membrane-substrate gap plays a significant role in the frequency response of the cMUT. Below a cut-off frequency of 10kHz, the air can move in and out of the membrane-substrate gap and the membrane stiffness dominates the dynamic behavior. After the cut-off frequency the air gets trapped in the cavity and starts acting like an additional spring. This results in a lower displacement and a resonance frequency that is higher than predicted assuming a membrane in vacuum [11, 53].

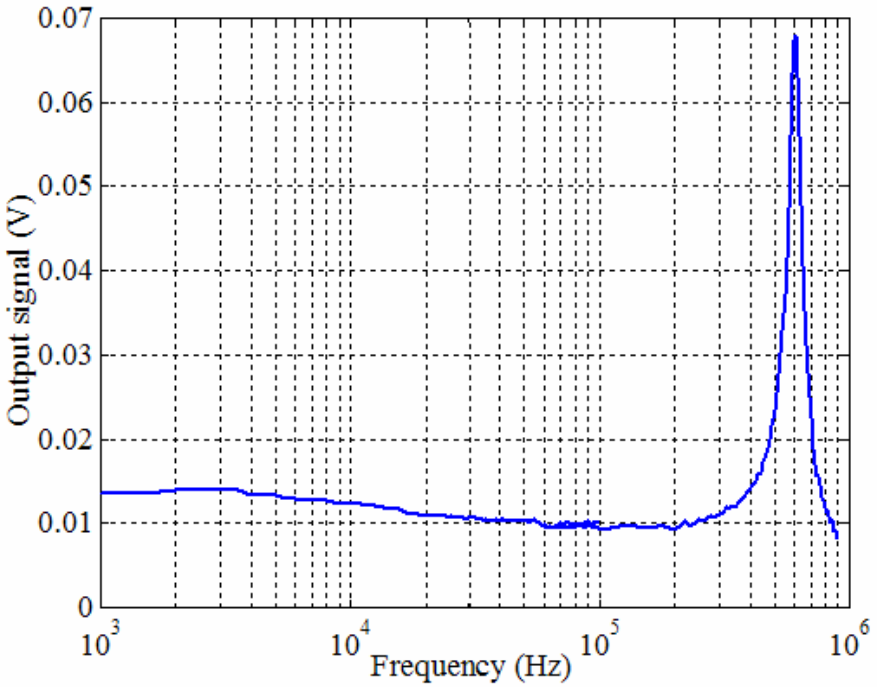

Figure 64 Dynamic response of the cMUT measured with electrostatic excitation

In these experiments, the minimum detectable displacement for the set-up is measured to be $2\text{x}10^{-4}$Å/√Hz around 250kHz using electrostatic forces to generate known displacements and measuring the rms noise over a known bandwidth [54]. Assuming that the membrane displacement can be on the order of 1µm during transmit, this particular cMUT with optical detection will have 154dB/√Hz effective dynamic range (104dB with 100kHz bandwidth). This figure, obtained by using a single membrane for optical detection is comparable to the best results obtained with a large (1cmx1cm) conventional cMUT operating at 2.3MHz with approximately 12000 membranes [55]. Therefore, cMUTs with optical detection are ideal for many nondestructive evaluation (NDE) applications in air in the 100kHz-1MHz range.

One can also compare the detection sensitivity of the optical method with other cMUT detection schemes. Since the RF detection method (Equation 2) cannot be used with a single membrane, a cMUT with 10 membranes with 180μm diameter and 2μm gap (d_0) is assumed. Ignoring parasitic capacitance, conventional detection (Equation 1) results in 0.357μA/nm sensitivity at 100V DC bias and an ultrasound frequency of 250kHz. The RF detection scheme would provide 14.1μA/nm sensitivity with 1GHz RF frequency, 4V RF signal amplitude, again ignoring any parasitic capacitance. Furthermore, neglecting any other electrical losses, the RF method would consume approximately 160mW to achieve this sensitivity. On the other hand, the optical method generates 16μA/nm sensitivity using a single membrane and a 2mW laser with 632nm wavelength. Note that the optical method is not affected by parasitic capacitance and gap thickness. Therefore, for typical ultrasound applications in air, the optical method provides high sensitivity, large dynamic range with simple electronics and low power consumption as compared to other cMUT detection methods [56].

Ultrasonic Imaging in Air

Ultrasonic imaging in air has many applications from robotics to metrology. Most imaging systems in air either use a phased array approach with a small number of large elements or a fixed focus system to improve spatial resolution [57-59]. CMUT arrays with capacitive detection can be used for improved array imaging, but it either requires large elements to have enough sensitivity or complicated electrical interconnects due to low capacitance of small array elements [40]. Optical detection avoids this problem because one can probe a single individual membrane in a cMUT without loss of

sensitivity. For example, to implement a 1-D imaging array, one does not need to interrogate all the membranes in each cMUT array element, which can be more than 1000 [50]. It is sufficient to illuminate only several membranes of each array element with a VCSEL or another laser and utilize the rest of the area for photodetectors and amplifiers.

This capability is demonstrated using a cMUT consisting of a 19×19 array of 160μm diameter membranes with 225μm pitch connected in parallel as shown in Figure 65. With 80V DC bias, the transducer has a resonance at 750kHz. During transmission, all membranes are excited by a 10 cycle, 10V tone burst at 750kHz using wire bonded electrical connections to the device terminals which are the thick rails at the bottom and on the left side of the device.

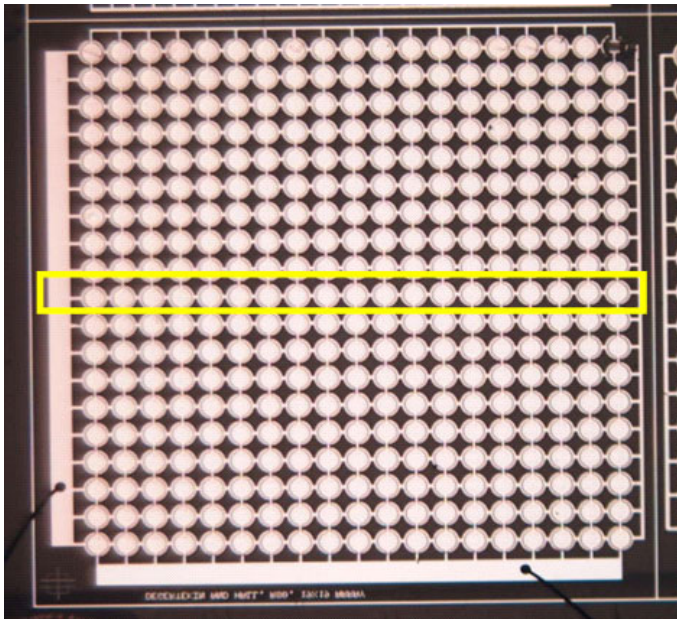

Figure 65 Micrograph of a 4X4mm cMUT array with 160μm elements

The cMUT location and the imaging phantom which consists of two 1mm diameter wire targets separated by 4mm and placed in front of an aluminum wall are

shown schematically in Figure 66. The imaged area is located 26mm away from the transducer.

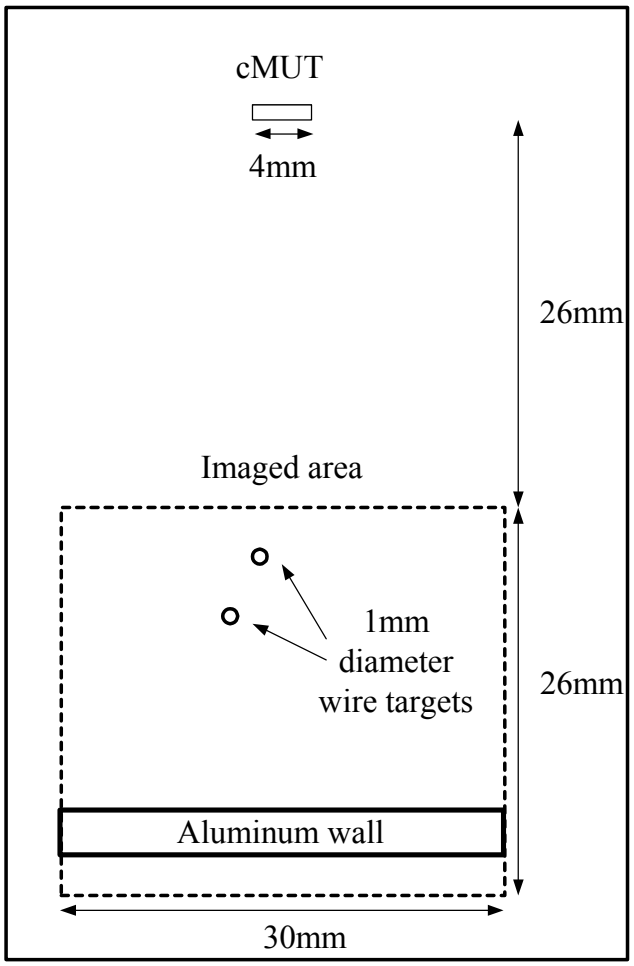

Figure 66 Schematic of a set-up used for ultrasonic imaging of two thin wires

For image reconstruction, the detection laser is scanned over a line of cMUT membranes at the center of the 2-D array as shown highlighted in Figure 65. Hence, a 1-D linear imaging array with 19 elements is implemented by measuring the vibration of one membrane from each column. The waveforms are digitized by a digital oscilloscope for each channel and stored in the computer for off-line synthetic aperture image

reconstruction. Figure 67 shows a trace from one of the channels showing the reflections from the wire targets in addition to the echo from the aluminum wall.

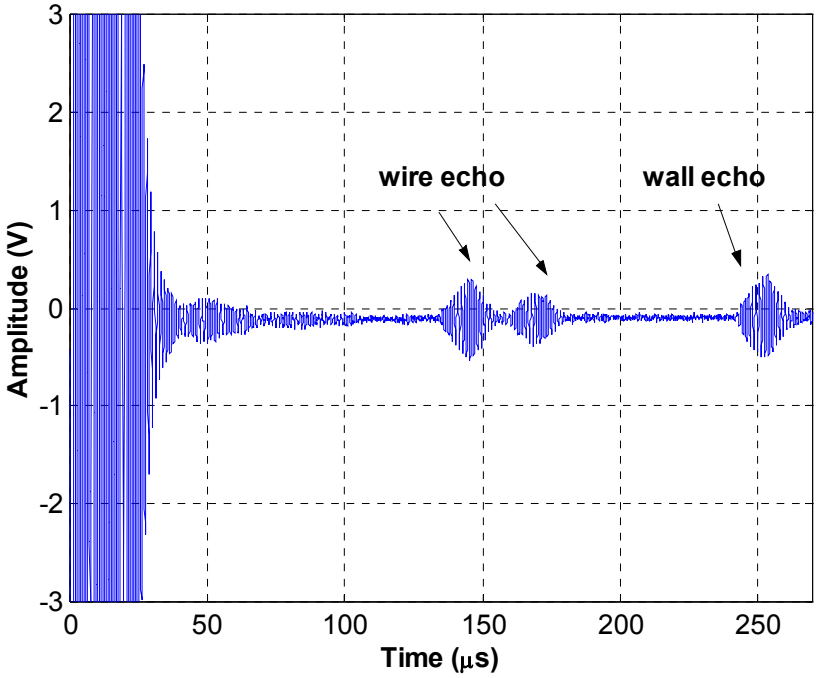

Figure 67 Time trace of the optical signal recorded from a single cMUT element during the imaging experiment described in Figure 66

The resulting image is shown in Figure 68, which is plotted with 20dB dynamic range after logarithmic compression. The two wire targets are clearly resolved with a side lobe level below 10dB. The image of the wall is clearly seen along with the shadowing effect of the wire targets. There are no grating lobes because the array was properly sampled for the reconstructed image (ultrasound wavelength in air at 750 kHz is 440μm, the element spacing is 225μm). The lateral resolution of the image is comparable to the theoretical predictions. Although the depth resolution is poor due to the narrow bandwidth of the cMUT (Q~15) the array can be used to map the boundaries of objects.

This example shows that by incorporating a 1-D VCSEL array and a silicon wafer with photodetectors a phased array with only 4mm size can be realized.

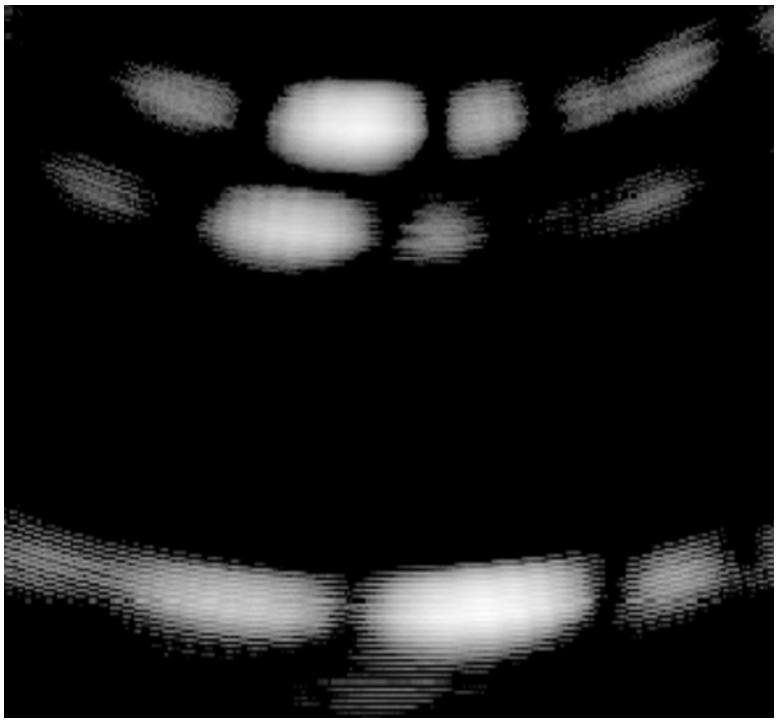

Figure 68 Reconstructed ultrasonic image of two wire targets

Discussion

The integrated optical detection method for cMUTs removes some of the limitations imposed by capacitive detection techniques while using the same efficient electrostatic transmission mechanism. The analysis of the phase sensitive grating structure integrated into the cMUT shows that the cMUT membrane displacement can be measured with interferometric sensitivity using small, low power lasers such as VCSELs and photodetectors integrated to CMOS electronics. With this integration scheme it will

be possible to implement cMUT arrays for imaging applications and provide optical isolation between transmit and receive electronics.

CHAPTER 8

SURFACED MICROMACHINED MICROPHONES

This chapter examines the viability of surface micromachined microphone structures. Devices very similar to the optical cMUTs are fabricated with extended etch channels that serve as volume cavities to reduce squeeze film stiffening. Characterization of these devices shows that a lossy wave propagation model is required to explain experimentally observed anomalies in the response. The wave model is then used to show the viability of fabricating acoustic microchannels with electrostatically controllable sound speeds. The final section of the chapter shows how such channels may be applied to create miniature surface micromachined microphones with electrostatically controllable directivity patterns.

Motivation

The displacement resolution measured during the Sandia optical microphone characterization is 6Å/√Hz near 1kHz. It is estimated that this figure can be improved by a factor of 5 with improved optics. Indeed, measurements presented on the optical cMUT structures which demonstrate better optics show a measured displacement resolution of 1Å/√Hz in the 20kHz to 100kHz range [60]. It has also been shown that the use of a Fabry Perot structure in conjunction with the diffraction based detection can improve this figure dramatically [61, 62]. Preliminary testing of these types of structures using metallic mirrors has shown an improvement by a factor of 3. For applications where power consumption is not an issue, a particularly simple approach for improving the

displacement resolution is using higher laser power. Recall from Chapter 1 that, for shot noise limited detection, the minimum detectable displacement scales with $1/\sqrt{I_{in}}$, where I_{in} is the laser power used. If the displacement sensitivity is improved to the 1×10^{-5}Å/√Hz range with any one or combination of these techniques, a variety of interesting acoustic transducer designs become possible as the demand for good compliance from the deformable structure becomes much less.

The possibility for broadband surface micromachined microphones is one such design. An example calculation was presented in Chapter 1 where it is shown that, with 1×10^{-5}Å/√Hz displacement resolution, a microphone compliance of only 5Å/Pa is sufficient to provide a 20dB pressure equivalent noise level across the audio bandwidth and a noise level of 33dB across a 200kHz bandwidth, which is where a diaphragm this stiff exhibits its fundamental resonance. Such a diaphragm can be made as small as 300μm diameter and can easily be fabricated with an integrated diffraction grating electrode using the surface micromachining process described for the cMUT fabrication. Surface micromachined structures have the advantage of being much simpler and less expensive to fabricate than bulk micromachined structures, which require machining on both sides of the silicon wafer. For the Sandia microphones, the bulk micromachining process is required as the back-side DRIE plays a critical role in creating the large back-side cavity to reduce squeeze film stiffening. Displacing this air is equally critical for the 300μm structure being described here as the stiffness of the air in a 2μm gap would limit the compliance to a mere 0.1Å/Pa. With the small diameter structure, however, the possibility exists of displacing the fluid in the gap laterally into larger volume reservoirs

created with the same surface micromachining process. This idea is tested with devices fabricated using the cMUT fabrication process.

Fabrication of Surfaced Micromachined Microphones

The process used to fabricate the surfaced micromachined microphones is almost identical as for the optical cMUTs presented in Chapter 7, with the difference being the addition of the horizontal volume reservoirs. The volume cavities used to soften the squeeze film stiffness should be made as rigid as possible. Otherwise, the cavities themselves will deform under acoustic pressure and act to restrain the displaced air from the diaphragm region from entering. An ideal way to enhance the rigidity of the cavities relative to the diaphragm is to perform an extra deposition of any stiff material on them. For example, a 2μm thick layer of metal can readily be sputtered to increase the stiffness. This, however, requires at least three extra steps in the fabrication process. To keep the fabrication simple, the horizontal cavities used in this case are made rigid by means of their geometry as they are formed into long channel structures with the stiffness primarily determined by the channel width, which is kept small relative to the membrane size.

Three completed microphone elements are shown in Figure 69, a micrograph of the top-side of a 9 element array. Each microphone consists of a 200μm diameter diaphragm connected to four 530μm long channels which provide the added volume necessary to reduce the squeeze film stiffness. For some devices, the ends of these channels are sealed with UV cured epoxy to create a microphone structure capable of responding down to DC. One such device is illustrated in the far left side in Figure 69. For other devices the channels are left open, which results in a microphone with a low

frequency cutoff. The remaining features observed in the figure are connections for the bottom electrode in the array.

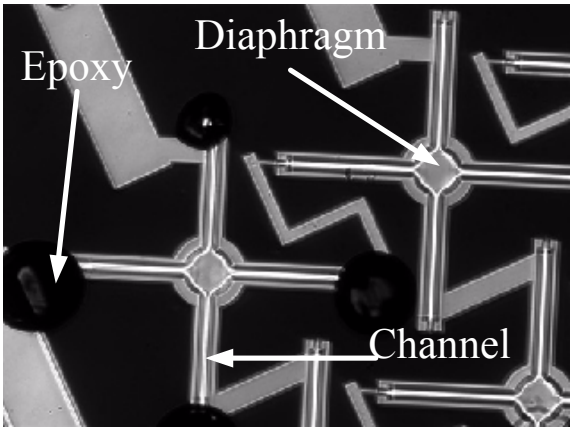

Figure 69 Micrograph of surface micromachined microphone optical microphone structures

The displacement sensitivity calibration for these devices was performed in a manner identical to that described for the Sandia microphones. As in the case of the optical cMUTs, these devices produce interference curves with an intensity swing close to 80%. Figure 70 shows the first diffracted order intensity vs. gap height for one of the elements in the array of Figure 69.

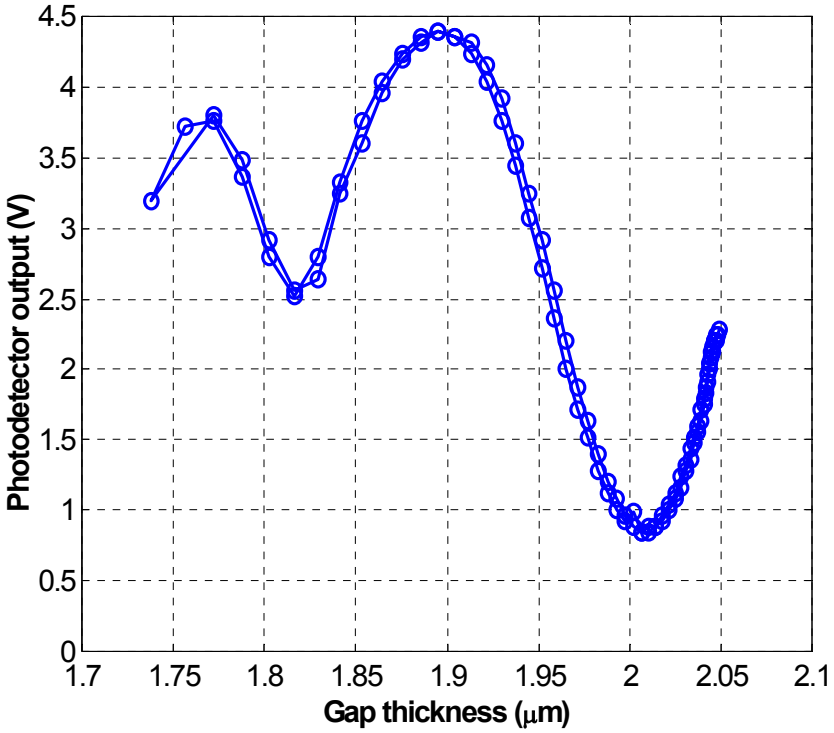

Figure 70 First diffraction order intensity vs. gap thickness for a surface micromachined optical microphone

Dynamic Characterization

Analytical equations for the stiffness of the 200μm Al membrane predict a compliance of roughly 1Å/Pa. When the total back-side air volume is taken as the sum of the volume behind the membrane plus the sum of the volumes in all four channels, the resulting compliance of the structure is expected to be 0.5Å/Pa, which is computed using the equation for the isentropic compression of a gas as described in the equivalent circuit modeling section of Chapter 4. When the air directly behind the membrane ceases to displace to the channels, the resulting compliance is expected to be reduced to 0.1Å/Pa.

The purpose of the dynamic characterization is to study the frequency dependence of the membrane compliance, thereby assessing the viability of the horizontal cavity approach.

All characterization measurements presented in this chapter are performed using electrostatic excitation. The response is first measured in vacuum to determine the dynamic properties of the membrane alone, without complexities caused by the presence of the air in the gap. This measurement is shown in Figure 71 along with predictions from a simple lumped model for the membrane which is used to extract the compliance near DC. The model uses an effective mass of 60% of the total computed membrane mass to account for the distributed deflection profile. The membrane stiffness is adjusted to match the resonance frequency shown which allows extraction of the compliance. These measurements provide a value of the 0.95Å/Pa.

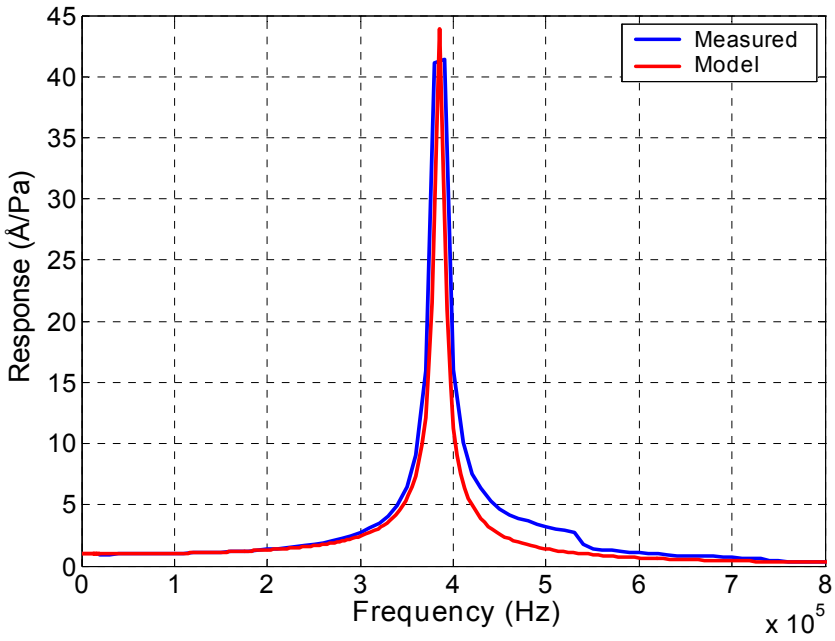

Figure 71 Dynamic response of the surfaced microphone in vacuum

The response is then measured in air to asses the effectiveness of the horizontal air cavities. This is performed on two structures, one with the channels left open and the other with the channels sealed with the UV cured epoxy. The measured responses are shown in Figure 72. Several important observations can be made. As expected, the compliance of the sealed structure is reduced only slightly to a value of 0.7Å/Pa near DC due to the additional stiffness presented by the back-side air volume. The additional volume provided by the channels is effective in this low frequency range. However, at approximately 2kHz, the compliance of the sealed channel device begins to decrease significantly as the air behind the diaphragm no longer has time to enter the channels due to flow resistance. The sensitivity is reduced to a value of 0.3Å/Pa when this occurs. This sealed data alone provides a complete demonstration of the proposed technique: The surfaced micromachined horizontal air cavities increase the effective volume of the back-side cavity and reduces the squeeze film stiffening caused by the thin 2μm air gap. In this case, the technique works up to 2kHz. Different geometries may extend this frequency cutoff significantly.

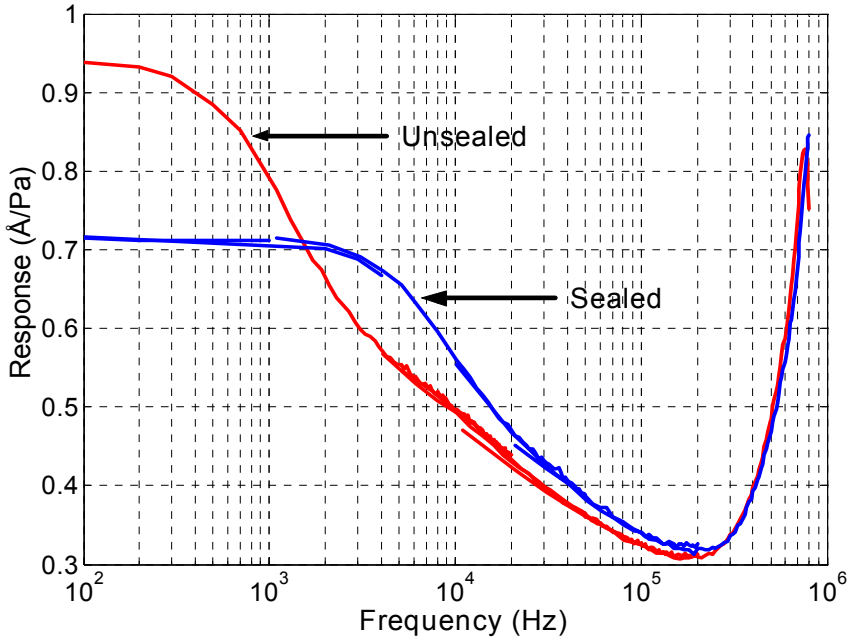

Figure 72 Response of the surfaced micromachined microphones in air with open channels and sealed channels

For the open channel structure, the compliance at DC is that of the membrane itself, since the air in the back-side volume is free to displace out of the open end of the channels. At higher frequencies, however, the losses in the channels prevent the air from leaving and the response becomes stiffened as in the sealed channel case. As expected, the responses converge at high frequencies (approximately 20kHz) where the channels become equally dysfunctional in both cases due to the flow resistance. Comparison of Figure 72 with Figure 71 also illustrates how the resonance frequency of the structure is increased due to the presence of the air in the back-side volume.

An interesting feature of the data is that the structure with the sealed channels has a larger compliance than the open channel structure over a certain frequency range, namely from 1kHz to 20kHz as can be observed in Figure 72. This is not intuitive as this implies that constraining the fluid at the end of the channel has the ability to make the

structure softer under certain circumstances. When lumped circuit models such as the one presented for the Sandia microphone in Figure 29 are applied to this structure, the trend cannot be accounted for. This motivated the investigation of a lossy wave model for the channels which is able to predict the trend and fit the data accurately. The model shows that the boundary conditions applied at one end of a channel can be transformed in amplitude and phase at the other end. This, in turn, explains why the air underneath the diaphragm is capable of seeing a softer channel impedance for a sealed channel than for a channel left open.

Lossy Wave Model for Acoustic Microchannels

An equivalent circuit for the surface micromachined microphones with the lossy wave model incorporated is shown in Figure 73. The left hand side of the model is identical in structure to the model for the Sandia microphones as presented in Figure 29. In this case, the volume of fluid displaced by the 200μm Al membrane as it deflects must either be compressed in the 2μm squeeze film gap behind the membrane or it must enter the acoustic channels. In a typical lumped model for the channels, the impedance presented to the air in the squeeze gap consists of a resistive and inertia component. A model based on this approach is able to capture the cutoff behavior of the data in Figure 72, but is unable to capture the counterintuitive behavior regarding the channel boundary conditions.

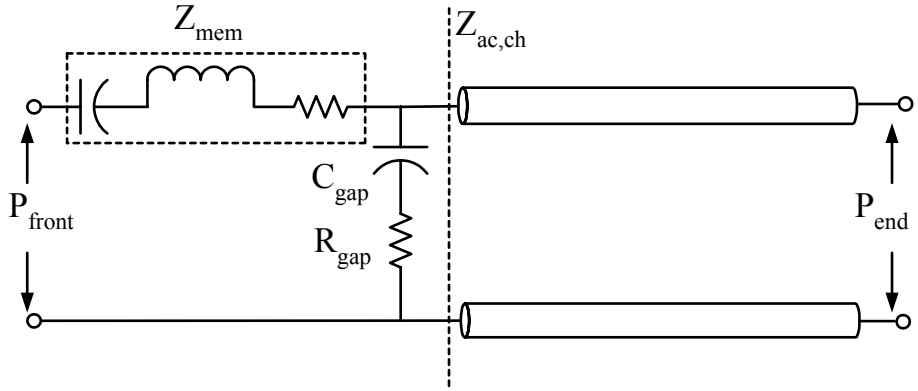

Figure 73 Equivalent circuit schematic for the surface micromachined microphones with the lossy wave model incorporated

For the lumped channel model, the flow resistance is computed using a simple analytical expression for slot flow where the total resistance is proportional to the length of the channel [30]. An easy way to get at a wave model is to, instead, look at the slot flow on a per length basis and formulate a differential momentum equation to include the effect. The slot flow resistance per unit length, R, is then

$$R = 12\mu / g^2 \tag{42}$$

where μ is the viscosity of the air. A momentum balance on a fluid particle in the channel gives

$$-\frac{\partial P}{\partial x} = \rho_0 \frac{\partial v}{\partial t} + Rv \tag{43}$$

where ρ_0 is the air density and v is the fluid particle velocity. With this momentum equation, a wave equation can be derived as

$$v_{xx} - \frac{1}{c_0^2} v_{tt} - \frac{R}{\rho_0 c_0^2} v_t = 0 \tag{44}$$

where c_o is the sound speed of air in a lossless medium. Finally, a dispersion relation can readily be extracted from the modified wave equation as

$$k^2 = \frac{\omega^2}{c_0^2} - \frac{j\omega R}{\rho_0 c_0^2} \tag{45}$$

The propagation impedance for waves in the channel is complex. Furthermore, the channel impedance seen by the squeeze film gap at the entrance of the channel, refereed to $Z_{ac,ch}$ in Figure 73, is the result of a standing wave due to the reflection at the end. This is schematically illustrated in Figure 74. For open channels, a pressure release condition is assumed, and for epoxy sealed channels a rigid boundary is assumed. This provides two cases for the reflection coefficient, *RC*, as shown in Figure 74. In both cases, the acoustic channel impedance consists of a resistive component and a stiffness component as

$$Z_{ac,ch} = R_{ch}(\omega) + \frac{1}{j\omega C_{ch}(\omega)} \tag{46}$$

For the open channel, the presence of stiffness instead of a mass is somewhat counterintuitive and in contrast to the assumption made in traditional lumped channel models.

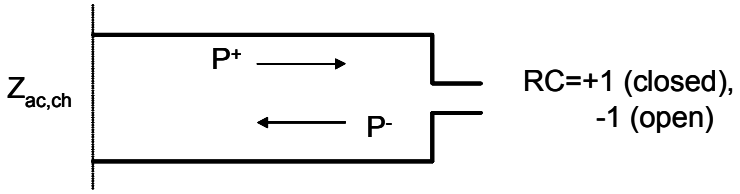

Figure 74 Schematic of a microchannel illustrating the standing wave behavior

The frequency dependence of R_{ch} and $1/C_{ch}$ helps to explain the measured response behavior in Figure 72. The model results for R_{ch} and $1/C_{ch}$ for an open ended channel are shown in Figure 75 and Figure 76. At low frequencies, R_{ch} converges to the value used in the lumped model, where the fluid in the channel does indeed oscillate as a

whole. At higher frequencies, the channel resistance locally restricts the air from moving near the entrance of the channel and, instead, the air begins to compress as a wave is propagated. Note that the actual values for a single channel are 4X that shown here, since $Z_{ac,ch}$ is the result of 4 channels in parallel.

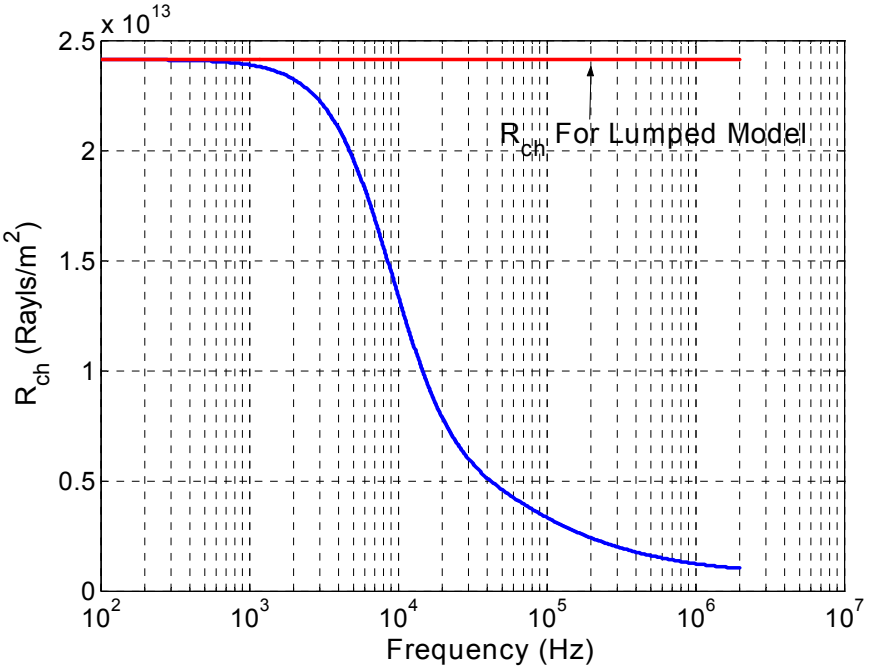

Figure 75 Resistive component of microchannel impedance

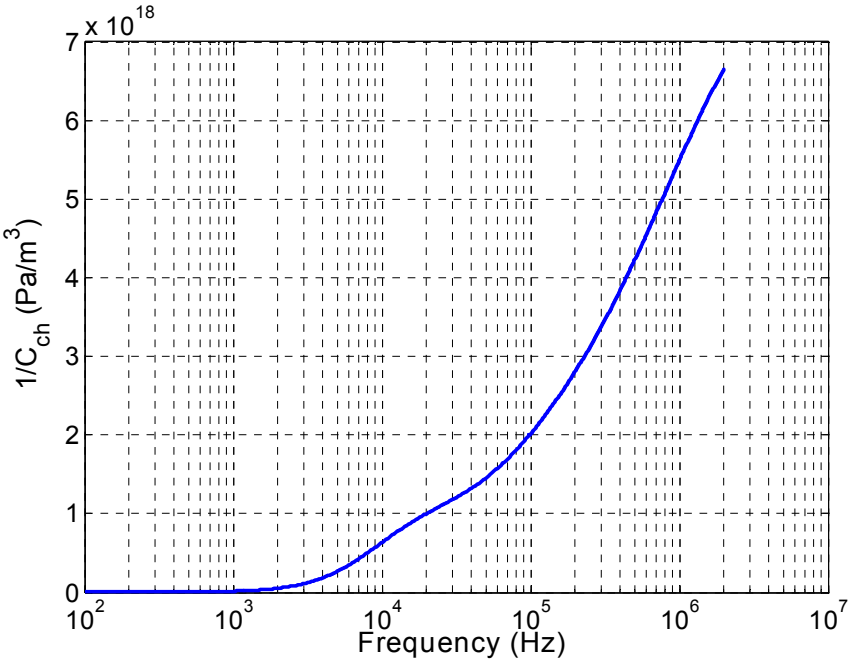

Figure 76 Stiffness component of microchannel impedance

When this model for the channels is incorporated into the equivalent circuit model as shown in Figure 73, the simulation results capture several interesting trends of the measured response data as can be observed in Figure 77. For the open channel case, the model captures the initial roll off in the response beginning at 200Hz, and also a second bend occurring near 3kHz. The model also captures the decay in compliance for the sealed channel. In this case, however, the compliance of the structure predicted by the model at DC is slightly off. Finally, the most interesting feature captured by the model is the prediction of a larger response value for the sealed structure in the 4kHz to 20kHz frequency range. Although this range does not exactly align with the experimental data, the model does offer a good approximation.

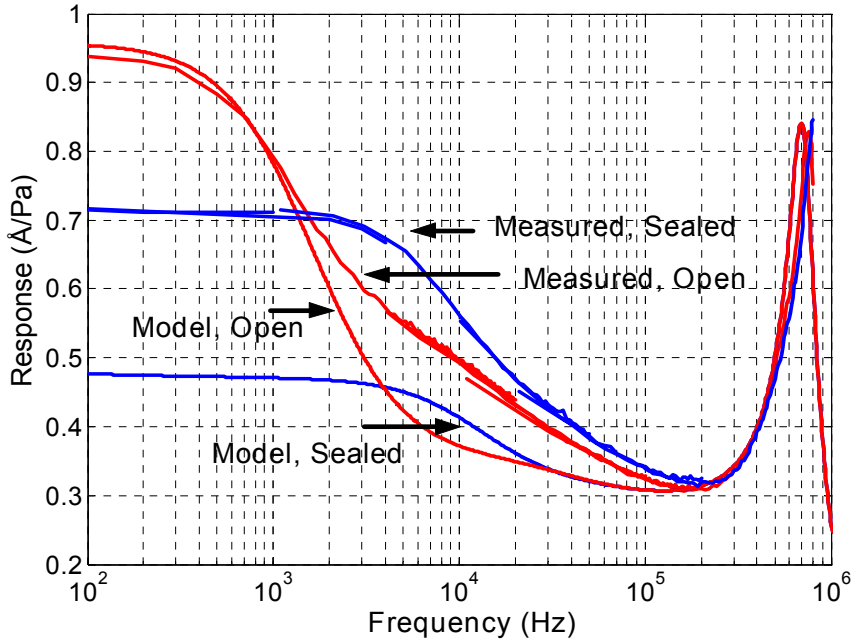

Figure 77 Measured and modeled response of the surface micromachined microphone

The modeling work presented in this chapter has inspired the consideration of a design for microchannels with controllable sound speeds. Such a design could potentially have application to the creation of surfaced micromachined microphones with mechanically adjustable directivity patterns. These ideas are presented in the final two section of this chapter.

Acoustic Microchannels with Controllable Sound Speed

The type of micromachined channels used in the optical microphone designs can be used for a variety of functions and are employed in many MEMS devices outside of acoustic transducers [63]. In this section, a design is proposed which uses the following principles: One of several viable actuation techniques such as capacitive, piezoelectric, or thermal actuation can be used to control the height of a fabricated micro channel. As

expressed in Equation 42, the channel height has a strong influence on the flow resistance due to the inherent viscosity of the fluid. In turn, the channel flow resistance affects the channel wave speed as is made clear in the dispersion relation in Equation 45. These actuation signals can therefore be used to control the wave speed in the channel. A schematic of the design is shown in Figure 78.

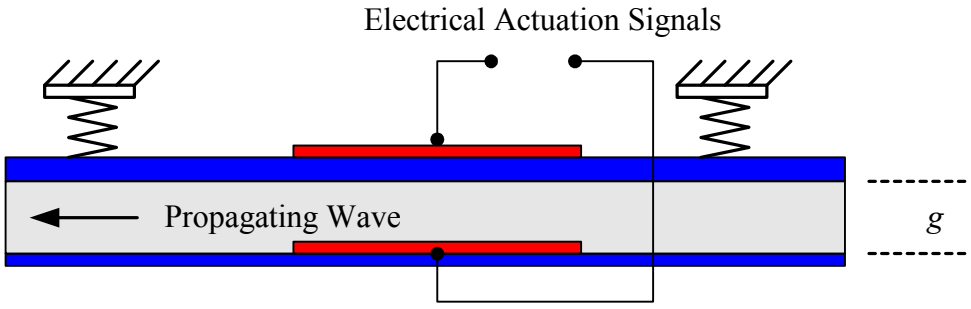

Figure 78 Schematic of a microchannel with controllable sound speed

To illustrate the sensitivity of the flow resistance to the channel gap height, Equation 42 is plotted in Figure 79 using properties of air. As the figure shows, the resistance has a high sensitivity to channel height for channels on the order of 1-2μm. Channels of these dimensions can be readily fabricated with standard, well established surface micromachining techniques as demonstrated with the optical microphone structures presented in this chapter.

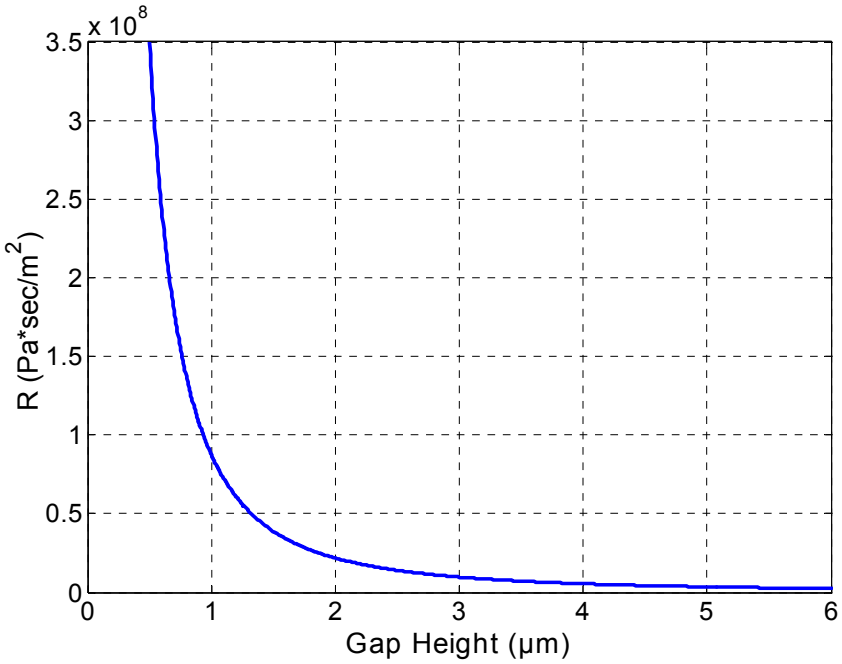

Figure 79 Slot flow resistance vs. channel gap height for air

To illustrate the effect of the gap height on the wave speed in the channel, the dispersion relation in Equation 45 is used to plot the magnitude and phase of a forward propagating 1 kHz wave in an air filled channel. Figure 80 shows the results for a channel height of 1 and 2μm. Note that by controlling the gap height across this range, which can readily be done with electrostatic actuation for example, the phase accrued after 1 mm of propagation is doubled from ~40 to ~80 degrees. When the channel height is set to a very large value, the wave speed approaches that of lossless propagation in open space. In this case, the phase accrued over 1mm is only 1 degree. This analysis shows that by controlling the channel height, the sound speed can be controlled over a range of 80X.

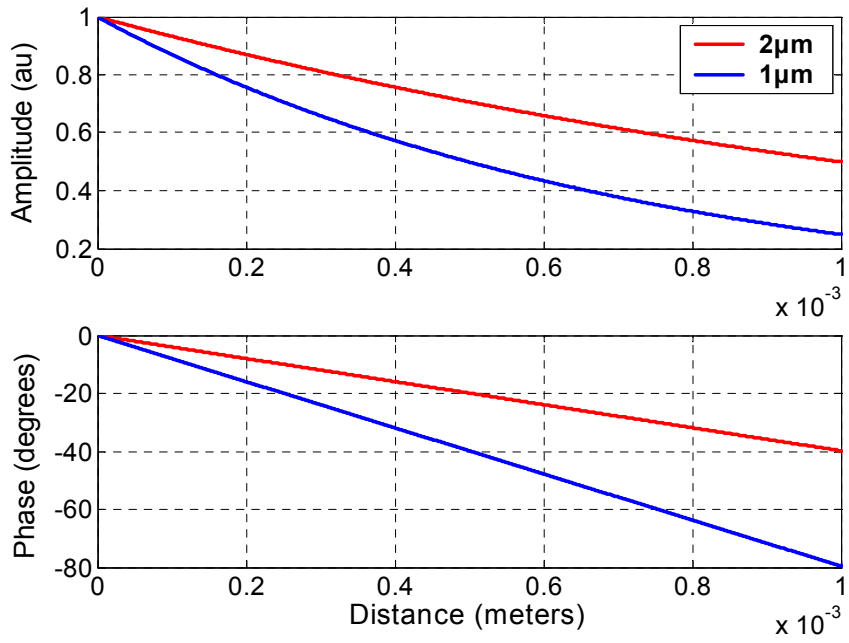

Figure 80 Amplitude and phase of a forward propagating wave in a 1µm and 2µm channel

Figure 80 also illustrates the fact that slowing the sound speed comes at the expense of attenuating the signal. For the 2µm channel height, for example, the signal is 50% attenuated after 1mm of propagation. For applications where the attenuation is problematic or undesirable, the use of multiple channels in parallel may be a viable design for building the signal to the required level. An alternative idea that can be investigated is the use of a horn structure, where the channel cross section is made smaller along the direction of propagation to compensate for the attenuation.

Mechanically Adjustable Directivity Pattern Microphones

The final section of this chapter provides an example to illustrate the utility of the acoustic microchannels. In this example, a compliant membrane is suspended above

a back-side air cavity which is connected to a channel with adjustable sound speed and open at the opposite end. The following analysis shows how control of the channel height leads to control of the directivity of the microphone – from a figure 8 to a cardioid to an omni directional pattern. In this manner, the directivity is implemented and controlled directly in the analog physical acoustic environment. Furthermore, this directional microphone requires the use of only a single membrane and can be realized with structures less than 1mm in size.

Figure 81 shows a schematic of the device under consideration and an equivalent circuit model to aid in the description of the operation. This analysis is described in the frequency domain and all pressures referred to are complex amplitudes. The microphone membrane is driven by the net pressure P_{front}-P_{gap}. The front-side pressure is directly applied from the acoustic signal. In addition, the incoming signal applies a pressure to the end of the channel, P_{end}, which has the same magnitude as P_{front} but differs slightly in phase depending on the direction of incidence. For example, if the channel is 1 mm long, the phase of P_{end} has a range of +/- 1 degrees. The phase of P_{gap} is equal to the phase of P_{end} plus whatever phase is accrued from propagation in the channel. Adjusting the phase of P_{gap} provides control of the directivity of the microphone, as the following simulation for three different channel heights illustrates.

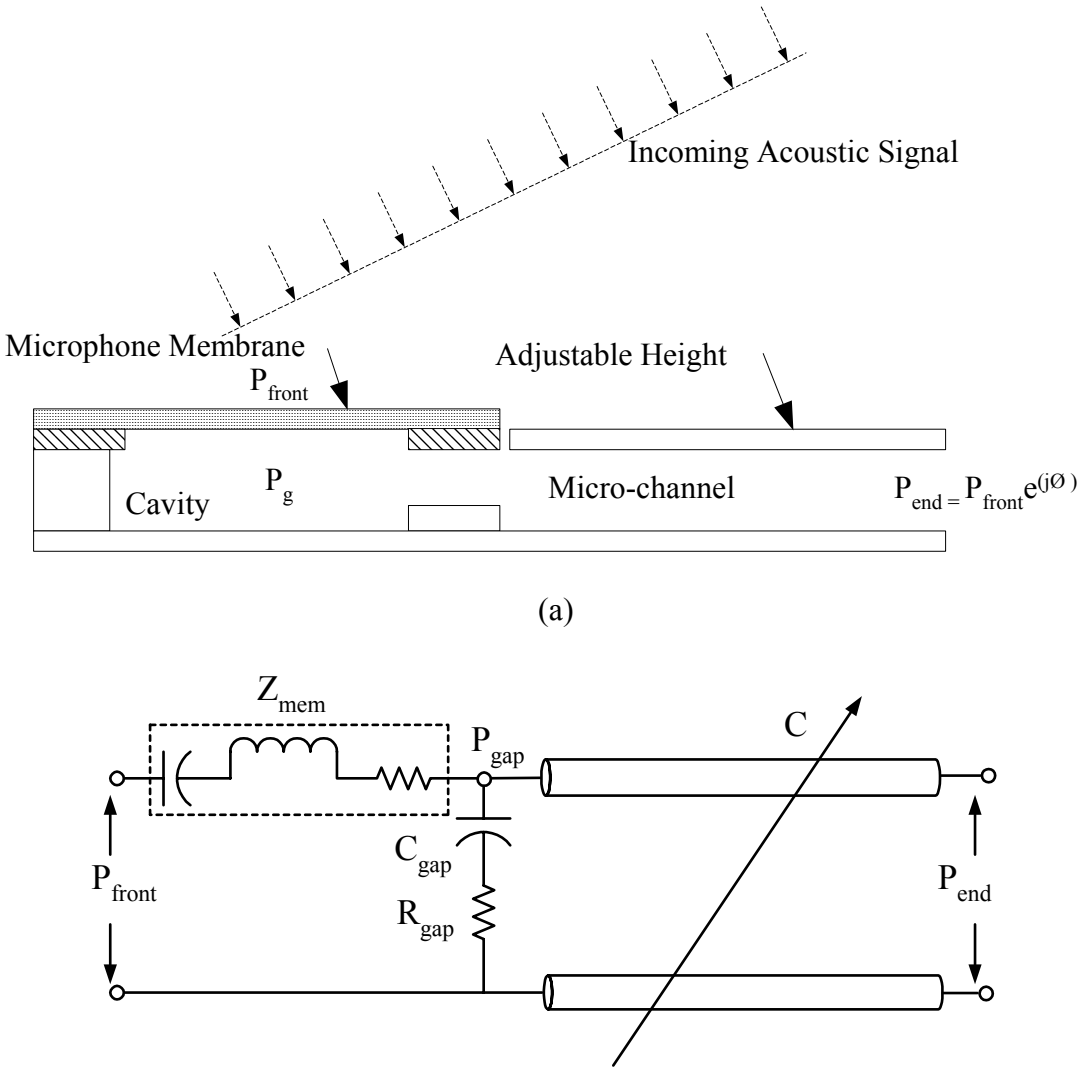

Figure 81 Schematic of a micromachined microphone with adjustable directivity

At a channel height of 20μm, the losses in the channel are very small and zero additional phase is added. P_{gap} and P_{end} have the same phase, and the microphone can be considered a purely pressure gradient type [9]. In this case, the common figure 8 pattern results as shown in Figure 82. For a channel height of 10μm, the losses in the channel are such that P_{gap} is slightly shifted in phase from P_{end} so that phasor cancellation with

respect to P_{front} occurs only at a 90^0 angle of incidence. The overall directivity pattern is that of a cardioid. For a channel height of 5μm, the losses in the channel shift P_{gap} significantly with respect to P_{front} and no cancellation is observed. The pattern approaches that of a purely omni directional microphone in this case

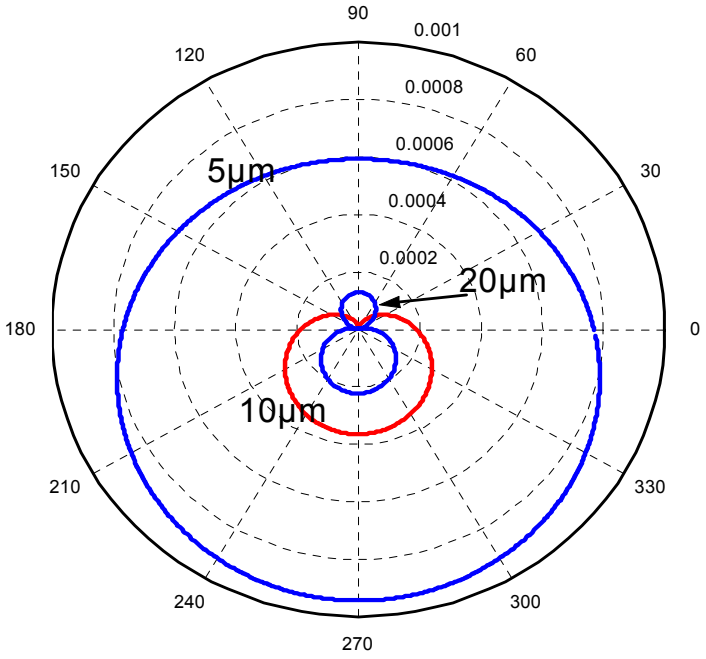

Figure 82 Directivity plots of a surface micromachined microphone with integrated adjustable microchannels for three channel heights

The three cases plotted in Figure 82 also show that directivity comes at the expense of sensitivity. This trade off is particularly pronounced for the miniature microphone proposed here since pressure gradients across the 1mm channel length are quite small in the audio frequency range. If the displacement sensitivity is high enough, however, these designs can lead to directional microphones in $1mm^3$ volumes. Alternatively, a design which uses a spiraled channel structure with a long length of

channel wrapped in a small area may provide directionality without sacrificing sensitivity. More complex directivity patterns can also be created by combining several of the devices presented here, or, potentially from the use of a single membrane with a more complicated channel structure.

CHAPTER 9

CONCLUSIONS

Micromachined microphones with integrated diffraction grating based optical displacement sensors have been demonstrated with designs fabricated using Sandia National Laboratory's dedicated fabrication technology. Characterization of these devices with a custom designed optoelectronically integrated test bed verifies the interference behavior and resulting interferometric displacement sensitivity obtained from zero and complementary higher order modes as predicted by a 1-D scalar diffraction model.

Detailed characterization of the microphone structure is performed via an electrostatic actuation port integrated into the device which is isolated from the optical displacement detection. Broadband characterization of the diaphragm in vacuum shows resonance peaks corresponding to as high as the 14^{th} vibration mode. Results from a finite element model modal analysis that incorporates many complications of the diaphragm structure including tension in the nitride membrane and the distributed mass and stiffness of the top polysilicon electrode show excellent agreement with the measured resonance data. A coupled physics finite element model is also used to accurately predict the electrostatic pull-in behavior of the microphone diaphragm which is important for displacement sensitivity tuning.

Electrostatic characterization in air shows a high frequency cutoff of the microphones between 1kHz and 10kHz, which is well below the 50kHz fundamental diaphragm resonance frequency measured in vacuum. Simulations of an equivalent

circuit model for the device suggest that this is caused by squeeze film stiffening of the air in the diaphragm – back-plate gap. Multiple experiments performed at different gap heights show a shift in the high frequency cutoff which confirms the model predictions.

Measurements were performed in the anechoic testing chamber to asses the frequency response and the internal noise of the optical microphones. With 5mW incident laser power, an A weighted displacement resolution of 2.4×10^{-2}Å is measured which, for properly designed microphone structures with a 20kHz bandwidth, should correspond to 17dBA internal noise. The low upper cutoff frequency of the Sandia devices results in an A weighted noise level of 39.9dBA.

The diffraction based detection method is also applied to cMUTs fabricated with diffraction grating back electrodes on quartz substrates. Measurements show a high displacement resolution of 2×10^{-4}Å/√Hz across the ultrasonic frequency range from each 160μm element in a 4mm×4mm cMUT array. The high sensitivity and dynamic range in transmit of these devices is employed in the phased array ultrasonic imaging of two thin wires.

Finally, surfaced micromachined microphones are fabricated and characterized with a procedure similar to that used for cMUTs. The use of horizontal cavities to reduce the high squeeze film stiffness associated with thin gap structures is demonstrated. A lossy wave model for the horizontal channel structure used in this demonstration was developed to capture the trends in the measured response data. The model, in turn, inspired the consideration of surface micromachined microphones with integrated channels used to adjust the phase of the backside cavity pressure acting on the microphone diaphragm and, in turn, the directivity pattern of the device. Simulations of

the design show that a microphone 1mm in size can be adjusted across a full extent of directivity patterns – from a figure 8, to a cardioid, to an omnidirectional pattern.

Recommendations

Several recommendations for future work are offered. Many of these can be pursued using the current Sandia devices and experimental set-up. First, the range of the interference curves produced by the Sandia devices is only 20% of the theoretically predicted swing, which predicts total cancellation of intensity for all orders other than the zero order at gap heights of $\lambda/2$ multiples. Since the displacement sensitivity is directly proportional to this swing, a five times improvement in signal to noise is the potential reward for this effort. It is clear from the characterization work performed in this thesis that the diaphragm deflects with a uniform parallel profile, so this can be ruled out as a potential reason for the poor swing. The primary recommendation offered is the use thicker metallic depositions on the backside of the grating. Metals other than gold should also be tried as the particular deposition conditions for gold in the MiRC cleanroom may be causing complications. Failing this, a detailed diagnosis of the diffracted field using CCD cameras is recommended to test the overlapping of orders on the PD plane.

Another important issue which can be studied with the current experimental setup is the integration of a control loop to alleviate drift in the displacement sensitivity, which is an undesirable feature common to all optical interferometers. For the microphone designs presented here, however, several enabling features of the device may be taken advantage of. If the microphone diaphragms are designed with a large bandwidth, the integrated electrostatic actuation port can be used to vibrate the diaphragm at ultrasonic

frequencies as the distortion in the higher order harmonics is monitored as the error signal. The same electrostatic actuation port can then be used to adjust the DC bias voltage such that the distortion is kept at zero, since this also corresponds to maximum displacement sensitivity. This method has the advantage of using an error signal with a zero level reference and has recently been employed in optical metrology [64, 65].

In future work, the back-plate design of the Sandia devices can be improved to provide microphones with diaphragm resonance frequency limited bandwidths. A particularly attractive design is the use of a cantilever structure to hold the bottom diffraction grating electrode in place. This design can resemble the one shown in Figure 18, which has four thick cantilevers. Simple analytical calculations show that a single branch is more than adequate to rigidly hold the electrode. Reducing the back-plate flow resistance will also reduce the thermal acoustic noise which is the dominant source over the 1kHz-10kHz range.

Initial work with Fabry-Perot structures shows promising results [61, 66]. This is certainly worthy of continued investigation, as theoretical calculations for structures using low loss dielectric mirrors predict the ability to achieve displacement resolutions in the 10^{-7}Å/√Hz range. It this is demonstrated, the applicability of the detection method to the high impact applications of immersion cMUTs should be given consideration. In addition, the directional microphone structures presented in Chapter 8 may create high impact applications as well when combined with recent developments in signal processing for miniature microphone arrays [67].

Finally and most importantly, the optoelectronic integration of an optical microphone using VCSELs and tightly integrated photodiodes should be pursued as the

miniaturization feature of the method is a great portion of its overall value. The integration will require detailed characterization of VCSEL beam divergence patterns. Preliminary tests show that the use of collimation optics at the microscale will be beneficial for some designs in collecting and using all the available light. Relative intensity noise measurements of VCSELs operating in CW mode show values comparable to regular sized laser diodes, which are reasonable. However, these measurements should also be performed in pulsed operating mode to verify the feasibility of low noise, low power microphones for remote hearing applications.

APPENDIX 1

ELECTROSTATICS FINITE ELEMENT MODEL CODE

```
finish
/clear
/prep7                          !clear database

elemsize=20
V=15

emunit,epzro,8.854e-6           !free space permittivity

et,1,181                        !shell element used for mem and grating

et,2,123                        !electrostatic element for air and
nitride

keyopt,1,3,0
keyopt,1,8,1
keyopt,1,9,0
keyopt,1,10,0

R,1,thmem

mp,ex,1,200e3                   !mat props for membrane
mp,nuxy,1,.24
mp,alpx,1,23.2e-6

mp,perx,3,3.9                   !elec props for material 3 (air volume)

!!!!!!!!!!BUILD MEMBRANE AND TOP ELECTRODE !!!!!!!!!!
!!!!!!!!!!!!!!!!!!!!!!!!!!!!!!!!!!!!!!!!!!!!!!!!!!!!

widfing=3
spc=5
lenfing=40
thmem=0.8
gap=2.0

numstr,area,700
rectng,0,1050,0,1050            !nitride membrane

numstr,area,800
rectng,80,120,725,875
agen,4,800,800,1,200,0,0,,,0
agen,4,800,803,1,0,-200,0,,,0
rectng,125,275,680,720
agen,4,816,816,1,200,0,0,,,0
agen,3,816,819,1,0,-200,0,,,0
```

```
numstr,area,850
rectng,0,75,680,720
agen,3,850,850,1,0,-200,0,,,0
rectng,280,320,0,75
agen,3,853,853,1,200,0,0,,,0

numstr,area,950
rectng,0,160,90,120
rectng,140,160,0,90

numstr,area,1100
rectng,325,475,80,120
agen,3,1100,1100,1,200,0,0,,,0

numstr,area,1200
rectng,0,100,0,50       !create optical reflector
allsel,all

aovlap,all
asel,s,area,,1204
asel,a,area,,1205
cm,mem,area
allsel,all

cmsel,u,mem,area
cm,poly,area
allsel,all

wplane,1,0,0,0,1,0,0,1,0,1    !create remaining areas for air volume

numstr,area,1300
rectng,0,1050,-(thmem+gap),0
agen,2,1300,1300,1,0,1050,0,,,0
wplane,2,0,0,0,0,-1,0,0,-1,2
rectng,-1050,0,-(thmem+gap),0
agen,2,1302,1302,1,1050,0,0,,,0
wplane,3,0,0,-(thmem+gap)
rectng,0,1050,0,1050
wplane,4,0,0,0
allsel,all

numstr,area,1000
wplane,3,0,0,-(thmem+gap)
rectng,0,100,0,50       !create cantilevered region of bottom electrode
numstr,area,2000
rectng,0,1,0,lenfing          !create etched regions between fingers
rectng,4,6,0,lenfing
agen,12,2001,2001,1,spc,0,0,,,0

rectng,70,85,0,40

asel,s,area,,2000,2014
cm,etch,area
allsel,all
numstr,area,3000
asba,1000,etch
asel,s,area,,3000
```

```
cm,grating,area               !group grating area into comp
allsel,all
wplane,4,0,0,0


aovlap,all
aglue,all
allsel,all

va,all
cm,air,volu

!!!!!!!!!!!! MESH MODEL !!!!!!!!!!!!
!!!!!!!!!!!!!!!!!!!!!!!!!!!!!!!!!!!!

mshape,0,2d

cmsel,s,mem,area
type,1
real,1
mat,1
esize,elemsize
amesh,all

cmsel,s,poly,area
type,1
real,1
mat,1
esize,elemsize
amesh,all

cmsel,s,grating,area
type,1
real,1
mat,1
esize,elemsize
amesh,all

mshape,1,3d

cmsel,s,air,volu
vatt,3,,2
esize,elemsize
vmesh,all

!!!!!!!! APPLY ELECTROSTATIC BCS AND WRITE FILE !!!!!!!!
!!!!!!!!!!!!!!!!!!!!!!!!!!!!!!!!!!!!!!!!!!!!!!!!!!!!!!

cmsel,s,poly,area       !apply voltage to top electrode
asel,u,area,,1202
da,all,volt,V
allsel,all

asel,s,loc,z,-(thmem+gap)
da,all,volt,0
allsel,all
```

```
asel,s,loc,z,0
sfa,all,,mxwf
allsel,all

cmsel,s,grating,area
sfa,all,,mxwf
allsel,all

et,1,0

physics,write,ELECTROS        !write electrostatic physics file
physics,clear

!!!!!!!!!!!!!!!! WRITE STRUCTURAL PHYSICS FILE !!!!!!!!!!!!

emunit,epzro,8.854e-6         !free space permittivity

et,1,181                !for mem and grating
et,2,0                        !electrostatic element

keyopt,1,3,0
keyopt,1,8,1
keyopt,1,9,0
keyopt,1,10,0

R,1,thmem

mp,ex,1,200e3                 !mat props for mem
mp,nuxy,1,.24
mp,alpx,1,23.2e-6

!!!!!!!!!!APPLY STRUCTURAL BCS AND WRITE FILE !!!!!!!!!
!!!!!!!!!!!!!!!!!!!!!!!!!!!!!!!!!!!!!!!!!!!!!!!!!!!!!!!!!!!!

lsel,s,loc,x,1050
lsel,r,loc,z,0
dl,all,,ux,0
dl,all,,uy,0
dl,all,,uz,0
dl,all,,roty,0

lsel,s,loc,y,1050
lsel,r,loc,z,0
dl,all,,ux,0
dl,all,,uy,0
dl,all,,uz,0
dl,all,,rotx,0

lsel,s,loc,x,0
lsel,r,loc,z,0
dl,all,,ux,0
dl,all,,roty,0

lsel,s,loc,y,0
lsel,r,loc,z,0
dl,all,,uy,0
dl,all,,rotx,0
```

```
allsel,all


cmsel,s,grating,area
lsla,s
lsel,r,loc,x,100
dl,all,,ux,0
dl,all,,uy,0
dl,all,,uz,0
allsel,all

cmsel,s,grating,area
lsla,s
lsel,r,loc,y,50
dl,all,,ux,0
dl,all,,uy,0
dl,all,,uz,0
allsel,all

cmsel,s,grating,area
lsla,s
lsel,r,loc,x,0
dl,all,,ux,0
dl,all,,roty,0
allsel,all

cmsel,s,grating,area
lsla,s
lsel,r,loc,y,0
dl,all,,uy,0
dl,all,,rotx,0
allsel,all

finish
physics,write,STRUCTURE

/solu

ESSOLVn,'ELECTROS','STRUCTURE',3,0,'air',,0.05,0.05,10,-1,1

Finish
```

APPENDIX 2

MODAL ANALYSIS FINITE ELEMENT CODE

```
!this code works

finish
/clear
/prep7                  !clear the database

et,1,shell91,,1
et,3,shell91,,1

mp,ex,1,270e3           !membrane material properties
mp,nuxy,1,.27
mp,alpx,1,23.2e-6
mp,dens,1,3000e-18
thk_1=0.8

mp,ex,2,1e3             !polysilicon material properties
mp,nuxy,2,.27
mp,alpx,2,23.2e-6
mp,dens,2,2700e-18
thk_2=2.5

keyopt,1,1,5
keyopt,1,4,0
keyopt,1,5,1            !output values at shell layer middles
keyopt,1,6,1
keyopt,1,8,1
keyopt,1,9,0
keyopt,1,10,0
keyopt,1,11,1

keyopt,3,1,5
keyopt,3,4,0
keyopt,3,5,1            !output values at shell layer middles
keyopt,3,6,1
keyopt,3,8,1
keyopt,3,9,0
keyopt,3,10,0
keyopt,3,11,1

R,1,2,0,,,,0            !real constant set 1 is for the composite areas
Rmore,,,,,,
Rmore,1,0,thk_1,,,      !mat number for 1st layer and geom data
Rmore,2,0,thk_2,,,      !mat number for 2nd layer and geom data

R,3,1,0,,,,0            !real constant set 3 is for the single areas
Rmore,,,,,,
Rmore,1,0,thk_1,,,
```

```
!!!!!!!!!!BUILD MEMBRANE AND TOP ELECTRODE !!!!!!!!!!
!!!!!!!!!!!!!!!!!!!!!!!!!!!!!!!!!!!!!!!!!!!!!!!!!!!!

numstr,area,700
rectng,0,2100,0,2100          !nitride membrane
asel,s,area,,700
cm,mem,area                   !group mem into comp

numstr,area,800
rectng,175,325,1730,1770      !create all horizontal electrodes
agen,9,800,800,1,200,0,0,,,0
agen,3,800,808,1,0,-200,0,,,0

numstr,area,900
rectng,175,325,730,770
agen,9,900,900,1,200,0,0,,,0
agen,3,900,908,1,0,-200,0,,,0

numstr,area,1000
rectng,175,325,1130,1170
rectng,175,325,930,970
agen,3,1000,1001,1,200,0,0,,,0
agen,2,1000,1005,1,1200,0,0,,,0

numstr,area,1100              !create all vertical electrodes
rectng,330,370,1775,1925
agen,8,1100,1100,1,200,0,0,,,0
agen,4,1100,1107,1,0,-200,0,,,0
agen,2,1100,1131,1,0,-1000,0,,,0

numstr,area,1500
rectng,950,1150,1000,1100     !create reflector
rectng,890,910,930,1170
rectng,1190,1210,930,1170
rectng,910,1190,1140,1170
rectng,910,1190,930,960

numstr,area,1700
rectng,330,370,975,1125
agen,3,1700,1700,1,200,0,0,,,0
agen,2,1700,1702,1,1000,0,0,,,0

allsel,all
aovlap,all
allsel,all

asel,s,area,,1711
asel,a,area,,1710
cm,mem,area
allsel,all

cmsel,u,mem,area
cm,poly,area
allsel,all
```

```
!!!!!!!!!!!!!!! MESH MODEL !!!!!!!!!!!!!
!!!!!!!!!!!!!!!!!!!!!!!!!!!!!!!!!!!!!!!!!

cmsel,s,mem,area
esize,40
type,3
real,3
amesh,all
allsel,all

cmsel,s,poly,area
esize,40
type,1
real,1
amesh,all

!!!!!!!!APPLY STRUCTURAL BCS AND WRITE FILE !!!!!!!
!!!!!!!!!!!!!!!!!!!!!!!!!!!!!!!!!!!!!!!!!!!!!!!!!

lsel,s,loc,x,2100       !apply BCs on right side of structure
dl,all,,ux,0
dl,all,,uy,0
dl,all,,uz,0
dl,all,,roty,0
allsel,all

lsel,s,loc,y,2100       !apply BCs on top side of structure
dl,all,,ux,0
dl,all,,uy,0
dl,all,,uz,0
dl,all,,rotx,0
allsel,all

lsel,s,loc,x,0          !apply BCs on left side of structure
dl,all,,ux,0
dl,all,,uy,0
dl,all,,uz,0
dl,all,,roty,0
allsel,all

lsel,s,loc,y,0          !apply BCs on bottom side
dl,all,,ux,0
dl,all,,uy,0
dl,all,,uz,0
dl,all,,rotx,0
allsel,all

!!!!!!!!!!!!!!!!!! APPLY LOADS AND SOLVE !!!!!!!!!!!!!!!!!!
!!!!!!!! ENDING FOR UNIFORM PRESSURE ANALYSIS !!!!!!!!!!!!!

tref,20
allsel,all
BFE,all,TEMP,1,10       !make mem elements colder to induce tension
allsel,all
finish

/solu
```

```
antype,static

solve
finish

/solu
sstif,on
allsel,all
sfa,all,1,press,.00001
solve
finish

!!!!!!!!!!!!!! ENDING FOR MODAL ANALYSIS !!!!!!!!!!!!!!!!!!!!!!

!tref,20.5
!allsel,all
!BFE,all,TEMP,1,10      !make mem elements colder to induce tension
!allsel,all
!finish

!/solu
!antype,static
!pstres,on

!solve
!finish

!/solu
!ANTYPE,MODAL           ! Choose modal analysis type
!pstres,on
!MODOPT,LANB,15

!MXPAND,15
!solve
!finish
```

APPENDIX 3

EQUIVALENT CIRCUIT SIMULATION MATLAB CODE

```
%%%%% MATLAB CODE FOR SANDIA DEVICE CIRCUIT SIMULATION %%%%%%
%%%%%%%%%%%%%%%%%%%%%%%%%%%%%%%%%%%%%%%%%%%%%%%%%%%%%%%%%%%%

clear

%properties of air
rhoa=1.21; ca=343; vis=1.82e-5; zo=rhoa*ca;
%denisty, sound speed, viscosity,

%frequency range of calculation
nfreq=1000;
f=logspace(1,5,nfreq);
om=2*pi*f;

%area of membrane in m^2
A=2100e-6*2100e-6;

%membrane impedance
K=1/(A*43e-10); %Pa/m^3
fres=40e3;
M=K/(2*pi*fres)^2; %effective membrane mass/area;
C=6e7; %structural damping
Zmem=K./(i*om)+i*om*M+C; %P/Q

%gap impedance, P/Q
Kgap=(rhoa*ca^2/(2100e-6*2100e-6*2e-6)); %Pa/m^3
Rgap=2e7; %loss from squeeze film compression
Zgap=Kgap./(i*om)+Rgap;

%back-plate impedance
Kback=1/(A*.182e-10); %Pa/m^3
Rback=1e10; %loss from flow through back-plate
Zback_1=Kback./(i*om);Zback_2=Rback;
Zback=(Zback_1.*Zback_2)./(Zback_1+Zback_2);

%cavity impedance, P/Q;
Kcav=(rhoa*ca^2/(2e-3*6e-3*3e-3)); %Pa/m^3
Rcav=7e10; %loss from squeeze film compression
Zcav=Kcav./(i*om);

%vent impedance, P/Q;
lh=5e-3; TR=.1524e-3; %length and tube radius
R=8*vis/(TR^2); %P/v resistance per unit length
Zvent=R*lh/(pi*TR^2); %P/Q resistance

%%%%%% P1=pressure on membrane, P2=pressure at vent %%%%%%
%%%%%%%%%% Use superposition, P1=1, P2=0 %%%%%%%%%%%%%%%%
```

```
Zp1=Zcav.*Zvent./(Zcav+Zvent);
Zs1=Zback+Zp1;
Zp2=Zgap.*Zs1./(Zgap+Zs1);
Zs2=Zmem+Zp2;

Qmem_1=1./(Zs2); dmem_1=1e10*Qmem_1./(i*om*A);

semilogx(f,abs(dmem_1)); xlabel('Frequency (Hz)');
ylabel('Response (Å/Pa)'); pedit;
axis([200 60e3 0 150]);
```

REFERENCES

[1] J. Mason, "Companies compete to be heard on the increasingly noisy MEMS phone market," in *Small Times*, July 18, 2003.

[2] D. W. Schindel, D. A. Hutchins, L. Zou, and M. Sayer, "The design and characterization of micromachined air-coupled capacitance transducers," *IEEE Trans. Ultrason. Ferr. Freq. Cont*, vol. 42, pp. 42-51, 1995.

[3] M. I. Haller and B. T. Khuri-Yakub, "A surface micromachined electrostatic ultrasonic air transducer," *IEEE Trans. UFFC*, vol. 43, pp. 1-6, 1996.

[4] I. Ladabaum, X. C. Jin, H. T. Soh, A.Atalar, and B. T. Khuri-Yakub, "Surface micromachined capacitive ultrasonic transducers," *IEEE Trans. Ultrason. Ferr. Freq. Cont*, vol. 45, pp. 678-90, 1998.

[5] O. Oralkan, X. C. Jin, F. L. Degertekin, and B. T. Khuri-Yakub, "Simulation and experimental characterization of a 2-D cMUT array element," *IEEE Trans. UFFC*, vol. 46, 1999.

[6] M. Petersen, W. Olthuis, and P. Bergveld, "High-performance condenser microphone with fully integrated CMOS amplifier and DC-DC voltage converter," *IEEE J. MEMS*, vol. 7, 1998.

[7] P. R. Scheeper, A. G. H. v. d. Donk, W. Olthuis, and P. Bergveld, "A review of silicon microphones," *Sensors and Actuators A*, vol. 44, pp. 1-11, 1994.

[8] A. G. H. v. d. Donk, P. R. Scheeper, W. Olthuis, and P. Bergveld, "Modeling of silicon condensor microphones," *Sensors and Actuators A*, vol. 40, pp. 203-16, 1994.

[9] A. S. Ergun, S. T. Hansen, and B. T. Khuri-Yakub, "Improved modeling and design of microphones using radio frequency detection with capacitive micromachined ultrasonic transducers," presented at 2001 IEEE Ultrasonics Symposium, 2001.

[10] A. S. Ergun, B. Temelkuran, E. Ozbay, and A. Atalar, "A new detection method for capacitive micromachined ultrasonic transducers," *IEEE Trans. UFFC*, vol. 48, 2001.

[11] D. Certon, N. Felix, J. Guyonvarch, O. B. Matar, and F. Patat, "Characterization of transducer arrays by laser interferometry: influence of acousto-optic interactions on displacement measurements in water," *Proceedings of 2001 IEEE Ultrasonics Symposium*, pp. 1065-8, 2001.

[12] S. T. Hansen, A. Turo, F. L. Degertekin, and B. T. Khuri-Yakub, "Characterization of capacitive micromachined ultrasonic transducers in air using optical measurements," *Proceedings of 2000 IEEE Ultrasonics Symposium*, pp. 947-50, 2000.

[13] N. Bilaniuk, "Optical microphone transduction techniques," *Applied Acoustics*, vol. 50, pp. 35-63, 1997.

[14] B. M. Jost and J. P. Stec, "Refractive fiber optic microphones with ambient acoustic noise cancellation ability," *J. Acoust. Soc. Am*, vol. 98, 1995.

[15] D. S. Greywall, "Micromachined optical-interference microphone," *Sensors and Actuators A*, pp. 257-268, 1999.

[16] N. C. Loh, M. A. Schmidt, and S. R. Manalis, "Sub-10cm3 interferometric accelerometer with nano-g resolution," *J. Microelectromechanical Systems*, vol. 11, pp. 182-7, 2002.

[17] G. G. Yaralioglu, A. Atalar, S. R. Manalis, and C. F. Quate, "Analysis and design of an interdigital cantilever as a displacement sensor," *J. Appl. Phys*, vol. 83, pp. 7705-15, 1998.

[18] E. B. Cooper, E. R. Post, S. Griffith, J. Levitan, S. R. Manalis, M. A. Schmidt, and C. F. Quate, *Appl. Phys. Lett*, vol. 76, 2000.

[19] S. R. Manalis, S. C. Minne, A. Atalar, and C. F. Quate, *Appl. Phys. Lett*, vol. 69, 1996.

[20] T. Sulchek, R. J. Grow, G. G. Yaralioglu, S. C. Minne, S. R. Manalis, and A. Kiraz, "Parallel atomic force microscopy with optical interferometric detection," *Appl. Phys. Lett*, vol. 78, pp. 1787-9, 2001.

[21] O. Solgaard, F. S. A. Sandejas, and D. M. Bloom, "Deformable grating optical modulator," *Optics Letters*, vol. 17, pp. 688-90, 1992.

[22] Goodman, *Introduction to Fourier Optics*, 1988.

[23] H. Sagberg, A. Sudbo, O. Solgaard, K. A. H. Bakke, and I.-B. Johansen, "Optical microphone based on a modulated diffractive lens," *IEEE Photonics Technology Lett*, vol. 15, pp. 1431-3, 2003.

[24] E. Udd, *Fiber Optic Sensors: An Introduction for Engineers and Scientists*: Wiley and Sons, 1990.

[25] N. A. Hall, W. Lee, and F. L. Degertekin, "Capacitive micromachined ultrasonic transducers with diffraction-based integrated optical displacement detection," *IEEE Trans. on Ultrason. Ferr. Freq. Cont.*, 2003.

[26] S. A. Collins, "Lens-system diffraction integral written in terms of matrix optics," *J. Opt. Soc. Am*, vol. 60, pp. 1168-77, 1970.

[27] "VCSEL Model no. VCT-F85A332-S, Lasermate Corp., Walnut, CA, 91789."

[28] A. E. Siegman, *Lasers*: University Science Books, Mill Valley, CA, 1986.

[29] M. Okandan, P. Galambos, S. Mani, and J. Jakubczak, "Development of surface micromachining technologies for microfluidics and BioMEMS," *Proceedings of SPIE - The International Society for Optical Engineering*, vol. 4560, pp. 133-139, 2001.

[30] F. B. Hilderbrand, *Methods of Applied Mathematics*. New York: Dover Publications, 1965.

[31] S. D. Senturia, *Microsystem Design*: Kluwer Academic Publishers, 2001.

[32] P. Osterberg, H. Yie, X. Cai, J. White, and S. Senturia, "Self-consistent simulation and modeling of electrostatically deformed diaphragms," *Proceedings of the IEEE Micro Electro Mechanical Systems Cnference*, pp. 28-32, 1994.

[33] ANSYS, "Coupled Field Analysis Guide," vol. 7.1, 2004.

[34] ANSYS, "Element Reference Library," vol. 7.1, 2004.

[35] D. T. Blackstock, *Fundamentals of Physical Acoustics*: Wiley Inc., 2000.

[36] F. Chu and R. Holmes, "Efficient computation on nonlinear responses of a rotating assembly incorporating the squeeze-film damper," *Computer Methods in Applied Mechanics and Engineering*, vol. 164, pp. 363-373, 1998.

[37] F. Chu and R. Holmes, "Damping capacity of the squeeze film damper in suppressing vibration of a rotating assembly," *Tribology International*, vol. 33, pp. 81-97, 2000.

[38] A. H. Nayfeh and M. I. Younis, "A new approach to the modeling and simulation of flexible microstructures under the effect of squeeze-film damping," *Journal of Micromechanics and Microengineering*, vol. 14, pp. 170-181, 2004.

[39] L. Zhang, D. Cho, H. Shiraishi, and W. Trimmer, "Squeeze film damping in microelectromechanical systems," *American Society of Mechanical Engineers, Dynamic Systems and Control Division*, vol. 40, pp. 149-160, 1992.

[40] S. Calmes, C. Cheng, F. L. Degertekin, X. C. Jin, A. S. Ergun, and B. T. Khuri-Yakub, "Highly integrated 2-D capacitive micromachined ultrasonic transducers," *Proceedings of 1999 IEEE Ultrasonics Symposium*, pp. 1163-6, 1999.

[41] R. W. Fox and A. T. McDonald, *Introduction to Fluid Mechanics*: Wiley, 1992.

[42] T. B. Gabrielson, "Mechanical-thermal noise in micromachined acoustic and vibration sensors," *IEEE Transactions on Electron Devices*, vol. 40, pp. 903-908, 1993.

[43] T. B. Gabrielson, "Fundamental noise limits for miniature acoustic and vibration sensors," *Journal of Vibration and Acoustics*, vol. 117, pp. 405-410, 1995.

[44] M. Mullenborn, P. Rombach, U. Klein, K. Rasmussen, J. F. Kuhmann, M. Heschel, M. Amskov Gravad, J. Janting, J. Branebjerg, A. C. Hoogerwerf, and S. Bouwstra, *Sensors and Actuators A*, vol. 92, pp. 23-29, 2001.

[45] P. Rombach, M. Mullenborn, U. Klein, and K. Rasmussen, "The first low voltage, low noise differential silicon microphone, technology development and measurement results," *Sensors and Actuators A*, vol. 95, pp. 196-201, 2002.

[46] M. Pederson, W. Olthuis, and P. Bergveld, "A silicon condenser microphone with polymide diaphragm and backplate," *Sensors and Actuators A*, vol. 63, pp. 97-104, 1997.

[47] www.LarsonDavis.com, "Acoustic Test Products Group."

[48] T. Moulton, "Micromechanical devices with embedded electro-thermal-compliant actuation," *Sensors and Actuators A*, vol. 90, pp. 38-48, 2001.

[49] N. Hall and F. L. Degertekin, "An integrated optical detection method for capacitive micromachined ultrasonic transducers," *Proceedings of 2000 IEEE Ultrasonics Symposium*, pp. 951-4, 2000.

[50] X. C. Jin, O. Oralkan, F. L. Degertekin, and B. T. Khuri-Yakub, "Characterization of a 1-D capacitive micromachined ultrasonic immersion transducer array," *IEEE Trans. on UFFC*, vol. 48, pp. 750-61, 2001.

[51] J. D. Hamilton and M. O'Donnell, "High frequency ultrasound imaging with optical arrays," *IEEE Trans. UFFC*, vol. 45, pp. 216-35, 1998.

[52] H. Sontag and A. C. Tam, "Optical detection of nanosecond acoustic pulses," *IEEE Trans. UFFC*, vol. 33, pp. 485-99, 1986.

[53] J. D. Hamilton, T. Buma, M. Spisar, and M. O'Donnell, "High frequency optoacoustic arrays using etalon detection", IEEE Trans. Ultrason. Ferr. Freq. Cont," *IEEE Trans. Ultrason. Ferr. Freq. Cont*, vol. 47, pp. 160-9, 2000.

[54] F. L. Degertekin, N. Hall, and W. Lee, "Capacitive micromachined ultrasonic transducers with integrated optoelectronic readout," *Proceedings of 2001 IEEE Ultrasonics Symp*, pp. 875-881, 2001.

[55] S. T. Hansen, B. J. Mossawir, A. S. Ergun, F. L. Degertekin, and B. T. Khuri-Yakub, "Air-coupled nondestructive evaluation using micromachined ultrasonic transducers," *Proceedings of 1999 IEEE Ultrasonics Symposium*, pp. 1037-40, 1999.

[56] N. A. Hall and F. L. Degertekin, "Integrated optical interferometric detection method for micromachined capacitive acoustic transducers," *Appl. Phys. Lett*, vol. 80, pp. 3859-61, 2002.

[57] L. Medina and C. Wykes, "Multiple target 3D location airborne ultrasonic system," *Ultrasonics*, vol. 39, pp. 419-25, 2001.

[58] T. J. Robertson, D. A. Hutchins, D. R. Billson, J. H. Rakels, and D. W. Schindel, "Surface metrology using reflected ultrasonic signals in air," *Ultrasonics*, vol. 39, pp. 472-86, 2002.

[59] D. W. Schindel, A. G. Bashford, and D. A. Hutchins, "Chromatic aberration of an air-coupled ultrasonic Fresnel zone-plate," *Ultrasonics*, vol. 32, pp. 242-46, 1999.

[60] W. Lee, N. A. Hall, Z. Zhou, and F. L. Degertekin, "Fabrication and characterization of a micromachined acoustic sensor with integrated optical readout," *Special Topics in Quantum Electronics (STQE)(Invited Paper)*, vol. 10, pp. 643-651, 2004.

[61] W. Lee, N. A. Hall, and F. L. Degertekin, "A grating-assisted resonant-cavity-enhanced optical displacement detection method for micromachined sensors," *Appl. Phys. Lett*, vol. 85, pp. 3032-34, 2004.

[62] C. Zhou, S. V. Letcher, and A. Shukla, "A fiber optic microphone based on a combination of Fabry-Perot interferometry and intensity modulation," *J. Acoust. Soc. Am*, vol. 98, pp. 1042-6, 1995.

[63] J. Dziuban, A. Gorecka-Drzagza, K. Malecki, L. Nieradko, J. Mroz, and M. Szczygielska, "Silicon components for gas chromatograph," *Proc SPIE Int Soc Opt Eng*, vol. 4516, pp. 249-257, 2001.

[64] B. Kim, A. Razavi, F. L. Degertekin, and T. Kurfess, "Microinterferometer for non-contact inspection of MEMS," *Proceedings of International Workshop on Microfactories (IWMF)*, pp. 77-81, 2002.

[65] J. E. Graebner, "Optical scanning interferometer for dynamic imaging of high-frequency surface motion," *Ultrasonics Symposium*, vol. 1, pp. 733-736, 2000.

[66] P. C. Beard and N. T. Mills, "Miniature optical fibre ultrasonic hydrophone using a Fabry-Perot polymer film interferometer," *Electron. Lett*, vol. 33, pp. 801-3, 1997.

[67] M. Stanacevic, G. Cauwengberghs, and G. Zweig, "Gradient flow adaptive beamforming and signal separation in a miniature microphone array," *Proc. IEEE Int. Conf. Acoustics Speech and Signal Processing*, pp. 416-9, 2002.